Determination of Requirements for Smooth Operating Mode Transition and Development of a Fast Islanding Detection Technique for Microgrids

by

Lidula Nilakshi Widanagama Arachchige

A thesis submitted to the Faculty of Graduate Studies of

The University of Manitoba

in partial fulfilment of the requirements for the degree of

DOCTOR OF PHILOSOPHY

Department of Electrical and Computer Engineering

University of Manitoba

Winnipeg

Abstract

Opportunities for enhancing the security and reliability of power supply as well as the utilization of renewable and efficient energy sources have generated major interest in Microgrids. A microgrid typically consists of interconnected loads, distributed generators (DG) and energy storages, and should be able to operate in parallel with the utility grid or as a power-island. The main focus of this thesis is on the transition between parallel and islanded operation of a microgrid.

A literature review on existing microgrids was carried out. Based on the survey, a microgrid test system was implemented on PSCAD/EMTDC simulation program. The microgrid controls essential for the study and a load shedding scheme were designed and implemented.

When the microgrid changes from parallel to islanded operation, its controls need to be changed. It was found that delays in microgrid control mode transition can impact the amount of load need to be shed to preserve the frequency stability and the power quality of the islanded microgrid. The importance of fast detection of islanding was therefore highlighted.

The IEEE standard 1547.4-2011 recommends application of the existing DG synchronization criteria for microgrid synchronization. The adequacy of these criteria for synchronization of a microgrid with highly unbalanced loading was investigated. It was

found that the required criteria can be met with the support of switched capacitors for voltage balancing, and a circuit breaker supervised by a synchro-check relay is sufficient to successfully reconnect an islanded microgrid back to the utility.

In order to meet the requirement for fast detection of islanding of microgrids, new islanding detection technique was proposed. In the proposed scheme, Discrete Wavelet Transform was used to extract features from transient current and voltage signals, and then a Decision Tree classifier was employed to distinguish islanding events from other transients. Simulation based tests asserted that the proposed technique has a high reliability and fast response compared to most existing islanding detection methods. Also, the detection time of the proposed method was invariant with the power imbalance in the microgrid, and gave a zero non-detection-zone with any type of generator.

Acknowledgments

I would like to express my greatest gratitude to my academic adviser, Dr. Athula Rajapakse for the guidance, commitment and continuous support provided throughout for the successful completion of this research work. I am honoured to be his advisee. I am also thankful to the co-advisor, Dr. Dharshana Muthumuni and committee members for sharing their experience and their valuable comments and suggestions that helped very much to improve the quality of this thesis. I would specially like to thank Mr. Corey Senkow, the Distributed Resources Interconnection Engineer of Manitoba Hydro, Canada, for his support by providing resources and feedbacks throughout the research.

Also, the support received from the Natural Sciences and Engineering Research Council (NSERC) of Canada, Manitoba Hydro and University of Manitoba towards the research work is highly appreciated.

I would also like to thank all my friends at the Power Group of the Department of Electrical and Computer Engineering of the University of Manitoba for their continuous encouragement and for making my studies at the University of Manitoba one of the best experiences of my life.

Last but not least, my hearty thanks to my mother, sister and my loving friends for their love, great support and encouragement given in finalizing this important step in my life.

Dedication

To my beloved mother, late father and to my loving sister and friends.

Contents

List of Tables

List of Figures

List of Symbols

ω	Electrical angular velocity
ω_s	Synchronous electrical angular velocity
H	Per unit inertia constant
$P_{m,pu}$	Per unit mechanical power
$P_{e,pu}$	Per unit electrical power
w	Machine mechanical speed (rad/s)
w_h	Hub speed (rad/s)
w_v	Wind speed (m/s)
GR	Gear ratio
γ	Tip speed ratio ((mile/h)/(rad/s))
C_p	*P*ower coefficient
β	Blade pitch angle (degrees)
P	Output power (per unit)
A	Rotor blade sweep area (m^2)
ρ	Air density (kg/m^3)
G_{EFF}	Gear box efficiency
G_{MVA}	Machine rated MVA

$\Delta\tau$	Control mode transition delay
$\Delta\tau_{critical}$	Critical control mode transition delay
f_s	Frequency difference between the microgrid and utility grid
Δt_{insync}	Time duration that phase angle difference is within the threshold
$\Delta\Phi_{th}$	Phase difference threshold
Δf_{th}	Frequency difference threshold
ΔV_{th}	Voltage difference threshold
$E_{oscillation}$	Oscillation Energy
$I_{pk(transient)}$	Peak instantaneous current observed in any phase during the transition
P_{pk}	Peak grid power during the initial oscillations following the synchronization
t_{settle}	Oscillations settling time
W	*W*eight
b	Bias
ξ	Error
C	Penalty for the error term ξ
$\Psi_{m,n}$	Discretized mother wavelet
a_o, b_o	Fixed real values
m, n	Positive integers
$\hat{p}$	Proportion of observations in a random sample belonging to a class of interest
n	Size of the random sample
$z_{\alpha/2}$	Upper $\alpha/2$ percentage point of the standard normal distribution
Y_j	Class, where $j = 1, 2, ...J$
X_k	Predictor variable, where $k = 1, 2, ...P$

D^k_m	*m^{th} value of k^{th} variable*
L	Learning data set
t	Node number
$p(Y_j \mid t)$	Class probability distribution of the dependent variable at node t
$i(t)$	Impurity measure at node t
s	A particular split
p_L	The proportion of cases at node t that go into the left child node, t_L
p_R	The proportion of cases at node t that go into the right child node, t_R
$i(t_L)$	Impurity of the left child node
$i(t_R)$	Impurity of the right child node
$\Delta i(s,t)$	Goodness of split s at node t

List of Abbreviations

CART	Classification and Regression Trees
CB	Circuit Breakers
CHP	Combined Heat and Power
Db4	Daubechie's 4
DT	Decision Tree
DSP	Digital Signal Processor
DWT	Discrete Wavelet Transform
DER	Distributed Energy Resources
DG	Distributed Generator
EPS	Electric Power Systems
GSM	Global System for Mobile
IGBT	Insulated Gate Bipolar Transistors
IED	Intelligent Electronic Devices
LIBSVM	Library for Support Vector Machines
MV	Medium Voltage
MAS	Multi-Agent System
NDZ	Non-Detection-Zones
PLL	Phase-Locked-Loop

PMU	Phasor Measurement Units
PV	PhotoVoltaic
POI	Point-Of-Interconnection
PSCAD/EMTDC	Power Systems Computer Aided Design/ Electromagnetic Transients including Direct Current
PSS	Power System Stabilizer
PNN	Probabilistic Neural Network
ROCOF	Rate of change of frequency
SNR	Signal to Noise Ratio
SCR	Silicon Controlled Rectifiers
SPWM	Sine-wave Pulse Width Modulator
SCADA	Supervisory Control and Data Acquisition
SVM	Support Vector Machines
TDD	Total Demand Distortion
THD	Total Harmonic Distortion
VPN	Virtual Private Network
VSC	Voltage Source Converter
VVS	Voltage Vector Shift
VPD/FQB	Voltage-Power Droop/ Frequency-Reactive power Boost
WFT	Windowed Fourier Transform

List of Appendices

Chapter 1

Introduction

This thesis is focused in presenting appropriate solutions for the interconnection of microgrids to the utility grid. This chapter provides the background to the research, motivation behind the research, research objectives and the thesis overview.

1.1 Background

Centralized power generation became the mainstay with the recognition of the ability of transmitting electricity as alternating current at low costs across long distances. Electricity has been generated at central stations since 1881. With the economies of scale, centralized generation and radial transmission has worked out well up to the recent past [1]. Increasing power demand is always a challenging factor with the growth of population and economy. Although, enough generation can be added centrally, power transmission corridors are becoming narrower due to environmental constraints, right-of-way constraints and increasing infrastructure costs. Thus, existing transmission lines get more stressed when the utilities try to meet the increasing load demand through the central generation. There is also an increasing interest towards renewable and distributed energy

generation with the overwhelming concern on global warming. While there are technical developments in economical energy generation, power system deregulation has encouraged the generation owners to sell power in the electricity market. These with many other benefits offered by distributed generators (DGs), there is a rapid growth in the interconnection of DGs to power systems.

1.1.1 Distributed Generation and Power-islanding

The term distributed generation is referred to the small-scale generators connected to medium or low voltage power systems. They are not usually centrally planned or dispatched. DGs change the nature of the distribution system from passive to active, giving rise to certain technical issues [2]-[9]. One such issue is power-islanding, which is defined as "a condition in which a portion of the utility system that contains both loads and distributed energy resources (DER) remains energized while isolated from the remainder of the utility system" [10]. Fig. 1-1 is a simple representation of a distribution system with a DG. A power island is formed if breaker B1 opens while DG is still energized and connected to the distribution grid (B2 and B3 are closed).

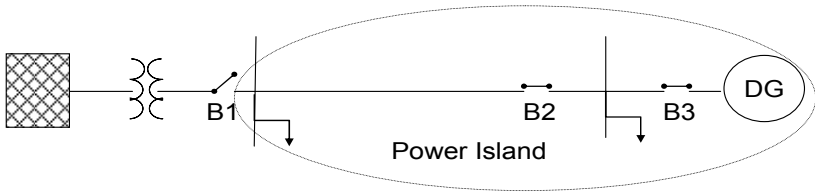

Fig. 1-1 An illustration of a power island.

Unintentional power-islanding results in several safety and power quality issues, including abnormal variations in frequency and voltage in the power-island, potential for

out of phase reclosing, possibility of creating ungrounded system depending on the transformer connections, and safety hazards for repair crews if the island is unidentified. Consequently, most interconnection regulations, which are usually guided by the IEEE standards 1547 [10], recommend to disconnect the DG within 2 s upon the formation of an island. This is achieved through anti-islanding protection, which is a subject that has been extensively studied [11]-[27]. However, frequent disconnection of DGs suppresses their expected benefits. A microgrid could be an attractive option to harness the benefits offered by DGs, eliminating the constraints on high penetration. Substantial environmental benefits may be gained through the utilization of energy efficient generation technologies and renewable energy resources [2]-[9], [28].

1.1.2 Microgrids

Microgrid is a portion of an electric power distribution system, located downstream of the distribution substation, encompassing variety of DGs, distributed storages and customer loads. With the embedded frequency and voltage control, microgrids can operate in parallel with the grid or as an autonomous power-island. Microgrids promote sustainability in power systems, focusing either or together on reliability and use of renewable energy resources and energy efficient generation technologies. Moreover, microgrids could reduce the network losses, defer the high investment costs required for network upgrades and also reduce the central generation reserve requirements. DGs provide local voltage support and microgrid as a whole increases the overall system reliability [2]-[3], [28]-[32].

In theory, a microgrid is designed as such that it appears to the utility grid as a single integrated system, functioning either as a load or a small generation source, potentially

alleviating many operational problems. However, the passive distribution system where only loads were present previously alters to an active network by introducing the DGs. This makes the operation of the distribution system more complex and gives rise to many protection, stability and safety issues [2]-[9]. Also, most of the renewable energy generation units are interconnected through power electronic interfaces. The inverter based micro-sources do not possess the "inertia" that conventional turbine driven generators have. Therefore, the microgrids require some form of fast responding energy storage to ensure initial power balance, when the utility grid supply is lost. Although, there is higher level of research done on microgrids [28]-[32], more research is required for finding possible simple solutions for safe and reliable operation of the system. Consolidated results would ultimately overcome the reluctance of utilities to allow intentional islanding.

1.2 Motivation

Due to its potential for promoting sustainable power generation and increasing power supply reliability, microgrids have been recognized as one of the key areas coming under the umbrella of smart grid technologies. Due to this increased attention, microgrids have become a subject that is being extensively researched around the world in the recent years [32]. The newly introduced IEEE standard 1547.4-2011 *Guide for Design, Operation, and Integration of Distributed Resource Island Systems with Electric Power Systems* [33], addresses the issue of intentional islands, which was missing in IEEE standard 1547-2003 [10] for *Interconnecting Distributed Resources with Electric Power Systems*.

Reference [32] by the author, presents an in-depth review of microgrid research around the world. There are numerous studies done on islanded and parallel operation of microgrids. Yet, research on transition of microgrid operation from grid connected mode to islanded mode is not well documented. Moreover, there are only a few studies documented in microgrid synchronization. Even the documented research on microgrid synchronization is mostly focused on converter based DGs [34]-[38].

The performance of the power-islanding detection methods in a microgrid setup is more demanding as the microgrid is designed to operate as a stable power island. Many power-islanding detection methods in practise and under research [11]-[27] would find difficult to meet the reliability (a measure of dependability: *operate correctly to the desired course*, and security: *not operate for other course*) and the response speed demanded by micorgrids without the use of expensive telecommunication facilities. Different islanding detection methods proposed in the literature can be mainly categorized into three groups: passive, active and telecommunication based methods. The passive methods make decisions based on the measured electrical quantities such as voltage and frequency [11]-[17]. In the active methods, disturbances are injected into the network and islands are detected based on the system responses to the injected disturbance [16]-[21]. The telecommunication-based methods use reliable communication links to transmit the circuit breaker status signals, which alert and trip the DGs when islands are formed [14], [18], [22].

The most common examples of these islanding detection methods are listed in Table 1-1. Passive islanding detection methods are preferred and widely used over the active and telecommunication based methods due to considerations such as the cost, sim-

plicity and power quality. In a situation where the intentional islanded operation is considered, there is a higher chance for the load and the generation of the island to be approximately balanced. Some passive islanding detection methods may fail to detect or take longer time to detect the islands when such power balance exists. On the other hand, anti-islanding protection cannot be made overly sensitive as that could lead to some unexpected control actions in a microgrid type of setup. Consequently, faster and more reliable power-islanding detection methods can bring benefits to the development of microgrids.

Table 1-1 Demerits of Existing Anti-islanding Relays

Anti-Islanding Method	Examples	Demerits
Passive [11]-[17]	Rate of change of frequency (ROCOF) Voltage Vector Shift (VVS) Over/Under Voltage Over/Under Frequency	• Fail /take comparatively longer time to detect the islanding if power in the island is nearly balanced • Nuisance tripping when made sensitive
Active [16]-[21]	Fault Level Monitor System Impedance Monitor Frequency Drift Method Reactive Error Export	• Degraded power quality • Unwanted interaction between the anti-island schemes of multiple paralleled DGs • Some cannot be applied with all types of generators
Telecomm. based [14], [18], [22]	Transfer Trip Scheme	• Costly compared to other two methods • Complex with multiple DER
	Power Line Carrier	• Costly compared to other two methods • Interfere with other signals (e.g. automatic metering)

On the grounds of aforementioned reasons, this thesis is focused on elaborating the problems associated with interconnecting microgrids to the utility, and proposes some novel solutions to overcome the problems.

1.3 Objectives

The overall objective of this research was to study the problems associated at the interconnection of microgrids to the utility, and propose effective solutions to overcome them. This goal was achieved by fulfilling a number of specific objectives.

The fist specific objective was to determine the state of the art of microgrids and identify the issues in the implementation of microgrids.

The second specific objective was to create a medium voltage (MV) microgrid test system. It was preferred to develop this microgrid test system based on an existing benchmark network, such as the one proposed by CIGRE working group C6.04.02 [39].

The next objective was to investigate the microgrid behavior during the transition from grid connected operation to islanded operation. Main emphasis was on the evaluation of the impact of the delays in microgrid control mode transition.

The fourth specific objective was to investigate the applicability of existing simple methodologies, such as synchro-check relays [40] and existing standards for microgrid synchronization. Under this objective, feasibility of using switched capacitor banks to meet the voltage criteria for synchronization and voltage balancing was also investigated.

The final objective was to propose solutions to any problems identified during the studies performed under third and fourth objectives. Having identified the importance of fast detection of islanding events to preserve the stability of microgrid, a fast islanding detection method was proposed. It was hypothesized that the transients generated during the islanding event contain unique signatures that reveal the cause of the corresponding transient event, and a classifier can be developed to distinguish islanding events from the

other disturbances. The objective was to prove this hypothesis and evaluate the performances of the proposed transient based islanding detection method in comparison to the existing islanding detection methods.

1.4 Thesis Overview

The thesis covers three main areas presenting the background, literature review on the existing methods and author's contributions. This chapter provides the introduction giving the background information with the problem statement and the research objectives. The rest of the report is organized as follows:

Chapter 2 presents the literature review, covering the areas of: (i) microgrids and its control, (ii) microgrid synchronization and (iii) power-islanding detection.

Chapter 3 presents the development of the microgrid test system in detail. The model validation and the evaluation of the conformity of the modeled microgrid to the IEEE standard 1547.4-2011 on "the *Guide for Design, Operation, and Integration of Distributed Resource Island Systems with Electric Power Systems*" [33], are also incorporated in this chapter.

The methodology and the outcome of the investigation on microgrid control mode transition from grid connected to islanded operation are comprehensively discussed in Chapter 4. It illustrates the effects of being fast or slow in the transition on frequency and voltage stability of the microgrid.

Chapter 5 presents a study on microgrid synchronization with the use of existing synchro-check relays and also presents the role of switched capacitor banks in a highly un-

balanced MV microgrid test system. It includes an analysis on the applicability of existing DG interconnection standards for microgrid synchronization.

The step by step approach of the design and implementation of the transient based islanding detection relay is presented in Chapter 6. The theory and methodology behind the selection of features is described. The classification accuracy and response time of the proposed islanding detection method is also discussed.

Chapter 7 presents the performance evaluation of the proposed islanding detection method giving a comparative analysis against the existing passive islanding detection methods under different scenarios.

Finally, the major conclusions, main contributions, and several suggestions for future research in the area of power-islanding detection and microgrids are highlighted in Chapter 8.

Chapter 2

Literature Review

As the penetration of DGs has been increasing, engineers have been preparing to face the design and operational challenges that necessarily follow any new trend. For the past few years, research on various aspects of DG-related issues and microgrids has been published. This chapter presents the summary of the reviewed literature related to microgrids and its control, microgrid synchronization and islanding detection.

2.1 Microgrids and Their Control

This section reviews the current status of the development of microgrids covering a brief description on components of a microgrid, and a summary on existing microgrid test systems that have been implemented and simulated. The study helps to visualize the present big picture of the microgrid and allows understanding the potential developments. Furthermore, the comparison of microgrids in several continents provides useful information for the design and choosing the right features for a particular microgrid application.

2.1.1 The Picture of a Microgrid

A microgrid is encompassed of a variety of DGs, distributed storages and a variety of customer loads, and it is a part of the distribution system. There can be different types of microgrid topologies, such as Local Electric Power Systems (EPS) Island (Facility Island), Circuit Lateral Island, Distribution Circuit Island, Substation Bus Island, Substation Island, and Adjacent Circuit Island. These are well defined in [33]. The substation islands refer to the MV microgrids, and their point-of-interconnection (POI) lies at the vicinity of the low voltage side of the substation transformer.

Distributed Generators

Generation technologies applicable for a microgrid can be categorized as renewable, efficient and conventional generation technologies. Renewable generation technologies include PV, small hydro and small wind turbines, while energy efficient small–scale generation technologies include combined heat and power (CHP) and micro-turbines. Some conventional generation technologies like IC engines can also be found in microgrid applications. These generation technologies are well known [2], [28], and thus, they are not discussed in detail. Nevertheless, it is important to note that CHP, PV and wind power generation are matured technologies and widely used in microgrids [32].

Almost all large integrated power systems in the world have been relying on centralized electricity generation such as large-scale hydro, coal, natural gas and nuclear power plants. Long-distance, high-voltage transmission carries the power to the customers from centralized sources. However, the growth of demand for clean electricity generation is changing this existing scenario, because the renewable energy resources are distributed

and have a less energy density. On the other hand, the aging centralized energy infrastructure, which can be more vulnerable with the increasing power demand, requires innovative and economical solutions as the construction of new transmission facilities is highly constrained by the environmental considerations. Many governments in the world have responded to these demands with suitable policy adjustments that encourage distributed and renewable energy generation. As a result, the share of renewable and efficient DGs is rapidly increasing. For example, [41] reports that in Canada, as of 2005, 25% of new electricity generation installed has come from distributed resources, compared to only 13% in 2002.

Energy Storage Devices

Energy storage is important for successful operation of a microgrid. The main functions of the energy storage devices in a microgrid are listed below:

1. Ensure the power balance in a microgrid, despite load fluctuations and transients, as most of the DGs with their lower inertia lack the capability of responding to these disturbances fast and maintaining the frequency and voltage stability.
2. Provides ride-through capability when there are dynamic variations in intermittent energy sources and allows the DGs to operate as dispatchable units.
3. Provides the initial energy requirement for a seamless transition between grid-connected to/from islanded operation of microgrids.

Among the available energy storage technologies, fly-wheels, batteries, and super-capacitors are more applicable for microgrid type of setup [42]-[44]. Fly wheels can be used as a central storage system for the whole microgrid. Batteries provide extra function

of being able to reserve energy for future demand. They can be used as either storage mounted on the dc bus of each micro-source or as a central storage system. Super capacitors would be an expensive choice compared to both flywheels and batteries [42]. Another option is to have a large traditional generation having considerable inertia (e.g.: hydro/steam/gas driven synchronous generator) along with the other micro-sources [32].

Interfacing Distributed Energy Resources

Distributed Energy Resources (DER) refers to both DG and energy storage technologies. Most of the emerging DER technologies require an inverter interface in order to convert the energy into grid-compatible ac power, and this type of interfacing may either consist of both converter and inverter or only an inverter.

Table 2-1 Typical Interfaces used with DER [45]-[46]

Primary energy source type		**Typical interface**	**Power flow control**
DG	CHP	Synchronous generator	AVR and Governor (+P, ±Q)
	Internal combustion engine	Synchronous or induction generator	
	Small hydro	Synchronous or induction generator	
	Fixed speed wind turbine	Induction generator	Stall or pitch control of turbine (+P, -Q)
	Variable speed wind turbine	Power electronic converter (ac-dc-ac)	Turbine speed and DC link voltage controls (+P, ±Q)
	Micro-turbine	Power electronic converter (ac-dc-ac)	
	Photovoltaic (PV)	Power electronic converter (dc-dc-ac)	Maximum Power Point Tracking and DC link voltage controls (+P, ±Q)
	Fuel cell	Power electronic converter (dc-dc-ac)	
Energy Storage	Battery	Power electronic converter (dc-dc-ac)	State of charge and output voltage/frequency control (±P, ±Q)
	Fly-wheel	Power electronic converter (ac-dc-ac)	Speed control (±P, ±Q)
	Super capacitor	Power electronic converter (dc-dc-ac)	State of charge (±P, ±Q)

The power electronic interface will be accommodated with filters and necessary protection systems. With the converter's capability of voltage and frequency control, these

DER units support the microgrid operation. The interfacing and power flow control options of common DER is summarized in Table 2-1.

Microgrid Loads

A microgrid could serve a variety of customers: residential, commercial and industrial. In general, commercial and industrial users are defined as critical/sensitive loads, and they demand high degree of power quality and reliability. The classification of loads based on the customer is important in achieving the expected microgrid control. With the classification of loads, part of the non-sensitive loads can be used as controllable loads to achieve the operating strategies in a microgrid as listed below [45]-[47].

1. To facilitate load/generation shedding within the microgrid to meet the net import/export power in grid connected mode.
2. To facilitate load/generation shedding to stabilize the voltage and frequency in the autonomous operation.
3. To improve the power quality and reliability of critical and sensitive loads.
4. To reduce the peak load to optimize the ratings of DER.

Interconnection of Microgrids

Microgrids get connected to the power system at the distribution level, and their energy handling capability is also limited with the use of renewable energy resources and waste heat. Thus, maximum capacity of a substation level microgrid is normally restricted to 10 MVA [28].

A microgrid is connected to the utility system via an interconnection switch. If the microgrid consists of voltage-sensitive loads such as semiconductor manufacturing, it re-

quires operation change-over times of less than 50 ms [28]. However, the existing protective equipment and circuit breakers are not capable to act that fast to isolate and change the mode of control in the microgrid. Therefore, in order not to disrupt the voltage sensitive loads, the voltage of the microgrid should be maintained above 50% of the nominal value during the changeover process [28].

Consequently, the recent research has proposed to apply static switches with fast response or Digital Signal Processor (DSP) controlled switching modules that consolidate both power switching and relaying, as the interconnection method [35],[48].

Microgrid Control

The main advantage expected from a microgrid is that it should allow itself to be treated as a controlled aggregated load or generator within the power system. Also, being part of smart grid systems, microgrids should facilitate adaptive control approaches.

The control approaches adopted in the existing and/or experimental microgrids are either embedded as autonomous parts of each DG, or use a central controller or use an agent based control [32]-[33]. These three types of microgrid controlling options as reported are summarized in the following discussion.

1. Autonomous control

Autonomous control in a peer-to-peer and plug-and-play operation model for each component of the microgrid with inverter based micro-sources is discussed in detail in [48]. In the peer-to-peer model, with one additional source, it ensures continuous operation of microgrid with loss of any component or generator. The plug-and-play model al-

lows a unit be placed at any point on the electrical system without re-engineering the controls. In [48], three possible autonomous control strategies are examined:

- Unit power control (every unit regulates its output power in the grid connected mode and switches to frequency control when islanded)
- Feeder flow control (each DG regulates the voltage magnitude at the connection point and the local feeder power flow vs. frequency droop characteristics ensures the power balance with the loads)
- Mixed control (allows some generators in unit power control and some in feeder flow control).

In [49], slightly different control scheme that allows the operation of multiple voltage source converters (VSCs) with standard inductor interfaces is presented. A control scheme named "Voltage-Power Droop/ Frequency-Reactive power Boost" (VPD/FQB) that operates in both grid-connected and islanded modes is proposed. It is independent of the islanding detection circuitry. Each current controlled VSC in such a microgrid has its own VPD/FQB controller that sets its current references to regulate the voltage and frequency of a common microgrid bus.

In [50], different combinations of governor control (droop control, fixed power control) in synchronous generators of a microgrid are discussed. It has concluded the necessity of having a communication system for proper coordination of generators.

2. Central control

A central microgrid controller is presented in [51], where each DG is equipped with two interface controls: one for grid connected and the other for islanded operation. Central controller unit decides the control mode of DGs based on islanding detection.

- In the grid connected mode, DG control is designed to supply only the active power and utility supplies the reactive power requirement.
- During islanded operation, the interface control is designed to maintain the voltage by supplying reactive power.

In [52], a centralized operation planning method, which is realized based on generation and load forecasting using neural network and fuzzy systems is proposed. It includes multi-objective evaluation of generation cost and CO_2 gas emission with some constraints. Unit commitment of generations includes start/ stop of power generations and storages. Load following function is accomplished based on PI control scheme. Use of power system stabilizer to compensate for the fluctuation of active power in microgrid is also proposed.

3. Agent based control

The agent based system facilitates both centralized co-ordination and local control as it operates in different levels in a hierarchy. This approach allows utilization of the strengths of both central and decentralized control systems and this is a possible candidate for future smart grid approaches.

An operation of a multi-agent system (MAS) for the control of a microgrid is presented in [53]. This system allows separating the complex centralized operation model into a hierarchical system. The particular MAS method consists of three different types of agents:

- Control agents (control directly the physical units of the system),
- Management agents (manage the microgrid and take decisions regarding the state),

- Ancillary agents (perform ancillary services, like communication tasks and data storage).

Another hierarchical method of integration of dc and ac DERs into the utility system is presented in [54]. In this framework, a large set of DER units are integrated into a three-level hierarchy through advanced power electronics and appropriate controls. A set of basic DER units are first integrated into a dc bus link through dc/dc or ac/dc converters. Then a collection of dc buses are integrated into an ac bus link through inverters. Finally, a range of ac buses are integrated into the microgrid. In the second level, droop control methods and the classic PI algorithm are used to control voltage, frequency and power output of the inverter.

Communication Strategies

Communication can be one of the most vital elements in a microgrid, particularly for power control and protection. The basic communication methods used so far include: radio communication, leased telephone lines, power-line carrier, internet and Global System for Mobile (GSM) Communications. The present microgrid experiments have used different communication protocols, but establishment of some standard communication protocol could help reduce the costs and accelerate the deployment of microgrids [32].

2.1.2 Experimental Microgrids and Microgrid Test-Beds

There is no particularly accepted benchmark test system for microgrids. The research on microgrids is based on either test-beds or simulations using different microgrid topologies.

Table 2-2 Summary of Microgrid Test Systems [32]

Detail			DGs								Energy Storage				Load			Microgrid Control		
Region	Microgrid	Radial (R)/ Mesh (M)	PV	Solar thermal	Wind	Fuel cell	CHP	Hydro	Diesel/Steam/Gas	Motor driven gen	Central (Cen)/ Individual (Ind)/ with Intermittent source(Int(source))	Battery	Fly wheel	Capacitor	Residential (R)/ Commercial(C)/ Industrial (I)	Static	Motor/Electronic	Central	Autonomous	Agent Based
Test-Beds and Intentional Islanding Experience																				
North America	Boston Bar, Ca	R	-	-	-	-	-	2	-	-	-	-	-	-	R	-	-		✓	
	Boralex, Ca	R	-	-	-	-	-	-	1	-	-	-	-	-	R	-	-		✓	
	CERTS, US	M	-	-	-	-	-	-	3	-	Ind	✓	-	-	-	✓	-		✓	
	UW, US	R	1	-	-	-	-	-	1	-	-	-	-	-	-	✓	-		✓	
Europe	Bronsbergen, Netherland	M	108	-	-	-	-	-	-	-	Cen	✓	-	-	R	-	-	✓		
	AmSteinweg, German	M	Several	-	-	-	1	-	-	-	Cen	✓	-	-	R	-	-			✓
	DeMoTec, German	M	1	-	1	-	-	-	1	-	Cen, Int(PV)	✓	-	-	R, C	-	-	✓		
	CESIRICERCA, Italy	R	8	1	1	-	2	-	1	-	Cen	✓	✓	-	-	✓	-			✓
	Kythnos, Greece	R	7	-	-	-	-	-	1	-	Cen	✓	-	-	R	-	-	✓		
	NTUA, Greece	R	2	-	1	-	-	-	-	-	Cen	✓	-	-	-	✓	-			✓
	Uni. of Manchester, UK	R	-	-	-	-	-	-	-	1	Cen	-	✓	-	-	✓	-	✓		
Asia	Aichi, Japan	R	3	-	-	7	-	-	-	-	Cen	✓	-	-	I, C	-	-	✓		
	Kyoto Eco-Energy, Japan	M	2	-	1	1	-	-	1	-	Cen	✓	-	-	R	-	-	✓		
	Hachinohe, Japan	R	5	-	4	-	-	-	3	-	Cen	✓	-	-	I, C	-	-	✓		
	CRIEPI, Japan	M	3	-	-	-	-	-	-	-	-	-	-	-	-	✓	-	✓		
	Sendai, Japan	R	1	-	-	1	-	-	2	-	Cen	✓	-	-	R,C,I	-	-	✓		
	HFUT, China	M	2	-	2	1	-	1	1	-	Int(PV), Int(wind)	✓	-	✓	-	✓	✓			✓
	Lab-scale, China	R	1	-	1	-	-	-	-	-	Cen	✓	-	-	-	✓	-	✓		
	IET, India	R	-	-	-	2	-	-	-	1	-	-	-	-	-	✓	-	✓		
Simulation Studies (Some Significantly Different Cases)																				
Benchmark low voltage microgrid		R	2	-	1	1	1	-	-	-	Cen or (Ind)	(✓)	✓	(✓)	R	-	-	✓	(✓)	
2 - DG microgrid		R	-	-	-	-	-	-	2	-	-	-	-	-	-	✓	-		✓	
Converter fed microgrid		R	Simulated as current sources								-	-	-	-	-	✓	✓		✓	
DC linked microgrid		R	1	-	-	1	-	-	-	-	Cen	✓	-	-	R	-	-		✓	

A comprehensive survey performed by the author on the existing microgrids is presented in [32], and a summary of this survey is reported in this section. Table 2-2 illustrates the use of DGs at each microgrid, and types of energy storage(s) used indicating whether it is a central storage, coupled with each DG or connected at intermittent DGs and load types used. It also indicates whether the system is radial or mesh. Control method is also indicated as if autonomous, central or agent based. Table 2-2 allows understanding the different ways of adopting microgrid technology in different regions as of today.

In most of the test cases, a central energy storage is used but there are some microgrids where there is no energy storage used. In the cases where there is no energy storage is used, generator inertia has been increased purposely and large capacity generators are used. Only CERTS microgrid in the US has used individual energy storage and few test systems are available where only intermittent sources are coupled with energy storages.

For maintaining the voltage and frequency at desired levels, North American microgrids have primarily used autonomous control, while the Asian countries have mostly used central control systems. A microgrid that uses agent based control is reported from China. Application of both central control and agent based control in microgrids is experimented in Europe. Agent based control systems apply different optimization techniques at the top level for operation planning. Locally, every control strategy (autonomous, central or agent based control) applied in practical microgrid test systems use the well known droop control method. It is observed that using both frequency-active power droop and voltage-reactive power droop insures the system stability.

It is noted that most of the experiments in microgrid test systems do not indicate the islanding detection method adopted. Some systems use tele-metering after islanding happens and some use transfer trip schemes. As previously mentioned, for most voltage sensitive loads, the critical changeover time is about 50 ms if the voltage drops below 50% during the changeover process [28]. It indicates the importance of having a fast islanding detection method.

Besides the voltage sensitive loads, islanding detection time could be a factor affecting the frequency and voltage stability of the islanded microgrid. Preserving the stability of the microgrid following the islanding is important for avoiding black starts in microgrids, which in turn increases the power system reliability.

Although there are several new controlling approaches proposed in the literature [48]-[49], [52], in actual implementation of microgrids, conventional droop control is always used. In the future it is expected that the system should allow separations of control tasks to different agents. This is an active research area [53]-[54], and most control system studies are carried out using simulations. This highlights the importance of having a good benchmark microgrid simulation model with commonly used control methods. Such a benchmark model allows comparison of new control strategies against the methods currently in practice. Also, having an accepted simulation model would help other activities such as the development of microgrid standards.

2.2 Resynchronization of Microgrids

When reconnecting a microgrid operating in the islanded mode to the utility grid, voltage, frequency and phase criteria must be satisfied. Synchronizing a microgrid consisting of several generators with different characteristics and loads is more challenging than synchronizing a single generating unit with the grid. In [33], three possible methods of microgrid synchronization has been identified: (i) active synchronization where there is a control mechanism to match the voltage, frequency, and phase angle of the island system to the utility grid, (ii) passive synchronization, which employs a synchronization check for paralleling meeting the requirements of IEEE standard 1547-2003 [10], and (iii) open-transition transfer where loads and DGs in the island are de-energized before reconnecting to the grid.

Among the numerous published research works on islanded and parallel operation of microgrids, there are only few studies, which specifically study the subject of microgrid resynchronization. The documented research on microgrid resynchronization are mostly focused on converter based DGs.

A prototype static switch with required control functions for microgrid resynchronization implemented on a Digital Signal Processor (DSP) is presented [34]. This static switch and its control are specifically designed for a converter based DG. Three types of static switches (circuit breakers (CB)-based, silicon controlled rectifiers (SCR)-based, and insulated gate bipolar transistors (IGBT)-based) are investigated and the test results for the CB-based switch are presented. However, the challenge to meet the cost reduction function is acknowledged in [34].

A similar static switch is proposed [35], for the convertor based DGs. The synchronization is achieved by satisfying a voltage difference threshold and ensuring that the current flow to be inbound from the utility towards the microgrid. A transient free reconnection is reported with static switch, even when the frequency and phase angles at the interconnection point are not matched.

An adaptive notch filtering technique for synchronizing converter based DGs to the system, is proposed in [36]. This method eliminates the use of phase-locked-loop (PLL). According to [36], the algorithm has a capability of frequency adaption and can tolerate unbalanced system conditions. Therefore, it is considered suitable for microgrid applications. However, the discussion is limited to the measurement technique.

Use of a back-to-back convertor as the interconnection switch is studied in [37]. Similar to other studies, the microgrid consists of converter based DGs only. In this arrangement, there are two circuit breakers beside the two back-to-back voltage source convertors (VSC). Both breakers are open and VSCs are blocked simultaneously at islanding. In resynchronizing, the circuit breaker in the grid side is closed first and the grid-side VSC is de-blocked. The microgrid side circuit breaker is closed and the microgrid-side VSC is de-blocked only when the capacitor voltage is stabilized to the reference. Control function is done using flip-flops. Since this method uses full rated back-to-back convertor, it would also be costly.

In contrast to the aforementioned literature, which can be grouped into active synchronization methods, the synchronization study reported in [38] is a passive synchronization approach. Further, it has considered convertor based DGs as well as synchronous generators. The study initially assumes a balanced loading condition, which is expected

to change only after a fault. It concludes that with the use of PLLs in convertor based DGs, resynchronization is not an issue if phase difference across the interconnection switch is small (less than 10^o) when there are only convertor based DGs in the microgrid. The paper further states that with the synchronous generator, having a small phase difference across the interconnection switch during reconnection could be problematic and concludes the requirement of having solutions for minimizing the phase angle difference and voltage balancing to facilitate smooth transition.

Literature survey indicates that research on microgrid synchronization is mostly focused on inverter based DGs and it lacks studies on the applicability of DG interconnection standards for microgrid synchronization as suggested in [33]. Studying the ability of using switched capacitor banks and commercially available synchro-check relays for microgrid synchronization would be beneficial for the practical implementation of microgrids.

2.3 Islanding Detection

The most common practice is to adopt the IEEE standard 1547 [10] in formulating guidelines and/or rules for interconnecting DGs in the distribution systems. These operational practice standards have been developed with an underlying assumption that the power system is radial and they try to maintain the assumption. In the past, the power available from DGs was not essential to support the load on the system. Hence, the standards suggest disconnecting the DGs for any “significant” fault (faults that could require the protection to be provoked) on the distribution system and thus, maintaining the radial nature

of the system. Consequently, the islanding detection relays are designed to avoid power islanding, and these relays are referred to as anti-islanding relays.

Table 2-3 Interconnection System Response to Abnormal Voltages [10]

Voltage range (% of base voltage[a])	Clearing time(s)[b]
V < 50	0.16
50 ≤ V < 88	2.00
110 ≤ V < 120	1.00
V ≥ 120	0.16

[a]Base voltages are the nominal voltages stated in ANSI C84.1-1995, Table 1.
[b]DER ≤ 30 kW, maximum clearing times; DER > 30kW, default clearing times.

Table 2-4 Interconnection System Response to Abnormal Frequencies [10]

DR size	Frequency range (Hz)	Clearing time (s)[a]
≤ 30kW	> 60.5	0.16
	< 59.3	0.16
> 30kW	> 60.5	0.16
	< {59.8-57.0} (adjustable set point)	0.16 to 300 (adjustable)
	< 57.0	0.16

[a]DER ≤ 30 kW, maximum clearing times; DER > 30kW, default clearing times.

IEEE standard 1547-2003 [10] recommends disconnection of DER when the voltage and/or frequency at the point of interconnection deviate from their base values due to faults and other disturbances. Tables 2-3 and 2-4 summarize the recommended responses to voltage and frequency deviations. IEEE standard 1547-2003 [10] also recommends that protection system should disconnect the DER within 2 seconds of the formation of the island.

Different islanding detection methods have been proposed in the literature. They can be mainly categorized into three groups: active methods, passive methods and telecommunication based methods. Other than these methods, there are some recent research car-

ried out, using novel technologies such as wavelets and/or classification techniques like neural networks and decision trees.

2.3.1 Passive Methods

Passive methods, which are relatively simple in construction, are widely practiced compared to the other anti-islanding methods. The loss of utility grid results in changes to the loading of the DG, which in-turn produces, changes in the voltage, currents and frequency at the DG terminal. Passive islanding detection methods make decisions based on these locally measured electrical quantities.

The most common passive islanding detection methods include, Over/Under voltage, Over/Under frequency, Voltage Vector Shift (VVS) and Rate of Change of Frequency (ROCOF). All frequency depended relays' (Over/Under frequency, VVS, ROCOF) responses depend on the system characteristics like, the real power exchange that is lost to the microgrid at the time of islanding (active power imbalance) and system inertia constant as they are built based on the swing equation given by (2.1). In derivation of (2.1) DGs with inertia has been considered. Over/Under voltage relay response mainly depends on the reactive power imbalance between the generation and load demand [11]-[17].

$$\frac{d\omega}{dt} = \frac{\omega_s}{2H}\left(P_{m,pu} - P_{e,pu}\right) \tag{2.1}$$

where, ω: electrical angular velocity, ω_s: synchronous electrical angular velocity, H: per unit inertia constant, $P_{m,pu}$: per unit mechanical power, and $P_{e,pu}$: per unit electrical power.

Passive islanding detection methods are reported to have comparatively large Non-Detection-Zones (NDZ) with higher relay settings, and when the relays are made sensitive, the security of these relays drop considerably [11]-[17].

Over/Under Voltage

The voltage levels change with the changes in reactive power imbalance between generation and demand. Thus, the voltage magnitude measured at the DER can be used to detect the island. In voltage relays, trip signals are generated if the measured voltage shows abnormal variation over a certain time period according to the utility standards, which are mostly based on Table 2-3.

Over/Under Frequency

In a power island, there can be an active power imbalance between the generation and demand causing a change in the generator speed according to the swing equation given by (2.1), which affects the frequency. A frequency relay monitors the frequency of the voltage at the DER. If the frequency rises above or drops below a predetermined limits for a certain time as given in Table 2-4, then the DER is disconnected from the grid.

Voltage Vector Shift (VVS)

The loss of grid connection results in a sudden change in the cycle length of the terminal voltage waveform. The cycle duration is either shorter or longer, depending on if there is an excess or a deficit of active power in the islanded system. VVS relays measure the cycle length starting from the each zero crossing of the terminal voltage. The current cycle duration (measured waveform) is compared with the last one (reference cycle). The variation in the cycle duration with respect to the reference cycle can be expressed as an

angle, and if this angle exceeds a predetermined threshold, a trip signal is immediately sent to the circuit breaker. Usually, VVS relays allow this angle threshold to be adjusted in the range from 2^o to 20^o [11]. The relay is disabled if the magnitude of the terminal voltage drops below a threshold value to avoid false operation. An analytical study explaining the theory on VVS relay can be found in [15].

Rate of Change of Frequency (ROCOF)

ROCOF relay uses the time derivative of the frequency to detect islanding, which is based on the swing equation given by (2.1). The rate of change of frequency is calculated considering a measuring window, usually between 2 and 50 cycles [11]. If the value of the rate of change of frequency is higher than a threshold value, a trip signal is immediately sent. Typical ROCOF settings installed in 60 Hz systems are between 0.10 and 1.20 Hz/s [11]. ROCOF relay is also disabled, if the magnitude of the terminal voltage drops below a threshold value to avoid false operation.

2.3.2 Active Methods

In the active detection methods, relays directly interact with the system. In most of the active methods, disturbances are injected into the network and islands are detected based on the system responses to the injected disturbance. Therefore, active methods are designed as such that these small perturbations will result in a significant change in system parameters when the DG is islanded, and the changes are negligible when the DG is in parallel operation with the grid [14], [16]-[21].

Active methods have high dependability and security levels but the detection times are concluded to be longer than passive methods [17], [21]. Also, some active methods cannot be applied with all types of generators [17]. Another possible demerit reported is the interference of disturbances introduced by having multiple DGs and possible mal-operation of the relays. It claims that there is no research documented for applying active methods with multiple DGs in operation [14]. Most of the methods inherit power quality issues with the injection of disturbances into the system for islanding detection.

Reactive error export, reactive power fluctuation, fault level monitoring, system impedance monitoring and frequency-drift are some of the active islanding detection methods that are reported.

Reactive Error Export

In reactive error export method, the relay has an interface to control the DG excitation current causing it to generate a known value of reactive power. It is not possible for the DG to deliver this specified amount of reactive power to the utility grid when an islanding situation occurs. Reactive power error between the setting and the actual reactive power being exported for a time-period greater than a preset value initiates the relay. For proper operation of the relay, the time setting is chosen to be greater than the duration of possible power fluctuations making it a slow responding relay. Typical operating time of the relay varies between 2 s to 5 s [17]-[19].

Reactive Power Fluctuation Method

In the reactive power fluctuation method, a small constant frequency signal is applied to the automatic voltage regulator of synchronous generator. Islanding is detected based

on the frequency deviation, which becomes significant upon islanding. Reactive power fluctuation method is designed for synchronous machines and can be applied for inverter interfaced DC sources type distributed resources. However, this method is not applicable to induction machine interfaced distributed resources [17].

Fault Level Monitoring

The fault level monitoring method uses a shunt inductor connected across the supply through a point-on-wave switched thyristor. The thyristor is triggered at a point close to the voltage zero crossing and the current through the shunt inductor is measured. It is possible to determine the system impedance and the fault level using the measured current pulse. This calculation is repeated at every half cycle to detect the formation of power islands, thus giving very fast response. It is reported that fault level monitoring is an accurate method but, its construction introduces a small voltage glitch at the zero crossover point [17]-[19].

System Impedance Monitoring

System impedance monitoring is a method that detects power-islanding by actively monitoring the system impedance. A high frequency source (generally a few volts at a frequency in the low kHz range) is used as the input to a voltage divider, and this is connected to the utility grid via a coupling capacitor at the DG interconnection point. This introduces a small high frequency ripple into the mains voltage, and the coupling capacitor is selected to have a negligible ripple on the mains when the DG is synchronised to the utility. After islanding, the impedance increases dramatically to the impedance of the DG and the divided high frequency signal is clearly detectable [19].

This method claims to be highly reliable and fast, but would fail if connected near power factor correction capacitors [19]. Also, injection of high frequency signals in to the system affects the system power quality and thus, this method is not particularly suitable for intentional islanding situations.

Frequency-drift Method

Frequency-drift islanding detection method is specifically used in inverter interfaced DGs. The output current of the converter is controlled to a frequency, which is slightly different to the nominal frequency of the system. Under normal conditions, the terminal frequency is dictated by the powerful bulk supply. If the mains supply is lost, frequency will drift until a certain shutdown level is exceeded. The active frequency-drift method reported to pose a large NDZ [20]-[21].

2.3.3 Telecommunication Based Methods

The telecommunication-based methods use a central controller at the utility level, which is equipped with the islanding detection algorithm. Telecommunication-based methods do not inject perturbations on the grid and the performance of these relays is independent of the type of DG and power imbalance (the grid power exchange that is lost to the microgrid at the time of islanding). Also, if properly designed, they have a zero NDZs. However, these methods are usually expensive to implement and islanding detection times depends on the type of communication used. Another drawback of these methods is complexity of implementation, which increases with the number of DGs. Transfer trip

scheme and power line signalling schemes are two types of telecommunication based methods [14], [18], [22].

Transfer Trip Scheme

The transfer trip schemes involve continuous monitoring of the status of all circuit breakers and reclosers that could island a DG in a distribution system. When a breaker disconnection is detected, the central algorithm determines which areas are islanded, and a signal is sent to the relevant DGs to disconnect from the grid. Supervisory Control and Data Acquisition (SCADA) systems can be used for this purpose [14], [18], [22].

Transfer trip schemes require high level of communication support. Traditionally, radio communication or leased telephone lines have been used. Recently, new communication media like internet broadband, wireless communication, optic fiber Ethernet and satellite communication have been introduced with different approaches (Phasor Measurement Units (PMU) based, intelligent electronic devices (IEDs) based, line differential protection based and with Virtual Private Network (VPN) using domestic broadband internet) to detect islanding. Thus, islanding detection relay operating times mainly depends on the communication media. With the various new communications approaches, the reported minimum relay operation time is 30 ms and the maximum is between 1.15 to 1.7 s [22].

Power Line Signalling Scheme

This scheme utilizes the power line as a signal carrier. There is a signal generator connected to the secondary side of the substation bus, which continuously broadcasts a signal to all distribution feeders. Each DG is equipped with a signal detector. If the detec-

tor does not sense the signal (caused due to the opening of any breakers between the substation and the DG), it is an islanding condition, and the DG can be tripped immediately [14], [22].

One of the drawbacks of this method is that, if the distance between substation and DG unit exceeds 15 km, there is a possibility of signal attenuation, which would plead for repeaters [22]. Also the cost of the signal generator is much higher and there is a possibility to create interference with other power line communication signals such as automatic metering [14]. According to [22], this method could have a small NDZ when using a subharmonic signal, and operating time of the relay is about 277 ms.

2.3.4 Wavelet Based Methods

Application of wavelet transform based techniques for islanding detection has been recently investigated [23]-[25].

In [23] and [24], the absolute value of certain wavelet coefficient (of voltage or frequency signal) is compared against a threshold value to detect the power islands. If the relevant wavelet coefficient remains above this pre-set threshold for a period longer than given time delay, an islanding is declared. These threshold values are system specific and determined through trials and/or based on the experience of utility engineers [24].

In [25], a hybrid islanding detection algorithm based on wavelet transform is used, and the method is specifically designed for single-phase photovoltaic (PV) DG systems. It employs the high frequency components of the current injected by PV inverters to reveal the islanding condition.

2.3.5 Intelligence Based Methods

There is some recently published research on islanding detection using pattern classification [26]-[27]. The decision tree classifier is used in [26] to classify the islanding situations. However, the classification is based on a complex, large set of features, which include total harmonic distortion, gradient of the product of voltage and power factor, etc. The method has given a misclassification rate of 16.67% in detecting islanding correctly, which gives only 83.33% islanding detection accuracy.

Reference [27] applies an artificial neural network to detect islands, and it has investigated two neural network architectures. Both architectures have used instantaneous three phase voltage measurements as training and testing data. The best achieved accuracy from one of the proposed architecture is 84.44%, and 98 – 99% accuracy is achieved with the other architecture. However, the paper does not reveal the size of the data set, and it does not mention whether faults are considered in the classification. Also, the investigation has been carried out for a simple test system having a single DG, single lumped load and 3 buses.

The literature review on islanding detection methodologies reveals that the existing relays are not particularly designed for intentional islanding. Among the available technologies, telecommunication based methods inherit the qualities to be applied with microgrids but, the complexity, cost and operating time dependence on the communication technology defer the positive points. Thus, finding a fast and reliable islanding detection approach targeting intentional islanding is a requirement and would be an asset for the future deployment of microgrids.

Chapter 3

Microgrid Test System Modeling

This chapter presents the modelling of the microgrid test system. The microgrid test system was derived from the proposed CIGRE MV benchmark test system [39], and the system control was designed based on the literature review on practical microgrids [32]. The developed microgrid test system complies with the guidelines given in IEEE standard 1547.4-2011 [33].

3.1 The Focus of the Design

The microgrid test system was modeled based on the observations and conclusions made from the literature survey. The following remarks were made basically referring to [32]:

1. Microgrids are controlled centrally, autonomously or using agent based systems. Despite the overall control method, all practical microgrids use simple droop control locally. Some simulation studies have proposed different control options, but they are not yet implemented in practical systems;
2. Most microgrids use central energy storages while few systems use energy storages with each intermittent source. There are some systems, which do not use an energy

storage but use a large capacity generator with higher inertia (e.g.: hydro/steam/gas driven synchronous generators);

3. There is very little information on methods of island detection used in microgrids. Some use tele-metering after islanding happens and some use transfer trip schemes;
4. A portion of the 'non-sensitive' loads is used as the controllable load by allowing it to be shed during islanding to stabilize the voltage and frequency.

Besides the aforementioned remarks of microgrids based on [32], the following important facts were extracted from the IEEE standard 1547.4-2011, the *Guide for Design, Operation, and Integration of Distributed Resource Island Systems with Electric Power Systems* [33], which were met in the development of the microgrid test system.

1. A microgrid can be of different system configurations such as, "*substation island," "substation bus island," "circuit island," "facility island,"* and etc. A *substation island* or a medium voltage microgrid is created when the substation transformer secondary side (lower-voltage side) breakers are open.
2. "While paralleled to the area Electric Power Supply (EPS), distributed resource (DR) equipment needs to meet the power-quality requirements of IEEE standard 1547-2003. When in DR island mode, the power quality needs to be acceptable to all parties."
3. "The DR island system needs to monitor and control generation output to ensure power is balanced in real time so that acceptable frequency and voltage are maintained. Load-shedding schemes may be implemented to ensure this."

4. "When a DR is operating isolated from an infinite source such as the grid, frequency control can be achieved by either speed droop or real power sharing. Speed droop (or a master-slave configuration) is defined as the reduction of the speed set point as the load on the generator is increased. In real power sharing, the system real load level is provided to all of the generators operating on the common isolated bus. Each generator controls its individual real power generated, to constantly adjust its output to match the system real load. One variation on the droop method of control is to have a single generator, typically referred to as the swing machine, operating in isochronous mode [56]. Other generators may be operated in droop against this swing machine and, by means of adjusting their speed set point, operated at a constant real power setting. The isochronous machine needs to be able to handle load rejection and acceptance to maintain the steady-state frequency."
5. "When a DR is operating isolated from an infinite source such as the grid, voltage regulation can be achieved by either voltage droop or reactive power sharing."
6. "The operation of the DR island system needs to be controlled by a strategy consistent with the planned operation of the island. There are at least three alternative control strategies, as follows: (i) Centralized control, (ii) Distributed control and (iii) Autonomous control." Distributed control refers to the agent based control that was discussed previously.

One of the main objectives of this thesis was to discover the problems associated with frequency and voltage stability of the microgrid, during and after the period of control mode transition (the simulation studies were done for duration of maximum 60 s since microgrid is islanded). Thus, the focus lied more on a medium voltage industrial

microgrid having critical loads than a low voltage residential microgrid. Accordingly, this thesis uses a microgrid model derived from a proposed CIGRE MV benchmark test system, which has been designed based on an actual power system with unbalanced loading [39].

3.2 Simulation Tools and the Test System

Simulation studies were carried out using PSCAD/EMTDC power system simulation software using a simulation time step of 25 μs [55]. CYMEDist distribution analysis software was used for power flow studies. These are well established commercial software used in utilities and power system consultation agencies for power system simulation.

The CIGRE MV benchmark test system [39], which was originally developed for DG interconnection studies, was augmented with the features necessary for microgrid operation based on an extensive review of microgrid research [32]. Fig. 3-1 presents the modeled microgrid test system. The loads were highly unbalanced with Phase-b having the greatest load. To emulate a generic microgrid [32], three different sources of DGs were integrated. As shown in Fig, 3-1, there was a 3 MW steam turbine driven synchronous generator connected to Bus-10, a 1 MW wind turbine driven fixed speed induction generator connected to Bus-7 with a 0.5 MVars of capacitive compensation, and a 0.35 MVA DC source connected to Bus-3 via a Voltage Source Converter (VSC) representing a photovoltaic system. These DGs were placed considering the recommendations made in [39], and specially the load flow of the system without DGs [Bus-10 was one of the weakest

buses and Bus-3 was one of the strongest buses]. A high capacity, higher inertia DG (the synchronous generator) was used to avoid the necessity of energy-storage.

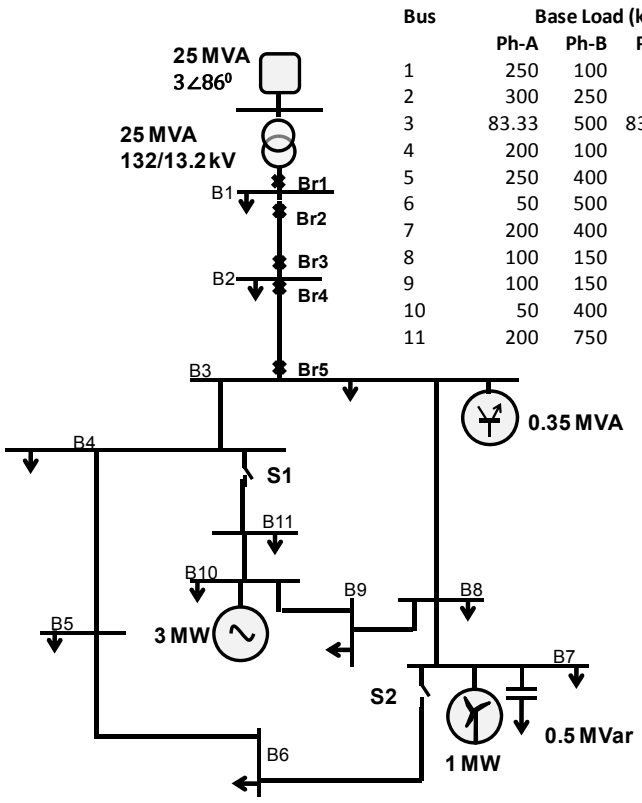

Bus	Base Load (kVA)			pf
	Ph-A	Ph-B	Ph-C	
1	250	100	300	0.9
2	300	250	200	0.95
3	83.33	500	83.33	0.9
4	200	100	100	0.9
5	250	400	50	0.95
6	50	500	100	0.95
7	200	400	100	0.95
8	100	150	200	0.9
9	100	150	100	0.95
10	50	400	50	0.9
11	200	750	100	0.95

Fig. 3-1 Microgrid test system.

The test system loads were simulated as constant RL loads and the base load values are shown in the figure. The load curves given in [39] show that peak load is 120% of the base load and the lowest level is 50% of the base load. The system has two switches S1, S2 (which were kept normally open) making it possible to change the network configuration from radial to ring operation. The test system consists only of over-head lines. Appendix A(i) presents the line data and Appendix A(ii) presents the tower data. Over-head

distribution lines were modeled as π-sections derived from the PSCAD frequency dependant transmission line model.

3.3 Microgrid Control Strategy

An agent based control mechanism as proposed in [53] was assumed in this study. The assumed agent based microgrid control strategy comprises of management, communication (or ancillary) and local (or control) agents, and it is shown in Fig. 3-2.

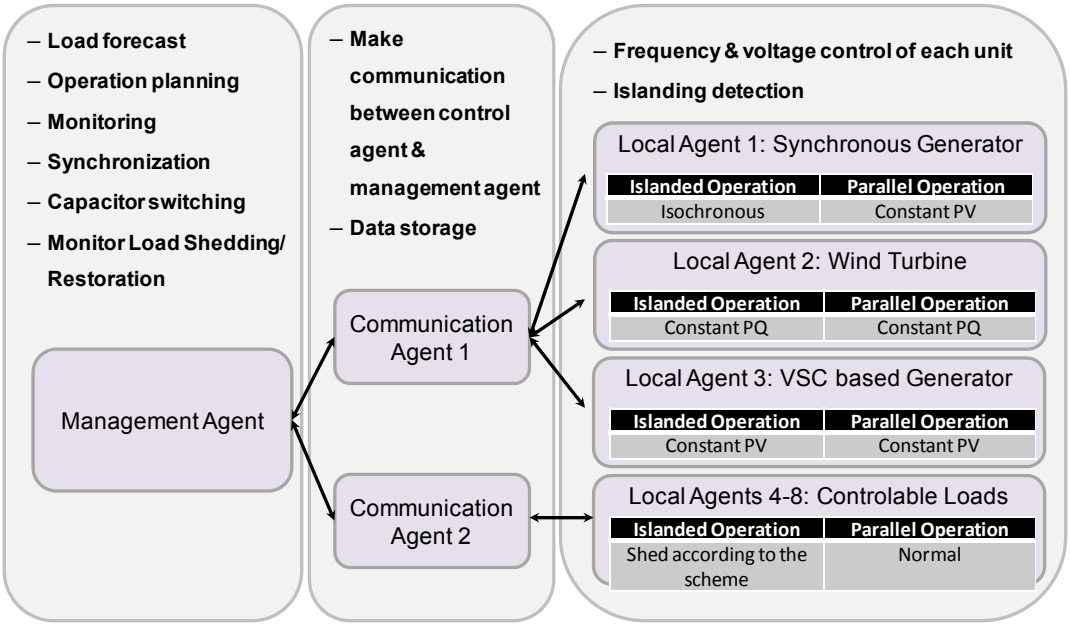

Fig. 3-2 Microgrid control strategy.

Islanding detection and voltage and frequency control are responsibilities of the local agent. The management agent is responsible for operation planning, load shedding monitoring and microgrid synchronization. The communication agent carries the status of each local agent to and from the management agent. The operating point of each DG (local agent) is assigned by the management agent as part of operational planning. In the island-

ed operation, the option of using a single machine (local agent) in isochronous mode with other local agents in constant power operation was integrated to the system [32]-[33]. Power control option of each local agent is discussed in the following subsections.

3.3.1 Synchronous Generator Control

The steam turbine driven synchronous generator emulates a co-generation plant. Standard synchronous generator and steam turbine models available in PSCAD were used, and typical values were used to define the required model [55]-[57]. The control block diagram of the plant is shown in Fig. 3-3 and the PSCAD model and some of the important parameters values used are given in Appendix A(iii).

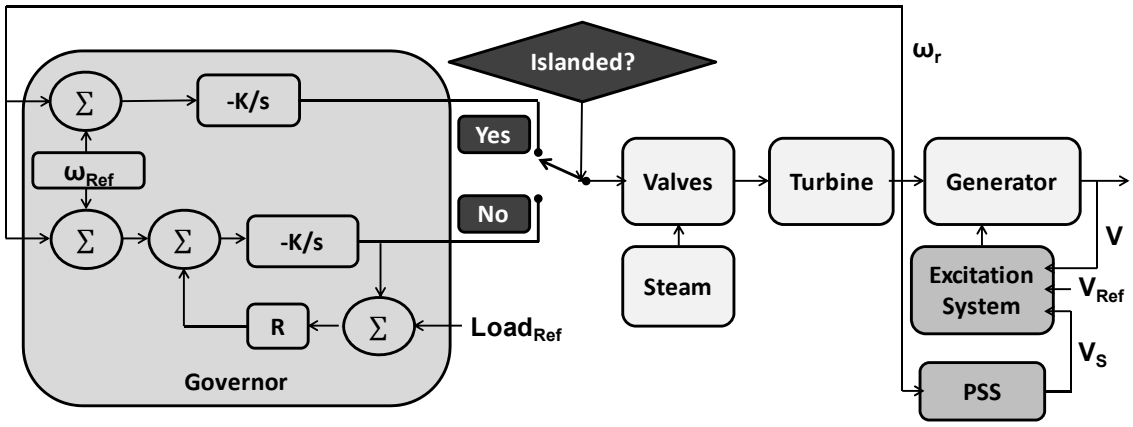

Fig. 3-3 Block diagram of the synchronous generator with frequency and voltage control.

The standard IEEE alternator supplied rectifier excitation system (AC1A) was used for voltage control and a power system stabilizer (PSS) was also incorporated to improve the system damping. The control block diagram of AC1A exciter with the PSS that was

modeled is shown in Appendix A(iv), and the typical parametric values [55] used are given in Appendix A(v).

An electro-hydraulic controlled governor excluding the over speed control was used for frequency control [55]. The block diagram of the electro-hydraulic controlled governor is shown in Appendix A(vi) and Appendix A(vii) presents the parametric values used in the grid connected and islanded modes. The speed reference was set to 1.00045pu, with the intention of facilitating resynchronization when the utility grid is restored. As shown in Fig. 3-3, the governor had two control modes corresponding to islanded operation and parallel operation. The control mode was selected based on the islanding detection relay output.

In the parallel operation of the microgrid, the synchronous generator was modeled to run as a constant PV generator, and it is in droop control mode with 5% droop and typical time constants [55]. The synchronous generator was selected as the swing machine in the islanded mode. Therefore, it was run as an isochronous generator, which responds for load changes and controls the frequency in the microgrid. In this mode of operation, the droop setting was made nearly equal to zero, effectively changing the governor to constant frequency operation. Therefore, the output power of the synchronous generator changes to follow the variations in the load demand while maintaining constant frequency. Fig. 3-4 illustrates the governor characteristics under grid connected and islanded operation.

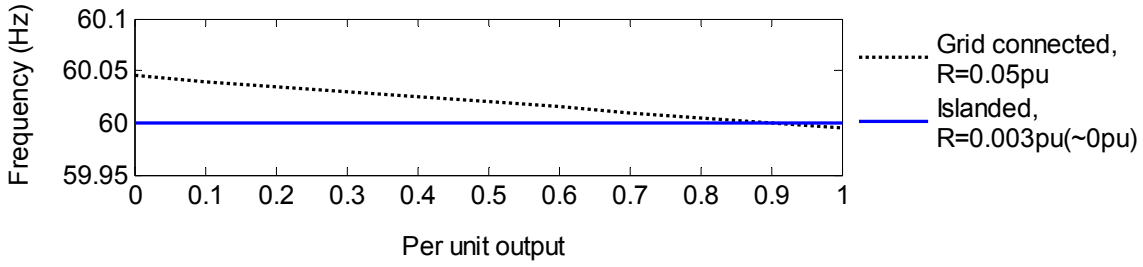

Fig. 3-4 Electro-hydraulic governor characteristics under grid connected and islanded operation.

3.3.2 Wind Turbine Control

The modeled wind turbine drove a fixed speed induction generator of 1 MW, and it was integrated with a pitch control mechanism to control the output power. A 0.5 MVar capacitor bank was connected at the generator terminal for reactive power compensation. Fig. 3-5 presents the control block diagram of the wind farm.

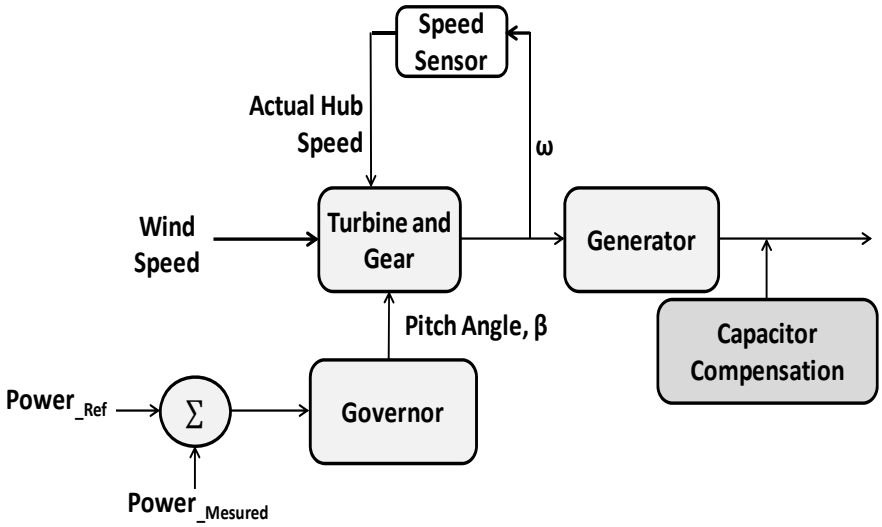

Fig. 3-5 Block diagram of the wind farm with frequency and voltage control.

The PSCAD model of the wind farm is shown in Appendix A(viii) [58], and Appendix A(ix) presents the block diagram of the wind turbine governor in pitch control and the parameters used (found by trials). The initial pitch angle (β) was found as suggested in

[59] by calculating the power coefficient to give 0.6 MW power output at a constant wind speed of 12 ms^{-1}. Equations (3.1) to (3.4) present the approximated non-linear functions that represent the blade dynamics [59].

$$w_h(w) = w/GR \tag{3.1}$$

$$\gamma(w) = \frac{2.237 w_v}{w_h(w)} \tag{3.2}$$

$$C_p(w,\beta) = \frac{1}{2}\left(\gamma(w) - 0.022\beta^2 - 5.6\right)e^{-0.17\gamma(w)} \tag{3.3}$$

$$P(w,\beta) = \frac{\frac{1}{2}\rho A w_v^3 C_p(w,\beta) G_{EFF}}{10e^6 G_{MVA}} \tag{3.4}$$

$$\text{rated mechanical speed} = \frac{\text{rated electrical speed}}{\text{pole pairs}} \tag{3.5}$$

where,

w – machine mechanical speed (rad/s),
w_h – hub speed (rad/s),
w_v – wind speed (m/s),
GR – gear ratio,
γ – tip speed ratio ((mi/h)/(rad/s)),
C_p – power coefficient,
β – blade pitch angle (degrees),
P – output power (pu),
A – rotor blade sweep area (m^2),
ρ – air density (kg/m^3),
G_{EFF} – gear box efficiency,
G_{MVA} – machine rated MVA.

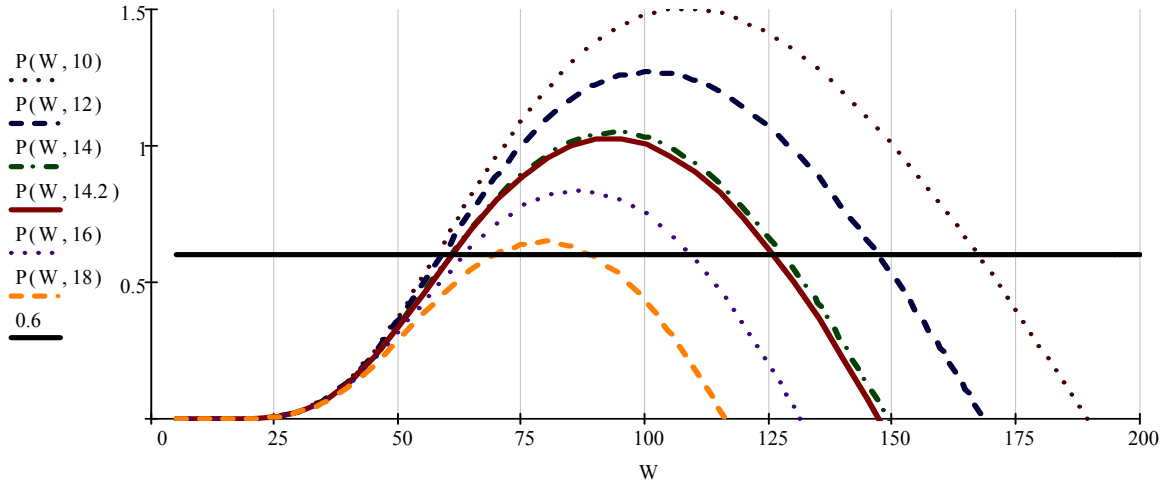

Fig. 3-6 Dependence of wind power output on pitch angle and mechanical speed of the wind turbine.

The turbine power output vs wind turbine mechanical speed relationship obtained from (3.3) and (3.4) is shown in Fig. 3-6. It illustrates the dependence of power output on the pitch angle for the modeled system at 12 ms^{-1} wind speed. The rated mechanical speed can be found by (3.5). Accordingly, for the rated electrical speed of 376.991 rad/s for 6-pole machine, the mechanical speed is 125.667 rad/s, and thus the initial pitch angle was found as 14.2^{o} from Fig. 3-6.

3.3.3 VSC with PI Control

Fig. 3-7 shows the block diagram of the VSC based DC source that represent the interface of a solar photo-voltaic system. The PSCAD model of the VSC based source is shown in Appendix A(x).

The system was equipped with typical VSC components [60] such as the DC capacitor, DC inductor (to minimize the DC voltage ripple), and an extra AC phase reactor (to reduce harmonics in AC currents). Considering the highly unbalanced nature of the microgrid, the VSC based system was connected to one of the strongest buses. Since simple decoupled control of VSC is not possible due to the unbalanced nature [61], direct control of VSC was used. The direct control involves adjusting the modulation index and the phase angle of the Sine-wave pulse width modulator (SPWM) directly according to the parameters being controlled [60]. A phase locked loop (PLL) was used in the SPWM for firing control.

The VSC was operated as a constant PV generator under both parallel and islanded operation of the microgrid. Therefore, power output was controlled by controlling the input DC voltage to a reference value. Simple PI controller was designed for this purpose,

and depending on the DC voltage error, phase angle of the SPWM was adjusted. Similarly, a PI controller was designed to control the terminal output voltage after the interconnecting transformer. The terminal voltage error was minimized by adjusting the modulation index of the SPWM. The initial parameters of the PI controllers were found by trials and later optimized using simplex method using the optimization tools available in PSCAD/EMTDC [62].

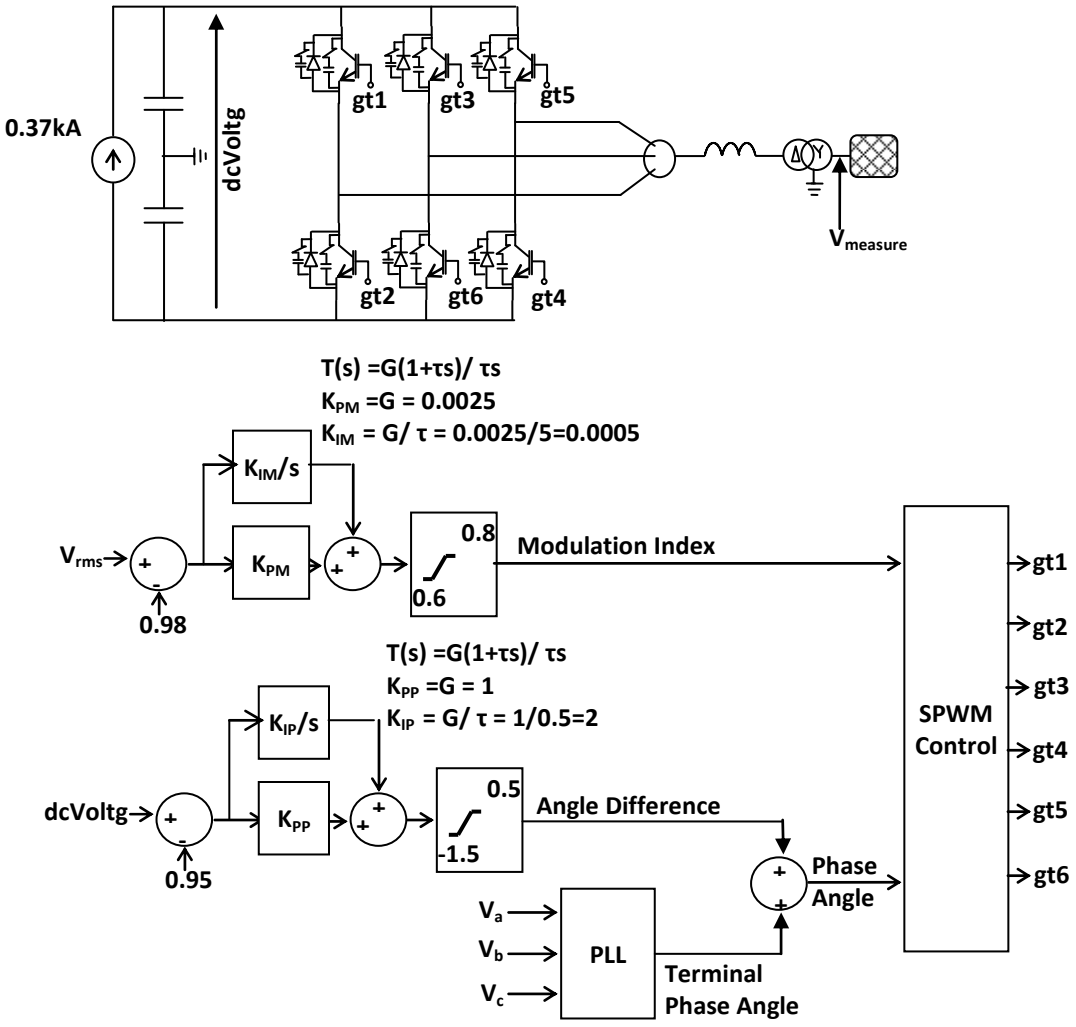

Fig. 3-7 The VSC based generator with frequency and voltage control.

3.3.4 Load Shedding

When the microgrid is islanded, a fast load shedding scheme is automatically activated to restore the balance between the load and available generation, and thereby prevent the frequency collapse [32]-[33]. The static and dynamic under-frequency load shedding are the two most widely applied concepts [62]-[64] for this purpose. Although, dynamic load shedding, which determines the amount of load to be shed at each stage by considering the magnitude of generation loss and available load on each feeder [64], is conceptually superior, static load shedding schemes are more common in practical power systems due to its simplicity [65]-[66]. Therefore, this thesis used a static load shedding scheme. The load shedding scheme was developed considering the generation mix in this particular microgrid test system, where a synchronous generator is used to control the microgrid frequency.

In the advanced static load shedding schemes, both frequency and rate of change of frequency is fed into the controller and when the frequency goes below a preset value and if the rate of change of frequency is more than a pre-set value, the controller initiates a signal to trip the loads assigned priority 1 (stage 1). If the frequency goes further down, the next stage of loads will be released and this will continue until the frequency stabilizes to its nominal value. Priorities are assigned to the loads in the design stage, considering their relative importance and the normal loading. However, in static load shedding, the real load behind the breaker or how much load has to be shed in order to reestablish the load balance is generally unknown [62]-[64].

Designing a static load shedding scheme involves four main steps [62]: (i) Calculation of total load to be shed, (ii) Deciding the number of load shedding stages and the size of load to shed at each stage, (iii) Setting the frequency and the rate of change of frequency thresholds, and (iv) Setting the time delays. The settings were found with the help of simulation studies. To avoid collapse of the system due to slow frequency drifts, time delayed back up relays, which operated regardless of the initial rate of change of frequency, were provided at each stage of the load shedding scheme. The load shedding scheme that was developed based on [66] is shown in Fig. 3-8.

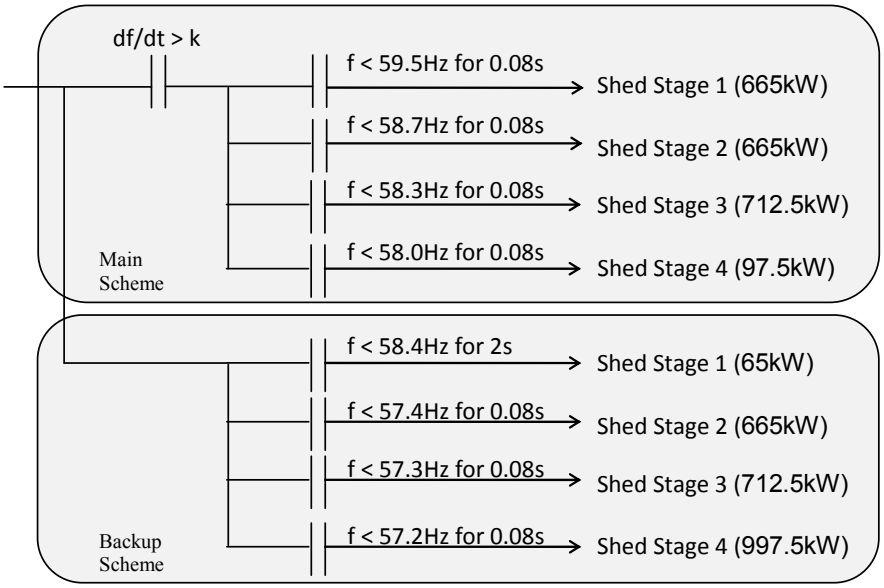

Fig. 3-8 Schematic representation of the designed load shedding scheme.

Table 3-1 Constant "*k*" of the Load Shedding Scheme

Inertia Constant of the Synchronous Generator, ***H*** (s)	Constant, ***k***
1	-1.71
2	-1.20
3	-0.98

Calculation of total load to be shed

If the frequency dependency of loads is neglected, the total overload can be calculated using (3.6).

$$\%\,\text{Overload} = \frac{\text{Load} - \text{Remaining Generation}}{\text{Remaining Generation}} \times 100 \tag{3.6}$$

It implies that 100% overload corresponds to a 50% loss of generation. Thus, at a 100% overload on the synchronous generator, 50% of the total load in the microgrid needs to be shed. The total load in the system is 6,390 kW (at 1pu voltage) resulting a requirement of shedding 3,195 kW of loads.

Decision of the number of load shedding stages and the size of load to shed at each stage

Generally four load shedding steps are recommended considering the economics aspects and complexity. The value of the load to be shed at various stages usually increases with every stage [64]. Having the loads being modeled as constant RL loads, the effective total load would be less than the theoretical value calculated at 1pu voltage. Thus, considering the available feeder loads, 10.5%, 10.5%, 11.5% and 15% of the total load were selected to shed in the four stages respectively.

Decision of the requirement of load shedding and frequency thresholds

The requirement of a load shedding was determined by the rate of change of frequency of the system, measured at the controllable loads. The critical rate of change of frequency setting was thus, determined by considering the system's ability to stabilize the frequency at an islanding happened in a balanced situation. Table 3-1 presents the rate of

change of frequency settings selected at different inertia constants of the synchronous generator.

The frequency at which the load shedding program starts was decided by considering the lowest frequency at which generators are allowed to run for long periods. According to the IEEE Standard 1547-2003 [10], generators connected to a distribution grid are required to tolerate ± 1% frequency variation in the steady state. Thus, 59.5 Hz was selected as the load shedding initiating frequency. The lowest setting should be above the critical frequencies of the generators, and the IEEE Standard 1547-2003 [10] recommends disconnecting distributed generators if the frequency drops below 57 Hz for a period longer than 0.16 s. This frequency threshold coincides with the under frequency setting of steam turbine generators, which is around 57 Hz [62]-[64]. Considering the aforementioned critical minimum frequency setting as well as the fact of unavailable spinning reserve in the microgrid, the minimum frequency of the load shedding scheme was selected as 58 Hz to avoid critical conditions. The intermediate frequency settings depend on the number of stages used in the system. In general, the setting frequency of the various stages is divided into equal frequency steps for nearly linear frequency decay. However, to avoid the shedding of more loads than necessary to stabilize the frequency in this particular microgrid test system, the frequency step between stage 1 (59.5Hz) and stage 2 (58.7Hz) were purposely kept higher.

Setting the time delays

It is advantageous to keep the time delay setting of the frequency relays as short as possible. This avoids an unnecessarily large decay of frequency, avoiding spurious trip-

ping of loads. Time delays of the relays were set at 5 cycles. Further, the breakers were simulated with an operating time delay of 5 cycles.

The backup system

To avoid system collapse, time delayed and frequency delayed back up relays were provided at each stage of the load shedding scheme, which operates regardless of the initial rate of change of frequency. Fig. 3-8 includes the backup relay settings, which were found by initial simulation studies. This load shedding scheme was developed with the intention to stabilize the system by shedding as small a load as possible.

3.4 Model Validation

The modeled microgrid test system was validated by modeling the same test system in CYMEDist distribution system analysis software. The system load flow results from CYMEDist was compared against the steady state values of three phase RMS voltages and phase angles from the PSCAD model. Furthermore, a transient simulation study was also conducted to illustrate the accurate operation of the developed microgrid control strategy. The PSCAD model was tested against the distribution system standards [10], [67] for the purpose of illustration of its accuracy in maintaining specifically, the power quality components under both grid-connected and islanded operation of the microgrid, which is also recommended in IEEE standard 1547.4-2011 [33].

3.4.1 Load Flow

Same system specifications as of those used in modeling PSCAD model were used in creating the simulation model in CYMEDist. In load flow comparison with PSCAD steady state results, the PSCAD synchronous generator model was first initialized using the CYMEDist output. Base case loading was considered in this study looking at the system operation without DGs and system with DGs in parallel operation and islanded operation. The base case total loading was 6390 kW and 2473.8 kVar.

The system without DGs

Fig. 3-9 presents the CYMEdist load-flow results compared against the PSCAD steady state bus voltages (RMS) and phase angles for the base case loads without connecting any DGs to the system. The switches S1 and S2 were kept open. A similar trend was observed with the peak loaded and low loaded cases. The highest error observed in comparing the phase voltages from the two models was only 0.5%, and the highest error observed with phase angles was only 0.01%.

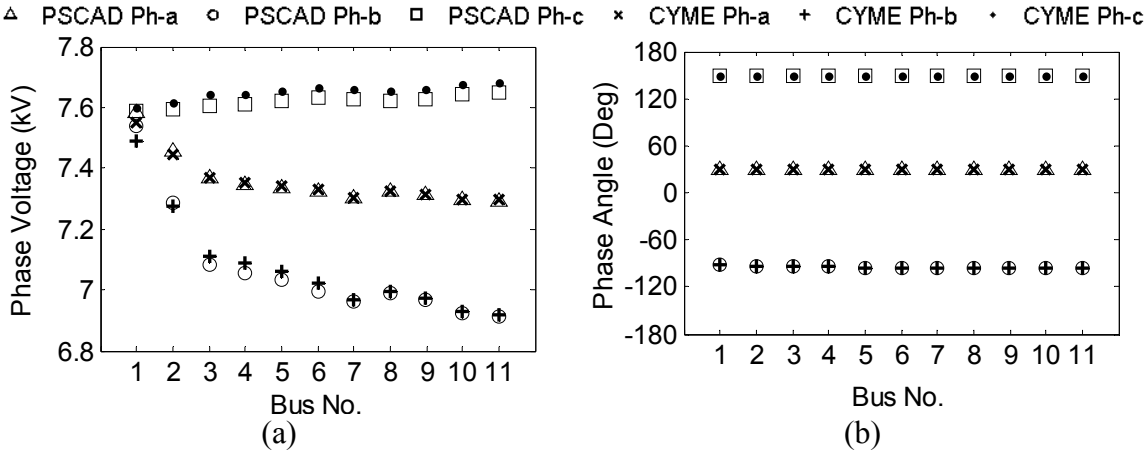

Fig. 3-9 Comparison of PSCAD and CYMEdist load-flow results without DGs (a) Phase voltages (b) Phase angles.

The system is radial when both switches S1 and S2 are open. However, Fig. 3-9 shows that Phase-c voltage is increasing along the length. This happens due to the unbalanced loading. For a balanced loaded condition phase voltages drop along the length. It can further observe that the Phase-b is the weakest of the three phases. The nominal phase voltage of the system is 7.62 kV. There is nearly -9% voltage deviation from the nominal in Phase-b of the Buses-10 and 11, and the voltage deviation of Bus-3 is -6.5% from the nominal.

The microgrid in parallel operation

Considering the observations in Fig. 3-9 and recommendations of [39], DGs were connected as shown in Fig. 3-1. Simulation studies were carried out with the assumption that the initial operating points of the generators were already set by the management agent. Therefore, it was considered that the power output of synchronous generator, VSC based source and the wind turbine were at 0.9 pu, 1 pu and 0.6 pu respectively.

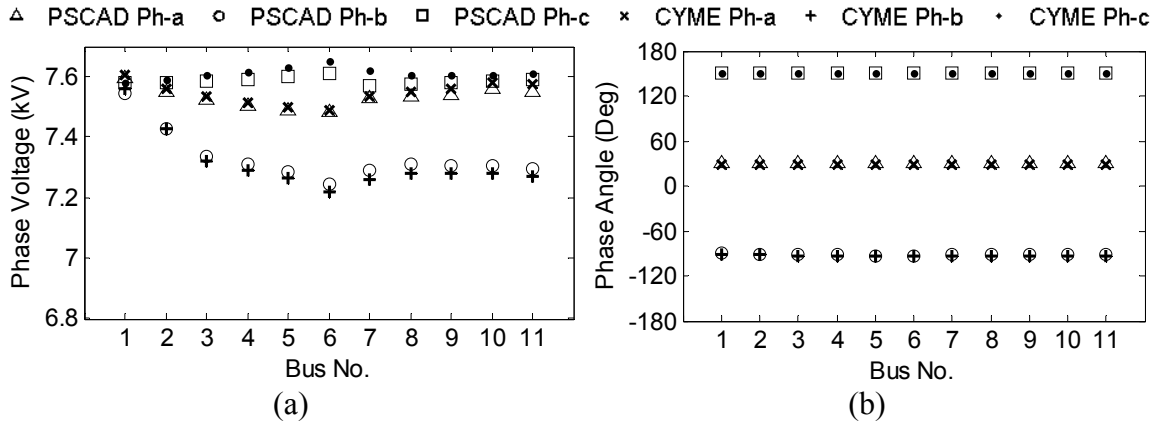

Fig. 3-10 Comparison of PSCAD and CYMEdist load-flow results with DGs connected for parallel operation of the microgrid (a) Phase voltages (b) Phase angles.

Fig. 3-10 presents the CYMEdist load-flow results compared against the PSCAD steady state bus voltages (RMS) and phase angles for the base loaded microgrid in parallel operation with the utility grid. The results validate the designed models again giving highly comparable results for both voltage and phase angles (the maximum voltage error < 0.6% and maximum phase angle error < than 0.01%).

One of the motivations to research on microgrids was that the microgrid is a means of harnessing the benefits of DGs. In comparing Figs. 3-9 and 3-10, it is very clear that DGs have improved the system power quality. Bus-10 and 11 were the weakest buses without DGs, and their Phase-b voltage, which had the lowest voltage level, has improved by 5% with the connection of DGs. Since Phase-b was highly loaded in this system, it still presented a low voltage level compared to the other two phases. With the connection of DGs, power system load flow results showed that Bus-6 had the lowest voltage levels with Phase-b having a voltage deviation of nearly -4.9% from the nominal.

The microgrid in islanded operation

The system was islanded by opening the breaker "*Br1*" shown in Fig. 3-1, after a predefined time. The system undergoes a transient state with load shedding before achieving the new stable operating point. This will be discussed under the frequency and voltage stability study. Also, the synchronous generator becomes the swing bus in the islanded operation and therefore, in order to meaningfully compare the PSCAD steady state results with CYMEdist load flow results, CYMEdist need to be initialize with measured phase angle and phase voltage at the swing bus from PSCAD. Consequently, only PSCAD re-

sults of RMS phase voltages are shown in Fig. 3-11 for the steady state islanded operation of the microgrid.

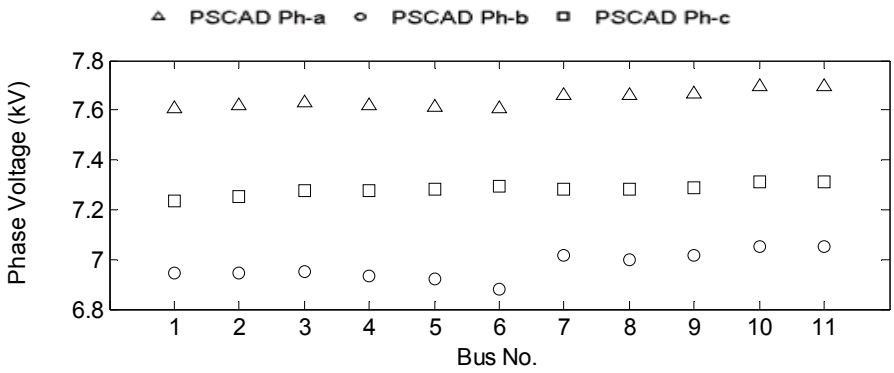

Fig. 3-11 PSCAD steady state operating phase RMS voltages for islanded operation.

Fig. 3-11 shows that, in the islanded operation, there is almost constant voltage distribution in all the buses. However, Phase-b voltage has dropped considerably and this voltage deviation in Bus-6 is 9.73% from the nominal, which is the worst case. Therefore, it is important to study the power quality of the microgrid in parallel and islanded operation to propose possible and necessary model improvements.

3.4.2 Frequency and Voltage Stability

In studying the transient behavior of the modeled microgrid test system, similar operating conditions as in the previous section were considered. The inertia constant of the wind farm and synchronous generator were 0.5 s and 3 s respectively.

The microgrid in parallel operation

To validate the accuracy of the model, a load tripping event was simulated. Initially, the microgrid was run at the base load condition in parallel with the grid. At t = 1 s a load

of (585 kW + 283 kVar) was tripped. In the grid connected operation, synchronous generator and the VSC based source operates as constant PV sources. The induction generator operates as a constant PQ generator.

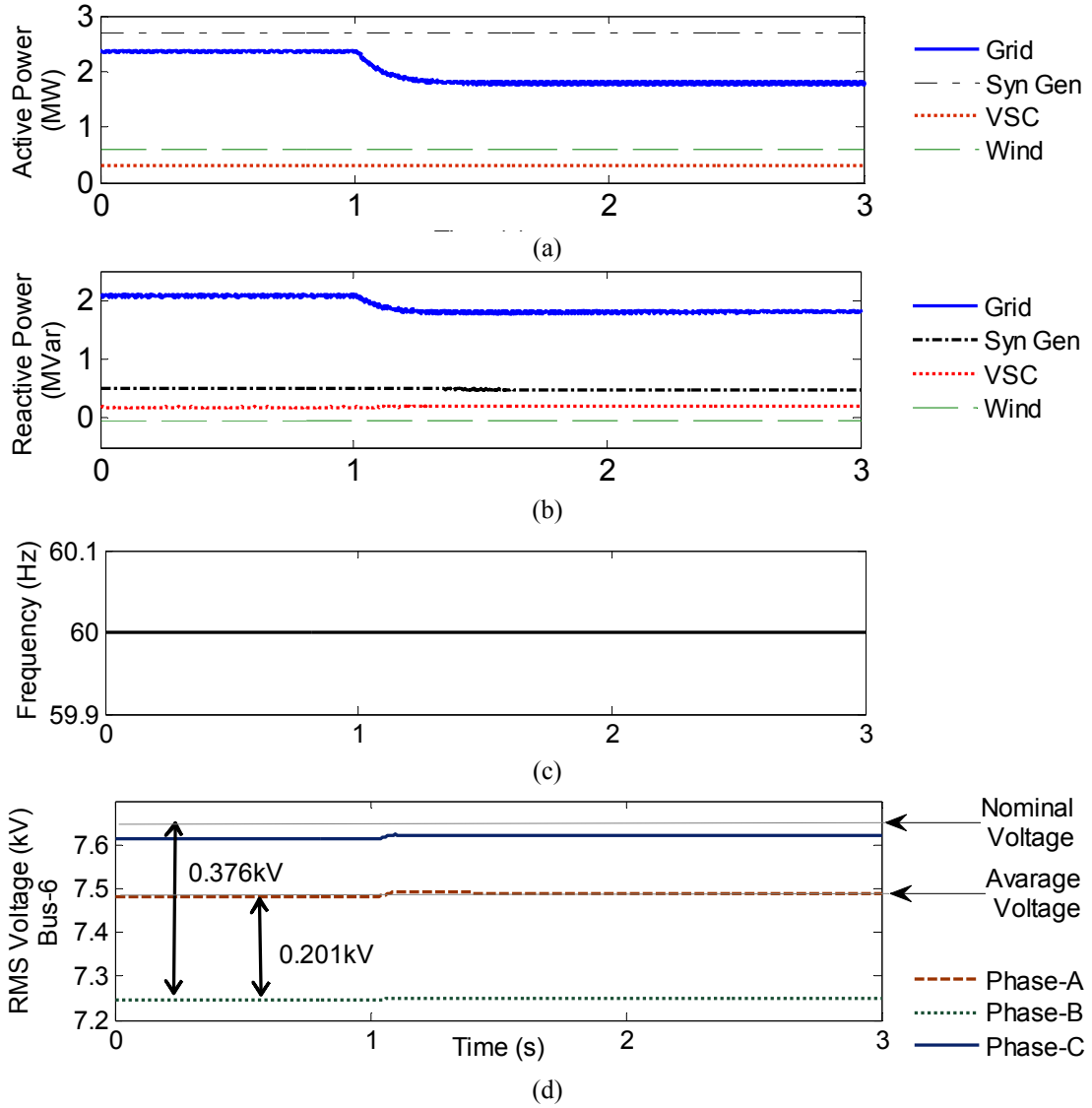

Fig. 3-12 System response to a load trip in parallel operation of the microgrid (a) active power variation, (b) reactive power variation of power sources. (c) time variation of frequency, (d) RMS phase voltages of Bus-6 (the weakest bus).

Figs. 3-12(a) and 3-12(b) present the real and reactive power variations during the event. The real and reactive powers imported from the grid drop in response to the load

change, but those of the DGs in the microgrid remain unchanged as expected. Fig. 3-12(c) presents the time variation of frequency, and Fig. 3-12(d) presents the RMS phase voltages of the weakest busbar (Bus-6) within the microgrid. Before the load was disconnected, voltage deviation of Bus-6, Phase-b voltage is nearly 0.37 kV giving a 4.9% from the nominal. This deviation with respect to the average of the three phase voltage is 0.2 kV.

The microgrid in islanded operation

The response of the microgrid, for an islanding event occurring at t = 2 s while the microgrid was operating at its base load is shown in Fig. 3-13. The variations of the power, frequency and voltage during the islanding event are shown. In the islanded operation, the synchronous generator was operated in the isochronous mode adjusting the frequency back to nominal value. The frequency reference was set to 1.00045pu, with the intension of facilitating resynchronization when the utility grid was restored. VSC based DC current source was still operated as constant PV generator, while the wind farm was run as a constant PQ generator. Since there was a power deficit in the islanded microgrid, the load shedding scheme had to be activated.

Fig. 3-13(a) and (b) present the active and reactive power responses of each generator for the islanding event corresponding to a +40% power imbalance (40% of the total power consumption in the microgrid was imported from the utility grid at the time of islanding). The synchronous generator stabilized the frequency after islanding, while the other two sources operating as constant power sources. The time variation of the frequency in the microgrid and utility grid for the islanding event are shown in Fig. 3-13(c).

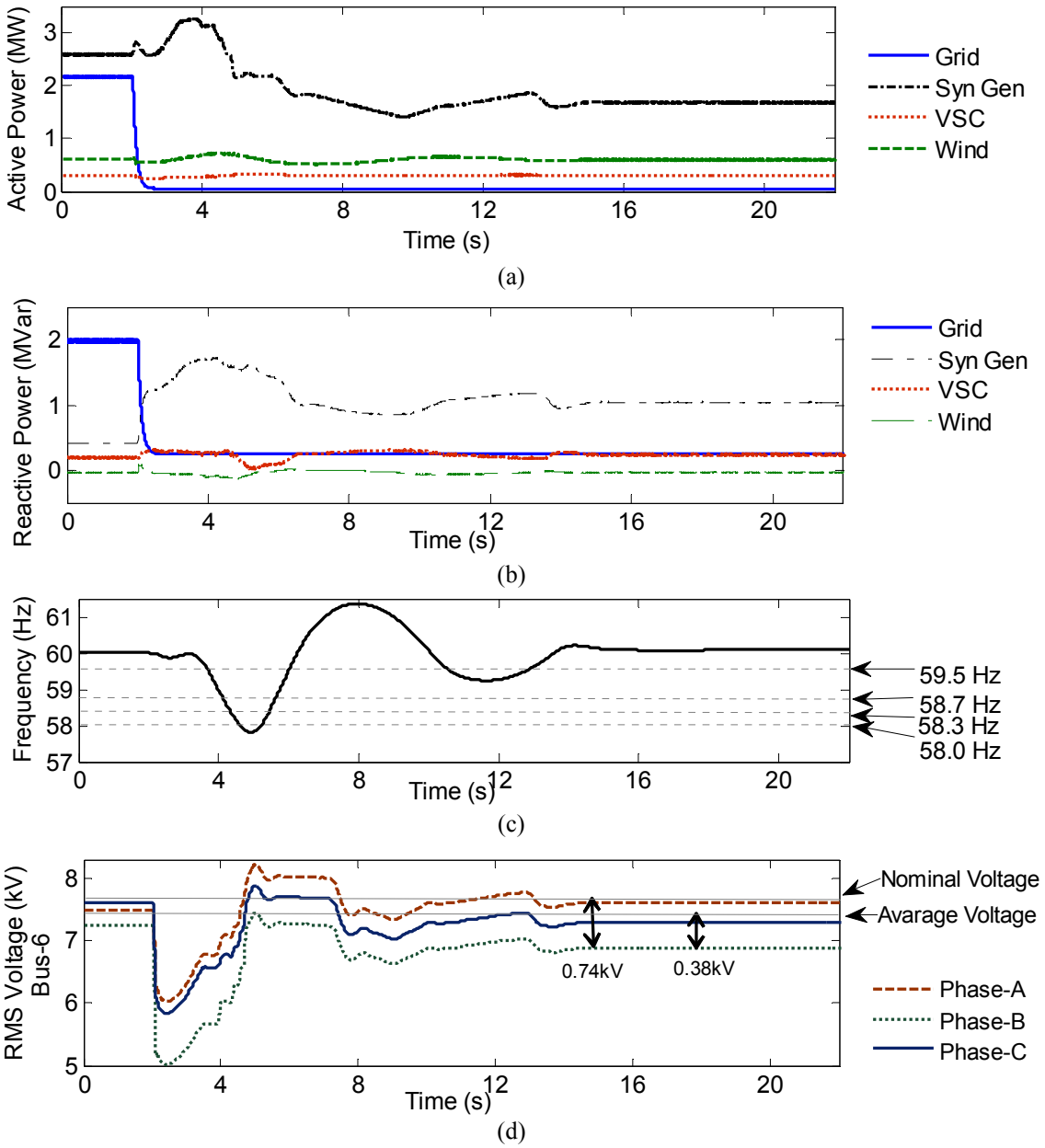

Fig. 3-13 Response to an islanding of the microgrid at t = 2s giving 40% power imbalance (a) source active power variation (b) source reactive power variation (c) frequency, (d) terminal rms voltage variation at the Bus-6.

The frequencies at which the loads were shed are marked by horizontal lines. Load shedding scheme underwent all four stages to stabilize the frequency. Islanded operation

satisfied the expected frequency standards having the deviation within 0.1 Hz. Fig. 3-13(d) presents the variation of terminal voltages of Bus-6, which was the weakest. Phase-b indicates the lowest voltage levels, and voltage deviation from the nominal was around 9.73% as previously discussed. This maximum voltage deviation with respect to the average of the three phase voltage was 0.38 kV.

The above observations confirmed the accurate performance of the microgrid in islanded and parallel operation, and in transition as designed. The next section looks into the power quality of the microgrid.

3.4.3 Power Quality

The microgrid should maintain the power quality requirements during both parallel and islanded operation. In complying with the IEEE standard 1547.4-2011 [33] for microgrids, the DG interconnection guidelines of the local utility, "*Technical requirements for connecting distributed resources to the Manitoba Hydro distribution system*" [67], and "*Power quality specification for interconnection to Manitoba Hydro's electrical system*" [68], were used in assessing the power quality conditions of the developed microgrid test system. Manitoba Hydro had used the IEEE standard 1547-2003 [10] as the basis for the development of its interconnection guidelines.

The Manitoba Hydro DG interconnection guidelines [67] specifies that synchronous generators must be equipped with excitation controllers capable of controlling the terminal voltage with a reference set between 95% and 105% of the nominal voltage. Induction generators are required to be provided with reactive power compensation to correct the power factor to ± 0.9 or better. Similarly, inverters and static power converters are re-

quired to be capable of adjusting its power factor to ± 0.90 or better. These requirements are met in developing the DG controlling strategy discussed in the Section 3.3.

Steady state voltage and frequency

According to [66], the steady state voltage operating range for distribution systems above 1 kV is ± 6%, and the normal system frequency operating range is 60 ± 0.2 Hz. For voltage levels less than 25 kV, voltage unbalance, as defined in (3.7), is expected to be below 4% in urban the areas under normal operating conditions [67]-[68].

$$\%\ \text{Voltage unbalance} = \frac{\Delta V_{max}}{V_{avg}} \times 100 \tag{3.7}$$

Where, V_{avg} is the average of the three phase voltages and ΔV_{max} is the maximum deviation from the average phase voltage.

Table 3-2 Steady state operating conditions at parallel and islanded operation of the modeled Microgrid

Description	Parallel Operation	Islanded Operation
Frequency deviation from the nominal (60 Hz)	0.0006Hz ≈ 0Hz	0.08Hz
Maximum voltage deviation (Observed at Bus-10, Phase-b)	4.9%	9.7%
% Voltage unbalance	2.7%	5.2%

The steady state frequency deviation from nominal, 60 Hz, voltage deviation from nominal, phase RMS 7.621 kV and the voltage unbalance at parallel and islanded operation of the microgrid are summarized in Table 3-2. These results were extracted from the cases in frequency and voltage stability study under the Section 3.2.2. It shows that both steady state frequency and voltage standards were well satisfied for the parallel operation of the microgrid. However, only frequency standards were met in islanded operation of the microgrid. The steady state voltage deviation and voltage unbalance were higher than

the maximum allowable limits given in the distribution system standards [67]-[68]. Therefore, appropriate means must be developed to meet the voltage standards in islanded operation of the microgrid. The proposed solution is discussed in Chapter 5.

Harmonics

The developed microgrid test system is equipped with a VSC based DC source, which introduces harmonics into the system. Although the thesis is not focused on a power quality study, this section provides an understanding of the level of harmonics present in this system. The recommended maximum limit for both, total demand distortion (TDD) and total harmonic distortion (THD) for a system less than 66 kV at the POI is five. This limit is defined for a TDD and THD calculated for harmonics up to the 50^{th} order [68].

Table 3-3 TDD and THD at the POI for parallel operation of the modeled Microgrid

Load	Total Demand Distortion (TDD)			Total Harmonic Distortion (THD)		
	Phase A	Phase B	Phase C	Phase A	Phase B	Phase C
Base	1.295	0.619	1.62101	0.037	0.031	0.042
Low	4.165	2.297	1.887563	0.044	0.042	0.047
Peak	0.758	0.315	0.843276	0.035	0.031	0.040

Table 3-4 TDD and THD at the POI for islanded operation of the modeled Microgrid

Load	Total Demand Distortion (TDD)			Total Harmonic Distortion (THD)		
	Phase A	Phase B	Phase C	Phase A	Phase B	Phase C
Base	1.435451	1.251186	1.410599	0.921408	0.861021	0.920548
Low	1.49849	1.263354	1.494262	0.962676	0.856355	0.990423
Peak	1.511197	1.286099	1.470155	0.986469	0.842179	0.97205

Tables 3-3 and 3-4 present the maximum TDD and THD levels observed at the POI of the microgrid for parallel and islanded operation respectively. Results are shown for three loading conditions of the microgrid. The base load was 6390 kW and 2474 kVar

while low load referred to 50% of the base load and peak load referred to 120% of the base load. The synchronous generator, wind farm and VSC based sources were operated at 0.9pu, 0.6pu and 1pu. This study particularly intends to present the level of harmonics in the system, therefore the particular specifications given in [68] for the calculation of TDD and THD was not followed. Instead, TDD and THD were calculated considering harmonics up to 63rd order, which were found using the available harmonic analysis components in PSCAD/EMTDC simulation software.

According to Table 3-4, in the islanded operation of the microgrid, there is apparently an even level of TDD and THD at all the loading conditions considered. With the values being considerably lower than the given standards for TDD and THD [68], the individual current and voltage harmonics levels can be predicted to be within the reasonable range.

Similarly, Table 3-3 shows that the THD was considerably low at all the loading condition considered for the parallel operation of the microgrid. This indicates that there was a low level of voltage harmonics in the system. However, with the high values obtained for TDD, the microgrid had considerably high level of current harmonics in the system in parallel operation at low loaded condition. Fig. 3-14 present the individual current harmonics as a percentage of the fundamental for phase-A current, observed at the POI of the microgrid in parallel operation at low loaded condition. It shows that there was more than 2% of 2nd and 3rd harmonics present in the current, which was introduced because of the unbalance loading and the IGBT switching in the VSC based DC source.

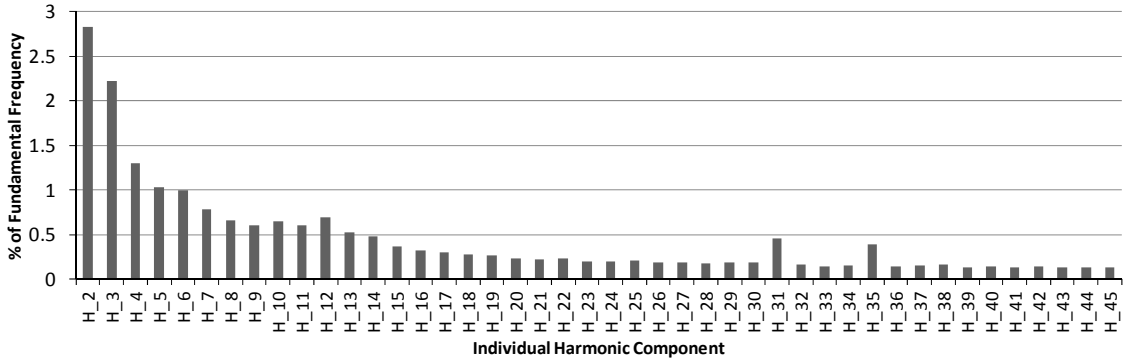

Fig. 3-14 Individual harmonic components of Phase-A current as a % of the fundamental, at the POI of microgrid at a low loaded condition in parallel operation.

Therefore, there is a provision for improvements by developing a special control algorithm for VSC based source connecting to the unbalanced microgrid. Further, specific power quality studies could help to standardize this microgrid test system. Despite the above possible improvements, this microgrid test system, which was derived from the CEGRE MV Benchmark test system and modeled based on a profound literature survey of existing microgrids, could be effectively used in studies on transient simulation of microgrids.

Chapter 4

Microgrid Control Mode Transition

This chapter presents the outcome of an investigation on microgrid control mode transition from grid connected to islanded operation. It reveals the importance of fast transition and introduces a notion of critical control mode transition delay for a microgrid.

4.1 Background

There are numerous studies done on voltage, frequency, and transient stability of microgrids during islanded and parallel operation of microgrids [32]. However, there is a lack of details on how the microgrid control mode transition from parallel to islanded operation is achieved, and its effect on the subsequent stability of the islanded microgrid. This control mode change-over time depends on the response time of the islanding detection technology used. In addition to changing of frequency and voltage control modes of generators, an islanded microgrid often requires under-frequency/under-voltage load shedding schemes to automatically drop loads to prevent the complete collapse of the microgrid.

Furthermore, with respect to the parallel to islanded mode transition, IEEE standard 1547.4-2011 [33] states that "at the time of the microgrid separating from an area EPS and forming the island, transient and dynamic voltage effects can arise due to the redistribution of energy stored in the large inertia machines if exist in the island". In addition to the microgrid stability, power quality during the transition can also be an issue in specific situations. The voltage-sensitive loads such as semiconductor manufacturing, requires operation change-over times of less than 50 ms or otherwise the voltage should be maintained above 50% of the rating at any time of operation [28]. Thus, the capability of existing islanding detection technologies to detect the islanding event and change the mode of control of the microgrid in a timely manner needs to be examined. The islanding detection time depends on the technique used and the grid power import/export that was lost at the time of islanding (power imbalance in the island), or on the communication delays, if transfer trip arrangement is used.

This study particularly looked into the microgrid behavior in the transition period and examined the effects of being fast or slow in the transition on the microgrid stability. In order to properly investigate the above, it was important to simulate a detailed model of a realistic microgrid. Therefore, the developed microgrid test system with generic frequency and voltage controls, and a load shedding scheme discussed in Chapter 3 was used in this study. Although several sophisticated microgrid control systems designed to specific microgrid systems can be found in literature [32], the most generic frequency and voltage controls and the conventional static load shedding scheme were used in this study with the intention of obtaining more general conclusions. As discussed in Chapter 3, the

controllers were developed in such a way that test system meets the control and power quality requirements specified in IEEE standard 1547.4-2011 [33].

The effects of the control mode transition delay on the microgrid were studied through simulations for a wide range of power imbalances in the microgrid. Sensitivity of the frequency and voltage responses to factors such as the inertia of the microgrid was also analyzed.

4.2 Microgrid Behavior at Islanding

The system frequency, rate of change of frequency and the terminal voltages are the basic quantities that characterize the system behavior upon a disturbance. This section illustrates the microgrid behavior for islanding events at different grid feeding levels. The synchronous generator control mode was instantly (without a delay) changed from droop controlled to isochronous mode at the event of islanding. The operation of the load-shedding scheme was blocked in this part of the study.

Simulation studies were carried out with the assumption that the initial operating points (power output) of the generators were already set by the master agent. Therefore, it was considered that the operating points of 3 MW synchronous generator, 0.35 MVA VSC based source and the 1 MW wind farm were at 0.9 pu, 1 pu and 0.6 pu respectively at the time islanding happens. The inertia constant of the wind farm was kept constant at 0.5 s and the synchronous generator inertia was changed (1 s, 2 s and 3 s) to study the responses under varying inertia constants (0.8 s, 1.5 s and 2.2 s) of the microgrid. The percentage real power imbalance defined by (4.1) is the grid real power exchange that was

lost as a percentage of the total real power consumption in the microgrid at the time of islanding. The "+" sign indicates the microgrid was importing real power from the grid at the time of islanding and the "-" sign indicates microgrid was exporting power to the grid at the time of islanding. The reactive power imbalance is also defined in a similar manner. Different power imbalances in the microgrid were simulated by changing the system loading level as a percentage of the base load.

$$P_{imbalance} = \frac{\pm P_{Grid}}{P_{Grid} + P_{SynGen} + P_{VSC} + P_{Wind}} \times 100 \quad (4.1)$$

Note: ***Power imbalance*** *should not be confused with unbalance between phases (voltage/ current/load). The word "unbalance" is used when specifying differences between phases.*

4.2.1 Time variation of frequency

One of the basic passive islanding detection techniques is the under frequency detection at the DG terminal. According to [14] and [70], islanding is declared if frequency goes below 59 - 59.5 Hz depending on the standards followed. The generators are tripped if frequency goes below 57 Hz for more than 0.16 s [10], [62].

Figs. 4-1 (a) and (b) presents the time variation of frequencies when islanding happens at t =1s for power imbalances of -3% and +1% respectively. The results are shown for three inertia constants (H = 1, 2 and 3 s) of the synchronous generator. In typical over/under frequency relay (81O/U), instantaneous voltage measurements are filtered prior to checking the zero crossings to detect the cycle length by sampling the waveform at 1-2 MHz [71]. In the simulations, Fast Fourier Transform (FFT) with anti-aliasing fil-

ters was used to measure the frequency through instantaneous voltage measurements at the synchronous generator terminal. Fourth order low-pass Butterworth filter was used for smoothing the measured frequency signal. The graphs in Fig. 4-1 show that there is a positive swing in the system frequency just after the islanding event, even for the positive power imbalances. This happened due to the response of the fixed speed induction generator, which had a low inertia (0.5 s). There was a small sudden drop in microgrid frequency when the grid was disconnected (which is not that visible in Fig 4-1). This caused the power output of the induction generator to increase [72] introducing an initial positive swing in the frequency.

Fig. 4-1 shows that it takes more than 2 s to detect the islanding using under frequency relays, depending on the power imbalance and system inertia. Fig. 4-1(a) shows that the islanding could not be detected at -3% power imbalance if under-frequency relays were used for the case of H = 3 s. Also it was not required to shed loads for the two power imbalances considered under any inertia level of the microgrid.

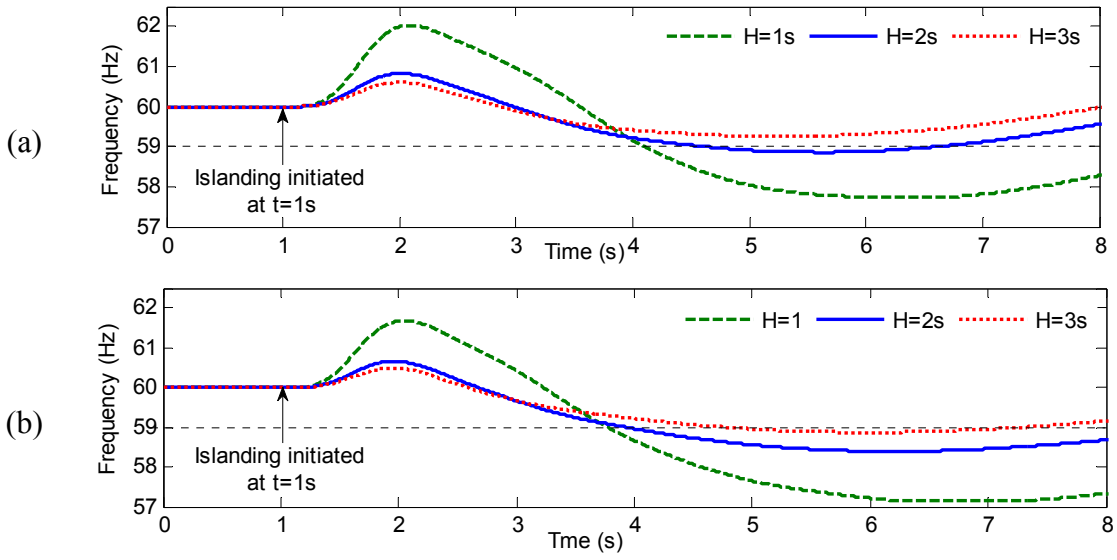

Fig. 4-1 The time variation of frequency to an islanding of the microgrid at t=1s without load-shedding (controls changed instantly) at power imbalance of (a) -3% (b) +1%.

4.2.2 Rate of Change of Frequency Response

Rate of change of frequency relay (ROCOF) is one of the most common types of anti-islanding relays used with the DGs. Typical settings of the ROCOF relay for a 60 Hz system varies from ±0.1 Hz/s to ±1.2 Hz/s [11], [73].

System rate of change of frequency for an islanding event at t = 1 s with power imbalances of -3% and +1% are shown in Figs. 4-2 (a) and (b) respectively. Table 4-1 presents the response times of ROCOF relay for different power imbalances and different synchronous generator inertia constants at two different relay settings (0.5 Hz/s and 1.2 Hz/s). For this particular test system, ROCOF relays presented very high rate of nuisance tripping when the relay settings were low (< 0.5 Hz/s).

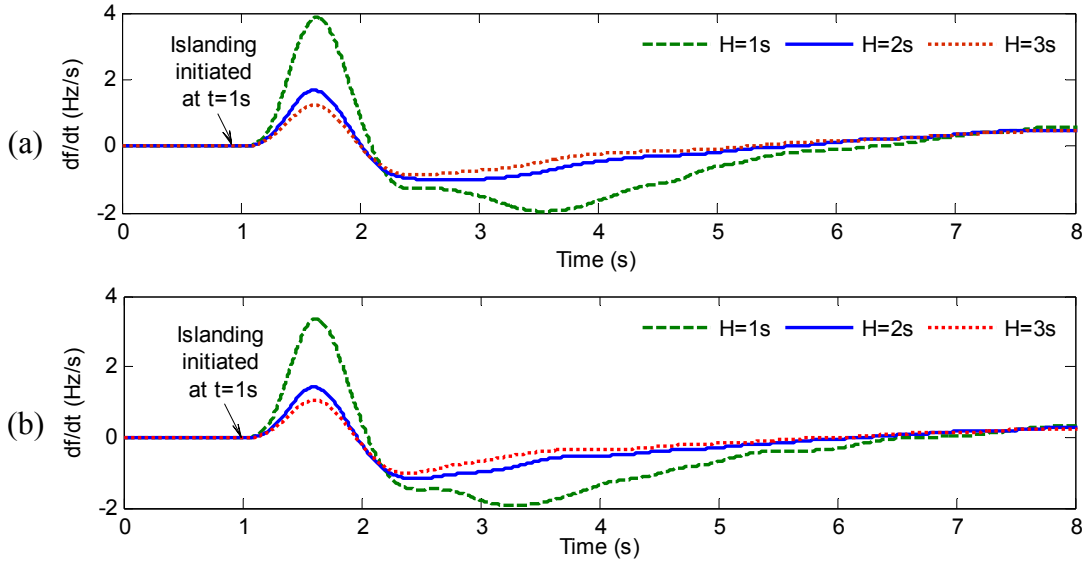

Fig. 4-2 System rate of change of frequency response to an islanding at t=1s without load-shedding (controls changed instantly) at power imbalance of (a) -3% (b) +1%.

Table 4-1 ROCOF relay response times

Inertia Constant of Synch Gen, *H* (s)	Response time of the ROCOF Relay (s)			
	-3% power imbalance		1% power imbalance	
	±0.5 Hz/s	±1.2 Hz/s	±0.5 Hz/s	±1.2 Hz/s
1	0.234	0.318	0.244	0.330
2	0.299	0.444	0.321	0.488
3	0.335	0.590	0.361	not detect

The results indicated that for both relay settings tested, ROCOF relays took more than 0.2 s to detect the power islanding under any inertia level and power imbalance. The detection time increased with the increasing inertia constant. At higher settings (1.2 Hz/s), the ROCOF relay did not detect the islanding events at low power imbalances (+1%) with higher inertia (e.g. synchronous generator inertia, H = 3s) in the system.

4.2.3 Voltage Response

Under voltage relay was discussed as an anti-islanding relay under literature review in Chapter 2. The relay settings according to [10] were given in Table 2-3 and these settings are particularly defined for anti-islanding.

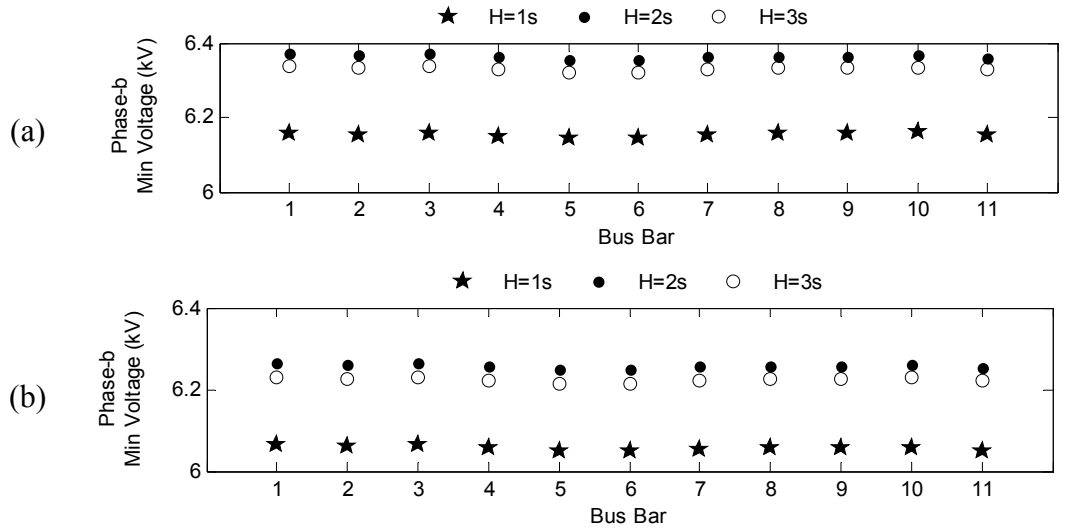

Fig. 4-3 Minimum voltage observed at Phase-b of each busbar for an islanding of the microgrid at t=1s without load-shedding (controls changed instantly) at power imbalance of (a) -3% (b) +1%.

This microgrid was unbalanced due to uneven load distribution among the phases. Unbalanced load-flow study in Chapter 3 showed that Phase-b had the lowest voltages in all the busbars. Therefore, the behavior of Phase-b voltage, which was the worst case, is illustrated in Fig. 4-3 for the same islanding events discussed above. Fig. 4-3 presents the minimum voltages observed on Phase-b of all busbars in the system. The unbalanced load-flow study showed that Bus-6 had the lowest voltage of the system under all loading conditions considered. This minimum voltage observed at Phase-b, was in-between 50% and 88% of the rated voltage. According to the standards [10], the maximum clearing time of the under voltage relay is 2 s in such a condition.

4.2.4 Summary

In summarizing the observed results, for this microgrid test system, for the power imbalances considered, islanding detection through under frequency or under voltage relays would take more than or nearly 2 s for any inertia level while a ROCOF relay taking more than 0.2 s. Study in [73] reveals similar results under an experimental study using commercial relays. Reference [17], which reviews islanding detection methods, declares that active methods take longer time than passive methods to detect islanding. Telecommunication based methods such as transfer trip schemes would be much faster but the detection time depends on the communication method, and in general it is in-between 30 ms and 1.7 s. Also, compared to passive and active methods, transfer trip schemes are costlier and complex to implement [14], [22].

4.3 Effect of the Control Mode Transition Delay on System Stability

When the microgrid is islanded, the synchronous generator control mode is changed from droop control to isochronous operation. The duration it takes to trigger the change of control mode of the synchronous generator (the *control mode transition delay*, $\Delta\tau$) depends on the response time of the islanding detection relay. In order to study the system behavior under different control mode transition delays, the control mode of the synchronous generator was changed after predetermined time durations ($\Delta\tau$ = 0 s, 0.05 s, 0.1 s, 0.2 s,... 2 s) from the time of islanding event initiation. The operating points of synchronous generator, VSC based source and the wind farm were set at 0.9 pu, 1 pu and 0.6 pu respectively at the time the microgrid was islanded. Different cases were simulated by keeping the inertia constant of the wind farm constant at 0.5 s, but changing the synchronous generator inertia (H) to 1 s, 2 s and 3 s.

4.3.1 Effect on Load Shedding and Frequency

Fig. 4-4 depicts the amount of total load shed for changing $\Delta\tau$ (0, 0.05, 0.1,…2 s). Results are shown for four different power imbalances (-8%, -3%, +1% and +30%).

To further illustrate the system behavior in transition period, frequency measured at the synchronous generator terminal under selected different transition delays ($\Delta\tau$ = 0.05, 0.2, 0.5 and 2 s) is illustrated in Figs. 4-5 and 4-6. Fig. 4-5 shows the time variation of microgrid frequency for an islanding event resulting -3% power imbalance while Fig. 4-6

showing the time variation of microgrid frequency at +1% power imbalance. The frequency variations are shown for three different inertia constants of the synchronous generator.

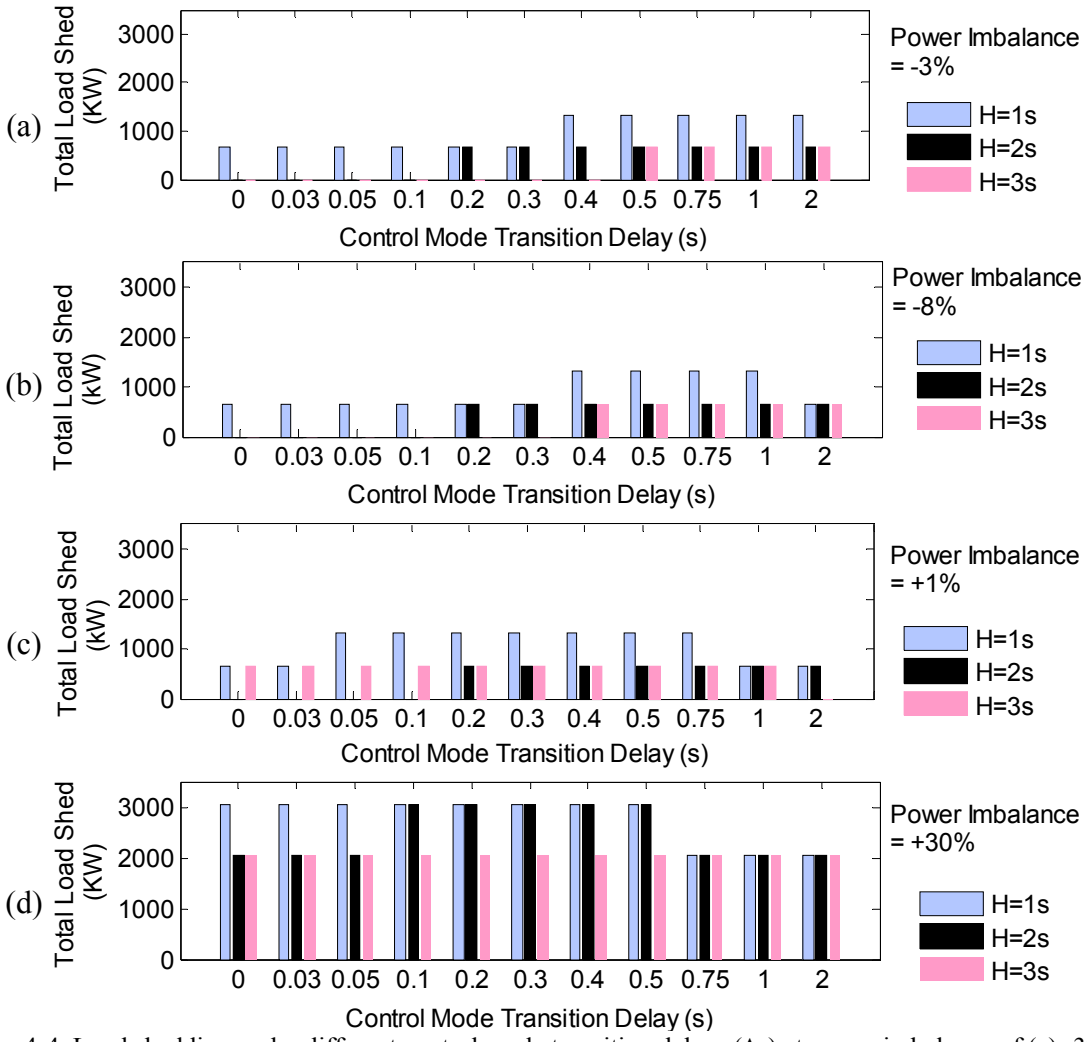

Fig. 4-4 Load shedding under different control mode transition delays ($\Delta\tau$) at power imbalance of (a) -3%, (b) -8%, (c) +1% and (d) +30%.

For the cases of -3% and -8% power imbalances, corresponding to Figs. 4-4(a) and (b), if the control mode was changed without any delay (i.e. if $\Delta\tau = 0$ s), it was not required to shed any load to stabilize the frequency for H = 2 s or 3 s of the synchronous

generator. However, according to Fig. 4-4(a), which corresponds to -3% power imbalance, the stage-1 of the load shedding scheme was shed at both cases: i) if $\Delta\tau \geq 0.2$ s, when H = 2 s and, ii) if $\Delta\tau \geq 0.5$ s, when H = 3 s. Similarly, if synchronous generator inertia constant, H = 1 s, then only one stage of loads was required be shed to stabilize the system frequency and voltage. But, if $\Delta\tau \geq 0.4$ s, two stages of loads were shed when H = 1 s.

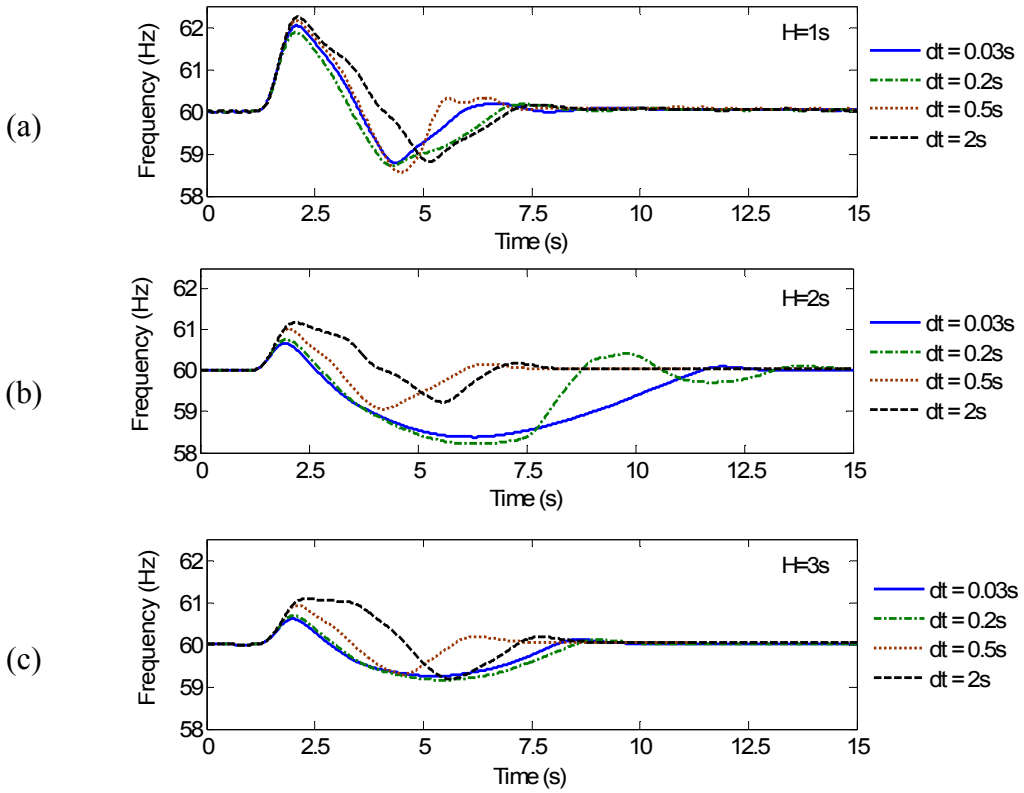

Fig. 4-5 Frequency variations under different control mode transition delays ($\Delta\tau$) for an islanding resulting -3% power imbalance with synchronous generator inertia, (a) H=1s, (b) H=2s, (c) H=3s.

Fig. 4-5 illustrates these further by time variation of microgrid frequencies at each event. Frequency swings had been introduced in the system due to the unnecessary load shedding (shedding of more loads than what is required to stabilize the frequency and voltage of the system) occurred. With H = 2 s of the synchronous generator, when $\Delta\tau$ =

0.2s, load was shed through the back-up load shedding step, which can be clearly observed from Fig. 4-5 (b).

Fig. 4-4(b) corresponds to an islanding of -8% power imbalance. It showed a similar trend as that of a -3% power imbalance. However, two noticeable differences existed in the two cases (Fig. 4-4(b) compared to Fig. 4-4(a)): (i) loads started to shed if $\Delta\tau \geq 0.4$s with H = 3 s and (ii) if $\Delta\tau = 2$ s with H = 1 s, there was again only one stage of loads shed, while two stages of loads were shed when $0.4\text{s} \leq \Delta\tau < 2\text{s}$.

For an islanding of +1% power imbalance, if $\Delta\tau = 0$ s, one stage of loads was required to be shed for H = 1 s and 3 s, while it was not required to shed any load for H = 2s. However, Fig. 4-4(c) shows that if $0.05\text{ s} \leq \Delta\tau < 1$ s with H = 1 s, then two stages of loads were shed. With H = 2 s, if $\Delta\tau \geq 0.2$ s, one stage of loads was shed, introducing frequency swings in the microgrid. When H = 3 s, only one stage of loads was shed as long as $\Delta\tau <$ 2 s, but there was no load shed when $\Delta\tau = 2$ s. The frequency variations corresponding to these events are illustrated in Fig. 4-6.

Fig. 4-4(d) corresponds to the load shedding at a power imbalance of + 30%. If $\Delta\tau =$ 0 s, all four stages of loads were required to be shed with H = 1 s. However, only three stages of loads were shed when $\Delta\tau \geq 0.75$s. Although, only three stages of loads were required to be shed with H = 2 s or 3 s to stabilize the frequency and voltage of the system, all four stages of loads were shed when $0.1\text{s} \leq \Delta\tau < 0.75$ s with H = 2 s. It was noticeable that the effect of control mode transition delay on system frequency was more significant and sensitive at low power imbalances and at low inertia levels of the microgrid.

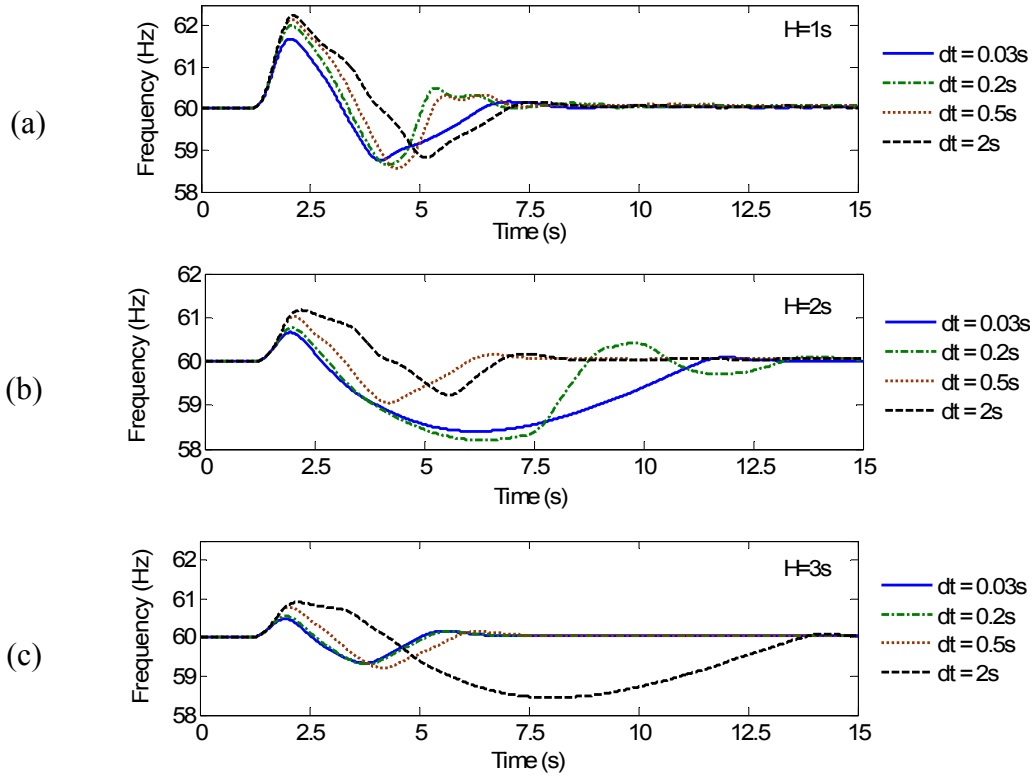

Fig. 4-6 Frequency variation under different control mode transition delays ($\Delta\tau$) for an islanding resulting +1% power imbalance with synchronous generator inertia, (a) H=1s, (b) H=2s, (c) H=3s.

It was noticeable from Figs. 4-4(b), 4-4(c) and 4-4(d) that the amount of load shed sometimes reduces back suddenly at longer control mode transition delays > 0.75 s. This happens because of the sustained voltage depression the system experience with longer control mode transition delays, which is discussed in the next section. With the voltage depression, the relative power consumption of RL loads in the microgrid reduces, which results in lower rate of change of frequency in the system.

4.3.2 Effect on System Voltage

Fig. 4-7 presents the voltage observed at the phase-b of the synchronous generator terminal (Bus-10) for two different control mode transition delays ($\Delta\tau$ = 0.03s and 2s). The

simulation results are shown for the case of +1% power imbalance at the time of islanding, for different synchronous generator inertia constants (1 s, 2 s and 3 s).

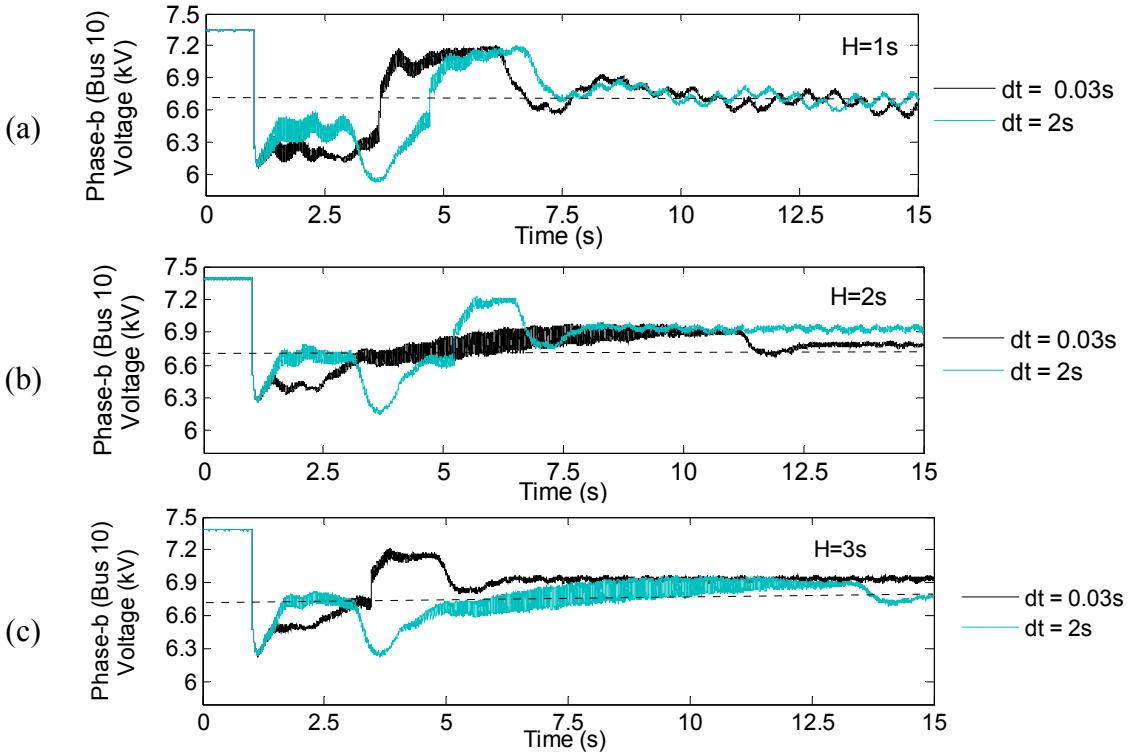

Fig. 4-7 Voltage response at Phase b of Bus 10 during the transition period at power imbalance of +1% with synchronous generator inertia, (a) H=1s, (b) H=2s, (c) H=3s.

The horizontal line in each graph of Fig. 4-7 corresponds to the 88% of rated voltage. According to IEEE standard 1547-2003 [10], the maximum tripping time for generator terminal voltages in-between 50% and 88% of the rated voltage is 2 s (Table 2-3). These protection settings may need to be adjusted by increasing the time delay settings, in applying to a microgrid type of setup to avoid spurious tripping of the generator. However, it can be observed from Fig. 4-7 that with the increasing control mode transition delay (e.g. $\Delta\tau$ = 2 s), there is a high tendency for sustained voltage depressions. This is further

illustrated by Fig. 4-8, which shows the time duration the Phase-b of Bus-10 voltage being less than 88% for different microgrid inertias. It also shows the importance of having a higher inertia level to overcome the long duration voltage depressions.

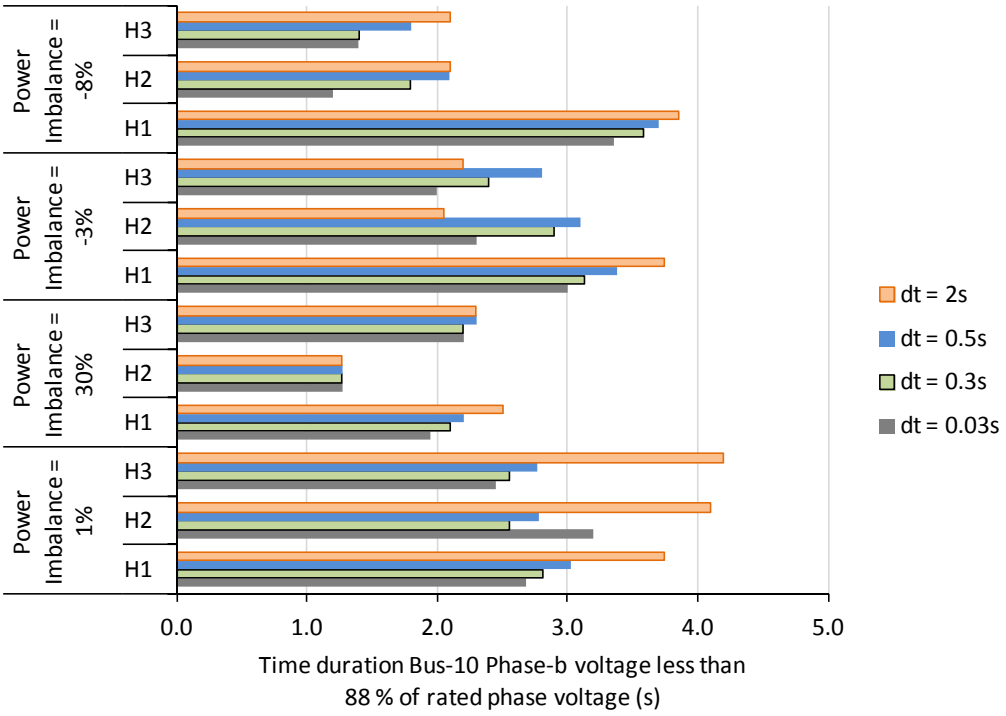

Fig. 4-8 Time duration the Phase-b Bus-10 voltage being less than 88% with synchronous generator inertia, H = 1s, H = 2s and H = 3s.

4.3.3 Critical Control Mode Transition Delay

The simulation results indicate that there is a *"critical control mode transition delay"* ($\Delta\tau_{critical}$). This can be defined as the control mode transition delay on and beyond which the resulting microgrid frequency and voltage responses significantly deviate from that resulting with control mode transition without any delay ($\Delta\tau$ = 0s). $\Delta\tau_{critical}$ for each test case is shown in Table 4-2.

Table 4-2 Critical control mode transition delay ($\Delta\tau_{critical}$)

Inertia Constant of Synch Gen, H (s)	Critical Control Mode Transition Delay ($\Delta\tau_{critical}$) ; (s)			
	-3% power imbalance	-8% power imbalance	+1% power imbalance	+30% power imbalance
1	0.40	0.40	0.05	0.75
2	0.20	0.20	0.20	0.10
3	0.50	0.40	2.00	> 2.00

If idle backup generation is available to support some of the microgrid loads, protection settings may need to be adjusted. Idle generation is usually set to power up within 100 ms after losing the utility grid, and such a situation will appear like a loss of a load in an islanded microgrid. In the transition, this situation improves the stability, if microgrid was importing power at the time of islanding. The responses will be similar to that of -8% power imbalance, if the microgrid was exporting initially. Under this situation, over frequency tripping of generators is possible if microgrid inertia is low ($H \leq 1$ s).

The results summarized in Table 4-2 lead to the conclusion that, for the microgrid network considered in the study, having a control mode transition delay less than 0.05 s ensures that the network behaves as if the controllers are changed without any delay. Taking more than 0.05 s for changing the control mode could lead to undesirable behavior such as shedding of too many loads in the microgrid, long duration voltage depressions and generator tripping through under voltage relay if set according to Table 2-3. The system became more robust during control mode transition with higher inertia constants ($H > 2$ s) for this 6 MW microgrid system. Under such high microgrid inertia, the critical transition time period shifted towards 0.4 s from 0.05 s, the value observed at lower inertia levels ($H < 2$ s). These findings support the reported work on requirement of operating mode transition delay for angle stability in [69], despite the use of two contrast-

ing control algorithms and different microgrid test systems. According to [69], real power control of the critical generator of a MV microgrid needs to be activated within 2 to 5 cycles to avoid potential angle instabilities. The microgrid considered in [69] has a 5 MVA synchronous generator and a 2.5 MVA VSC interconnected DC source, which is considered as the critical generator. The study further shows that waiting for 500 ms after islanding process to change the real power control of the VSC based generator leads to angle instability of the synchronous generator.

4.4 Concluding Remarks

The work and findings of the study on microgrid control mode transition period was presented in this chapter. The results in Section 4.2 confirmed the known fact that passive islanding detection methods would not be satisfactory when near zero power balance exists in the microgrid.

The observed results revealed that if the control mode is changed within a certain time period, the microgrid attains the same frequency and voltage responses as that of a changeover without a delay. In low inertia microgrids, delaying the control mode transition period above a critical time period could lead to unnecessary load shedding. At higher embedded inertia, a microgrid becomes more robust, and tolerates a longer transition delay.

The above conclusions pointed to the benefits of having a fast and reliable islanding detection device to activate control mode transition. Transfer trip schemes, if selected with the satisfactory fast responding communication method would be a solution. How-

ever, as discussed in the literature, transfer trip method becomes complex with the increased number of DGs and it is a costly implementation. Therefore, it is important to research in finding fast responding reliable islanding detection techniques suited for microgrids with reliability objectives.

The conclusions were drawn for a substation level microgrid with a synchronous generator and no energy storage. Therefore, these results may not be directly applicable to microgrids with fast responding battery storage.

Chapter 5

Voltage Balancing and Synchronizing

Microgrids can operate in parallel with the grid or as a power-island. They are thus, expected to perform seamless transition from parallel to islanded operation and vice versa. The previous chapter discussed the performance of the microgrid in transition from parallel to islanded operation. This chapter reports the investigations on microgrid synchronization to the utility grid, and proposes some possible simple solutions for voltage balancing. It shows that the existing synchro-check relay with a circuit breaker is sufficient to reconnect an islanded, highly unbalanced microgrid back to the utility grid.

5.1 Background

When reconnecting a microgrid operating in the islanded mode to the utility grid, voltage, frequency and phase criteria must be satisfied. Synchronizing a microgrid having several generators with different characteristics is more challenging than synchronizing a single generator with the grid. As previously discussed in Section 2.2 under literature review, in the IEEE standard 1547.4-2011 [33] three methods of synchronization has been identified: (i) active synchronization where there is a control mechanism to match the voltage,

frequency, and phase angle of the island system to the utility grid, (ii) passive synchronization, which employs a synchronization check for paralleling, and (iii) open-transition transfer where loads and DGs in the island are de-energized before reconnecting to the grid. The documented research on microgrid resynchronization are mostly focused on converter based DGs and they are mostly active synchronizing methods [34]-[37].

This study considered a microgrid with highly unbalanced loads, and investigated the passive synchronization of the microgrid using commercially available synchro-check relays [40],[74] with the support of switched capacitor banks for voltage balancing. The use of switched capacitors for voltage balancing had been studied in few previous research [38]. The guidelines of the local utility outlined in, "*Technical requirements for connecting distributed resources to the Manitoba Hydro distribution system*" [67], was particularly used in studying the microgrid voltage control and synchronization performance. Manitoba Hydro had used the IEEE standard 1547-2003 [10] as the basis for its interconnection guidelines. Thus, the contribution of this study is the analysis of the impact of applying existing DG synchronization criteria in the IEEE Standard 1547-2003 [10], to a typical medium voltage microgrid with unbalanced loading, as suggested in the IEEE Standard 1547.4-2011 [33].

Simulation studies were carried out with the assumption that the initial operating points of the generators were already set by the management agent. Therefore, it was considered that the power output of synchronous generator, VSC based source and the wind turbine were at 0.9 pu, 1 pu and 0.6 pu respectively at the time islanding happened for all the simulations. The inertia constant of the wind turbine generator and the synchronous generator were 0.5 s and 3 s respectively.

5.2 Switched Capacitors for Voltage Balancing

One aspect studied was the use of switched capacitors for voltage support and voltage balancing in a microgrid with unbalanced loads. The capacitor bank was designed based on the commercially available capacitor units considering their ratings and switching logics [75]-[76]. The capacitor bank connected at the POI of the microgrid consisted of three parallel units and single pole switching was used for voltage balancing.

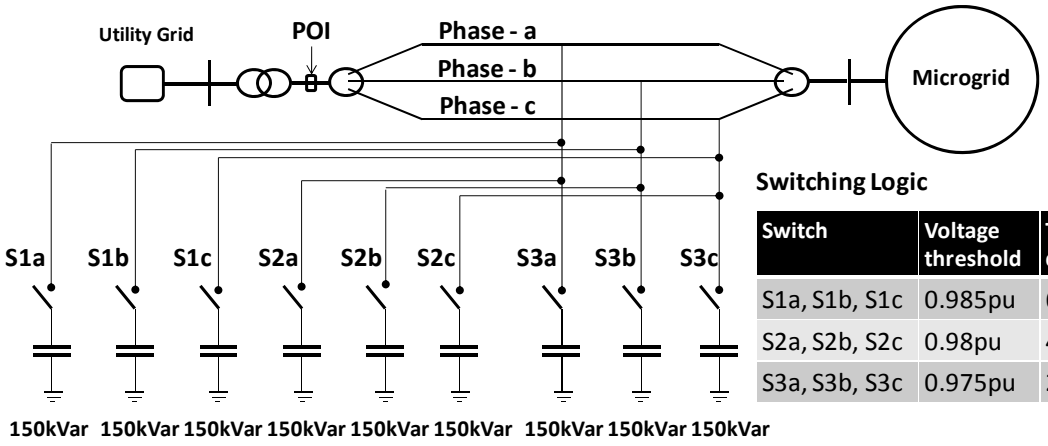

Switching Logic

Switch	Voltage threshold	Time delay
S1a, S1b, S1c	0.985pu	6s
S2a, S2b, S2c	0.98pu	4s
S3a, S3b, S3c	0.975pu	2s

Fig. 5-1 Switched capacitor bank for voltage balancing in the microgrid.

Capacitors were switched depending on the measured phase voltages; i.e. if the phase voltage dropped below the set value for duration greater than a specified time delay, the appropriate capacitor was connected to the system [75]. In order to minimize transients, capacitor switching was initiated only if the frequency was within ± 0.1 Hz from the nominal. Time delays for each stage were selected inversely proportional to the difference between the nominal voltage and the threshold voltage for the stage. Fig. 5-1 shows

the arrangement of the three-stage voltage balancing capacitor bank rated at 150kVar/phase/stage.

5.3 Synchro-check Relay

The synchro-check relay measures the magnitude, phase angle and frequency differences between the voltages on either side of the circuit breaker. The relay allows the circuit breaker closing only if the measured values are within some preset limits based on the synchronization requirements. The specific requirements that need to be satisfied in re-connecting a DG to the system are shown in Table 5-1 [67]. The guidelines in [67] specifically states that the DG must be reconnected only after the system has stabilized and the RMS voltage has returned to normal levels for a minimum of 5 minutes. This requirement is in agreement with the IEEE Standard 1547-2003 [10]. The standards applied for DGs rated above 1500 KVA were considered applicable to the microgrid as a whole.

Table 5-1 Standards for DG synchronization [67]

Total Generation	Frequency Difference	Voltage Difference	Phase Angle Difference
0 – 500 KVA	0.3 Hz	10%	20°
>500 – 1500 KVA	0.2 Hz	5%	15°
>1500 KVA	0.1 Hz	3%	10°

A synchro-check relay can be implemented using phase voltages in a balanced system or considering the positive sequence components in applying to an unbalanced system. However, in practical implementations, the synchro-check relay measures only one of the line-to-line voltages [40], [74][77]. The existing synchro-check relays utilize zero-

crossing technique to find the phase angles [40], [74]. The same techniques were used in this study.

If the requirements for synchronization of a DG with Manitoba Hydro's grid, outlined in Table 5-1, were applied to synchronization of the microgrid, the synchro-check relay settings should have been as indicated on the logic diagram shown in Fig. 5-2. The nominal voltage and frequency of the microgrid at POI was 13.2 kV, 60 Hz. A circuit breaker time delay of 83 ms [77] was introduced to emulate the practical scenario. The threshold of voltage difference was initially set at 0.03 pu with a time delay of 5 s for the study. This time delay had to be maintained to avoid spurious switching during transients. However, the standards [67] requires this waiting time to be 5 mins long, but 5 s delay was considered here to limit the simulation duration to a reasonable value.

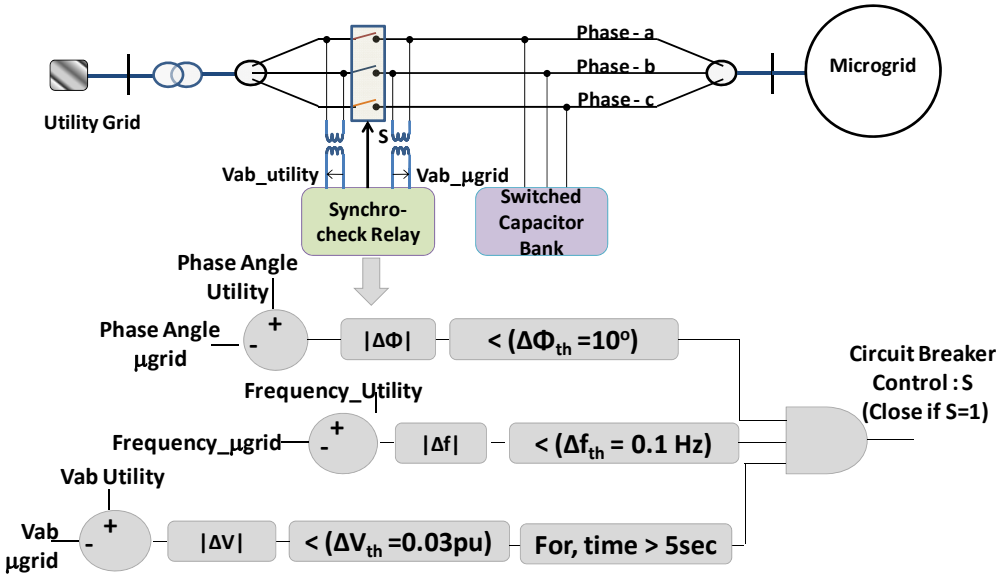

Fig. 5-2 Microgrid synchronizing function in accordance with [66].

5.4 Role of Switched Capacitor Banks

5.4.1 Effect on System Voltage

In order to examine the effect of capacitors on voltage, first an islanding event was simulated. Just before the islanding, microgrid was importing 40% of the real power from the utility grid (+ 40% power imbalance). Fig. 5-3 shows the variations of phase angle difference across the breaker, as well as the frequency, and line voltage magnitudes measured on either side of the circuit breaker. Variations are shown with and without the switched capacitor bank at the POI.

When islanded at t = 5 s, first the load shedding scheme was activated to stabilize the frequency. In the case of microgrid equipped with switched capacitor bank, capacitors were then switched-in according to the set logic to correct the voltage levels.

Fig. 5-3 also gives the highest values observed in the phase angle, frequency, and voltage differences, as well as the highest voltage deviation and voltage unbalance observed during the stable islanded operation under both scenarios. It is clear from Fig. 5-3 that the voltage magnitude difference requirement for synchronizing ($\Delta V < 0.03$ pu) was not met when the microgrid was operated without the switched capacitor bank. Introduction of the switched capacitor bank had not only raised the voltage to a value that meets the synchronization requirements, but also reduced the maximum voltage deviation from -9.73% to -4.74%, and the voltage unbalance from 5.24% to 1.85%.

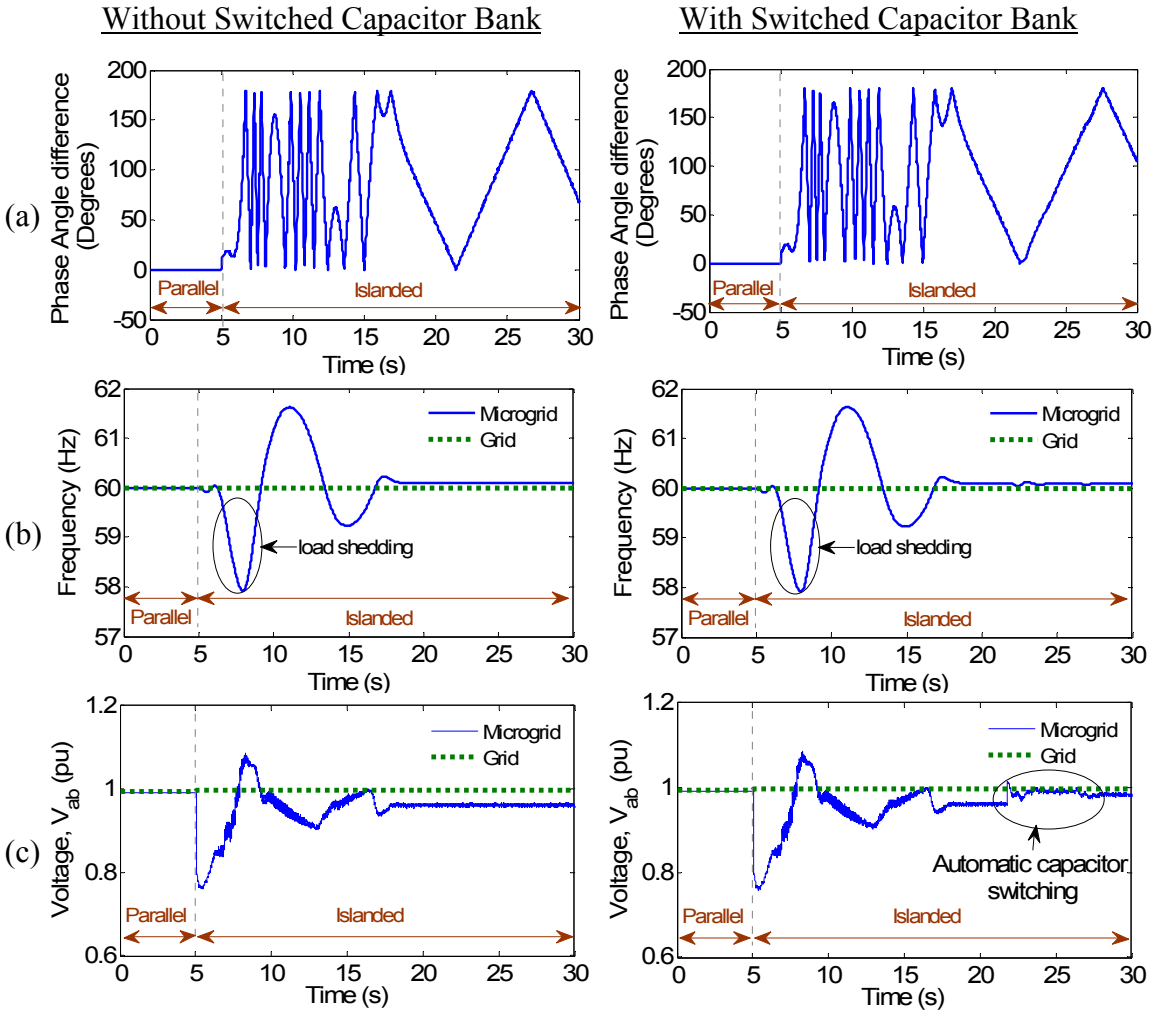

Fig. 5-3 Variations of synchro-check relay parameters for an islanding at t=5s (40% power imbalance) (a) Phase angle difference, (b) frequency, (c) V_{ab} line-to-line RMS voltages beside the circuit breaker, (d) summary.

Aforementioned study was repeated for reconnecting the microgrid back to utility after an islanding event that created a -7% power imbalance (microgrid was exporting power to the grid before the islanding event). The frequency deviation between the mi-

crogrid and the utility grid during the islanded operation was around 0.06 Hz, but the line voltage difference across the circuit breaker was 0.038 pu, without the capacitors. With switched capacitors, this difference was reduced to 0.005 pu, satisfying the specifications for synchronization. In this case, the islanded micorgrid was not able to satisfy the voltage standards without switched capacitor support: the maximum voltage deviation of -9.5% and the maximum voltage unbalance of 5.95% exceeded the allowable limits. However, with the provision of switched capacitor bank, the maximum voltage deviation and voltage imbalance were reduced to -5.4% and 3.6% respectively.

The above discussed voltage regulation and balancing achieved with the support of switched capacitors at POI of microgrid is summarized in Table 5-2 for microgrid islanded operation at both +40% and -7% power imbalances. Table 5-2 shows that even though the capacitor bank was connected at microgrid POI, the voltage of the weakest bus (Bus-6) was improved by nearly 5% and the voltage unbalance in the islanded microgrid was reduced by nearly 3%.

Table 5-2 Summary of maximum voltage deviation and voltage unbalance

Power Imbalance created when islanding	Max voltage Deviation at Bus-6		Voltage unbalance	
	No Cap.	With Cap.	No cap.	With cap.
+ 40%	-9.73%	-4.74%	5.24%	1.85%
-7%	-9.50%	-5.40%	5.95%	3.60%

The fact that this microgrid test system did not meet the voltage requirements in the islanded operation was discussed in Chapter 3 as well. With the connection of switched capacitors at the POI, microgrid system satisfied the voltage standards specified in [67].

5.4.2 Effect on Microgrid Synchronizing

Fig. 5-4 shows the simulation results for reconnecting the islanded microgrid back to the utility. Prior to the reconnection, the microgrid was operated in the islanded mode as a result of an islanding event that resulted in a +40% power imbalance. Thus, this can be considered as reconnection after the islanding event shown in Fig. 5-3. Fig. 5-4(a) shows the variations of the instantaneous voltages on two sides of the circuit breaker, Figs. 5-4(b) and 5-4(c) show the grid side instantaneous current and the power outputs of all the sources respectively.

Fig. 5-4 presents these results for three scenarios: Scenario 1: forced reconnection of the microgrid to the utility grid at a phase angle deviation of 20^o ($\Delta\Phi = 20^o$) without the switched capacitor bank, Scenario 2: same as Scenario 1 but $\Delta\Phi = 10^o$, and Scenario 3: reconnection using synchro-check logic in Fig. 5-2 with the support of switched capacitor bank to meet the voltage criteria. Note that, the voltage condition for synchronization could not be met without the capacitor bank support (explained with respect to Fig. 5-3).

The above three scenarios were simulated for the islanding event with -7% power imbalance discussed in the Section 5.4.1. Even though the two islanding events created different system conditions in the islanded microgrid, variations of the voltage and current during the resynchronization after -7% power imbalance islanding event were very similar to those observed in the case of +40% power imbalance islanding event, shown in Fig. 5-4. Table 5-3 summarizes the system conditions at the time of reconnecting the microgrid to utility grid (at the time of closing the breaker "*Br1*"), for the six cases.

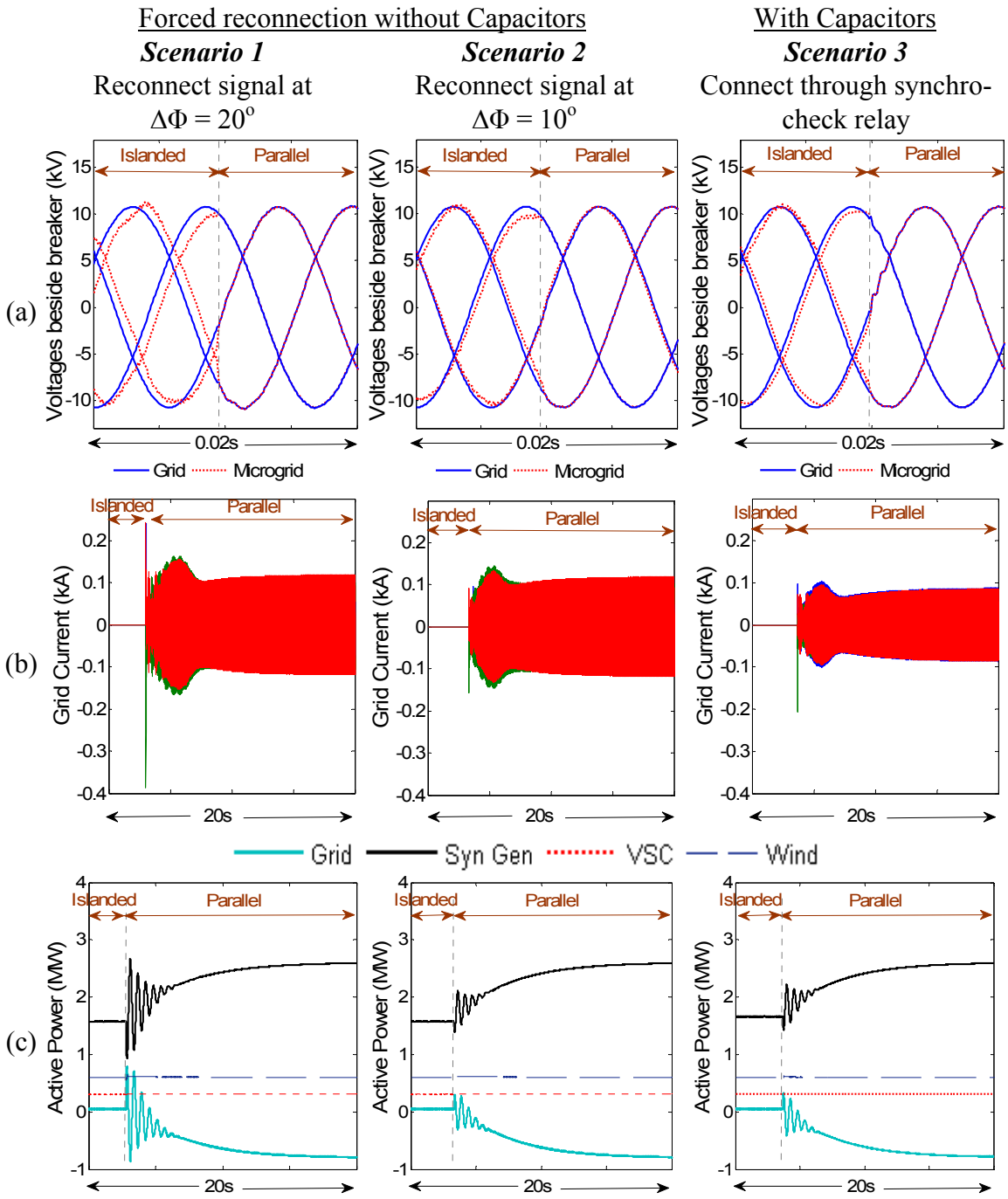

Fig. 5-4 Variations of (a) voltages beside the breaker, (b) grid side current output, (c) power outputs of all the sources for reconnecting the microgrid back to utility after an islanding of +40% power imbalance.

Table 5-3 System conditions at the time of reconnecting the microgrid to the utility grid

Power Imbalance	Detail	Forced reconnect without capacitors		With capacitors
		Scenario 1	***Scenario 2***	***Scenario 3***
		Reconnect signal at $\Delta\Phi = 20^o$	Reconnect signal at $\Delta\Phi = 10^o$	Connect through synchro-check relay
+40%	$\lvert\Delta\Phi\rvert$	17.28^o	7.56^o	7.56^o
	Δf	0.08Hz	0.08Hz	0.07Hz
	ΔV_{ab}	0.035pu	0.032pu	0.02pu
-7%	$\lvert\Delta\Phi\rvert$	18.36^o	9.72^o	9.72^o
	Δf	0.06Hz	0.06Hz	0.05Hz
	ΔV_{ab}	0.045pu	0.04pu	0.005pu

Table 5-3 shows that, the voltage criterion for synchronization could not be satisfied without the switched capacitors (Scenarios 1 and 2). Scenario 1 corresponds to the forceful reconnection of microgrid to the utility grid with a signal initiated at a phase difference of 20^o. In this case both voltage and phase angle criteria were violated and Fig. 5-4 (b) shows that at the time of reconnection, it had generated a current transient with a peak magnitude nearly four times the final steady state current. In scenario 2, i.e. when the phase difference was reduced to 10^o, the transient current was insignificant (only the voltage criterion was violated). As indicated by Fig. 5-4, there was no significant difference in the observed results between the forceful reconnection at 10^o phase difference (Scenario 2) and the reconnection using synchro-check relay (Scenario 3), where all criteria for synchronizing were satisfied. It should be noted that the final steady state current from the utility grid was reduced in Scenario 3 due to the switching of the capacitors. The peak transient current that was slightly higher than that in Scenario 2 could also be attributed to the capacitor bank. As shown in Fig. 5-4(c), the power outputs of the synchronous generator and the utility grid underwent a few oscillations before reaching their re-

spective steady state values. However, power outputs of the VSC and induction generator did not show significant transient variations due to reconnection event in all three scenarios. The microgrid started to export power to the utility grid after resynchronization. This happened due to the reduced load demand in the system with the load shedding in the islanded operation. Load restoration could be done once the system was stabilized (not shown in Fig. 5-4).

These results revealed that simple switched capacitor bank arrangement is sufficient to improve the voltage quality in islanded operation, although more sophisticated Var support schemes such SVCs, DSTATCOMS or energy storage systems are discussed in many studies [78]-[79]. The results also indicated that the synchronization criteria applied to individual distributed generators are satisfactory for microgrids of equivalent total generation. The effect of synchro-check relay settings in applying for microgrid reconnection was further investigated and reported in the next section.

5.5 Impact of Synchro-check Relay Settings

So far the settings of the synchro-check relay were at the maximum allowed limits for DG interconnection [67] as illustrated in Fig. 5-2. This section analyzes the impact of these settings on the microgrid synchronization performance.

Initially the frequency difference threshold was set at 0.1 Hz, which is the required limit for DGs greater than 1.5 MW of capacity. This is also, the steady state frequency deviation limit for distribution systems [67]. Therefore, it was desirable to leave the fre-

quency difference threshold of synchro-check relay at 0.1 Hz, even when applying to the MV Microgrid of nearly 6 MW of capacity considered in this study.

As observed in the results of Fig. 5-4, a lower phase difference shows a reduction in magnitudes of the current and power transients. Thus, it was desirable to set the phase angle difference threshold at the lowest possible value. The lowest possible threshold depends on the circuit breaker time delay and the slip-frequency, f_s (frequency difference between the microgrid and utility grid). The circuit breaker time delay considered in this study was 83 ms [77]. At a given slip frequency f_s , the phase angle difference between the utility grid and the microgrid voltages at the POI ($|\Delta\Phi|$) varies with the time as shown in Fig. 5-5.

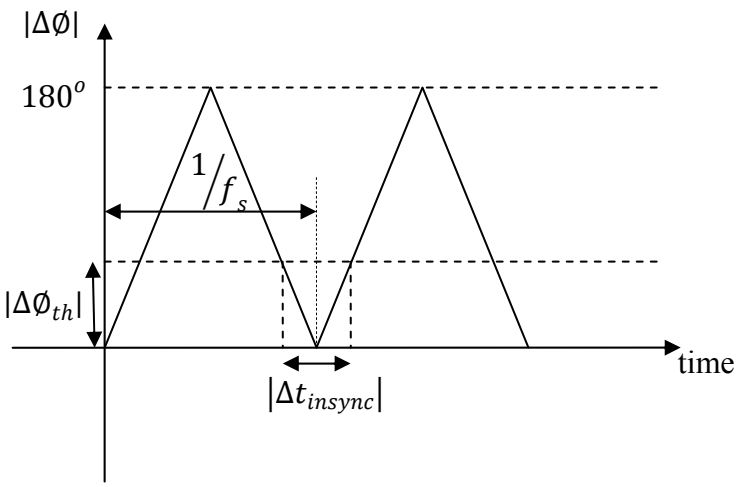

Fig. 5-5 The time variation of absolute value of phase angle difference between the utility grid and the microgrid voltages at the POI.

The relationship between the phase difference threshold, $|\Delta\Phi_{th}|$, and the time duration that phase angle difference is within the threshold, Δt_{insync}, can be derived using Fig.

5-5. If $f_{s,}$ is in Hz, and $|\Delta\Phi_{th}|$ is in degrees, the value of Δt_{insync} in seconds is given by (5.1) [77].

$$\Delta t_{insync} = \frac{|\Delta \phi_{th}|}{180 \quad f_s} \tag{5.1}$$

This Δt_{insync} should be greater than the circuit breaker time delay, which was 83 ms to ensure the microgrid reconnection within the set phase angle threshold. If $\Delta\Phi_{th}$ is 10^o then Δt_{insync} is 555 ms for the maximum possible slip frequency of 0.1 Hz. Similarly, if $\Delta\Phi_{th}$ is set at 5^o then, $\Delta t_{insyncc}$ is 277 ms, which is still much higher than the circuit breaker time delay. Therefore, threshold for phase angle difference in synchronizing the microgrid could be brought down to 5^o without any difficulty.

The threshold of voltage difference was initially set at 0.03 pu. According to the distribution system standards, the steady state voltage magnitude deviation could be as large as ±6% from the nominal value [67]. Thus, the steady state voltage magnitude difference between the utility grid and microgrid could be larger than the difference specified in the synchronization requirements. In the microgrid simulation examples considered in Section 5.4, while in the islanded mode of operation, switched capacitors were applied to support the synchronization function. The capacitors were switched-in to meet the set voltage difference threshold of the synchro-check relay. However, it was noticeable from Fig. 5-4 that the transient variations of the current (and power) following the reconnection in Scenarios 2 and 3 were not much different (since $\Delta\Phi_{th}$ was 10^o for the synchro-check relay and thus, the difference between the two scenarios was the presence of the capacitor bank). Therefore, it was explored whether the voltage difference threshold

could be set to a higher value without undue effects. Such possibility would allow reducing the number of capacitor stages and switching operations.

Table 5-4 Capacitor switching criteria for different ΔV_{th} criteria of the synchro-check relay

Switches	Time Delay (s)	Voltage Setting for Capacitor Switching (pu)	
		ΔV_{th} = 0.03pu	ΔV_{th} = 0.05pu
S1a, S1b, S1c	6	0.985	0.965
S2a, S2b, S2c	4	0.980	0.960
S3a, S3b, S3c	2	0.975	0.955

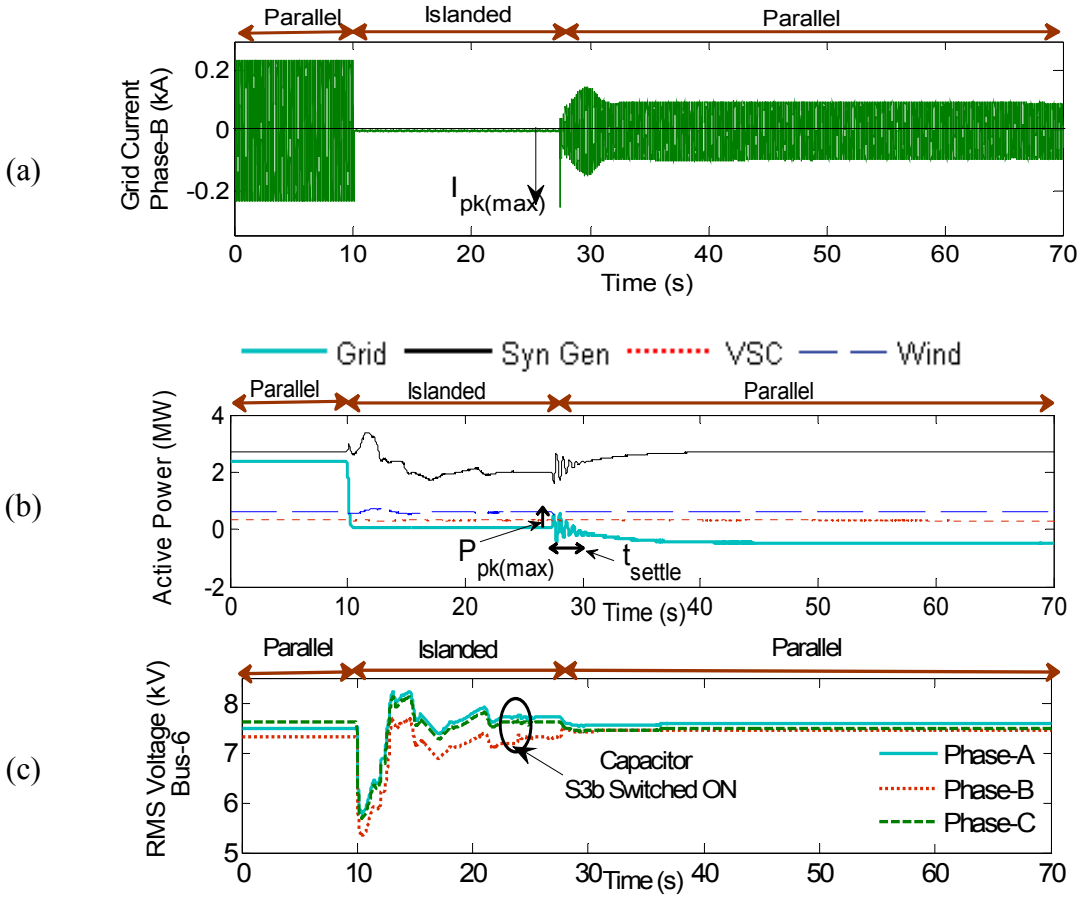

Fig. 5-6 Variations of (a) grid side Ph-b current, (c) utility grid and DG real power (c) RMS voltages of Bus-6 during islanding and reconnecting. (+40% power imbalance, ΔV_{th}=0.05pu, $\Delta \Phi_{th}$=10°, Δf_{th}=0.1Hz).

To analyze the sensitivity of voltage difference threshold (ΔV_{th}), it was set to 0.03 pu and 0.05 pu keeping the frequency difference threshold (Δf_{th}) at 0.1 Hz. Three phase angle difference thresholds ($\Delta \Phi_{th}$ = 5°, 10° and 20°) were considered. The capacitor switching voltage thresholds were adjusted as given in Table 5-4 so that the switching of the last set of capacitors results in voltage magnitudes that were just sufficient to meet the considered ΔV_{th} criteria (0.03 pu or 0.05 pu).

Fig. 5-6 presents the variation of phase-B grid current, real power outputs of all sources and the voltage of the weakest busbar (Bus-6) for an islanding event with +40% power imbalance and synchronizing it back to the utility grid after operating in the islanded mode for some duration. The results are shown for the case of Δf_{th} = 0.1 Hz, $\Delta \Phi_{th}$ =10° and ΔV_{th} = 0.05 pu.

With the aim of studying the effect of $\Delta \Phi_{th}$ and ΔV_{th} settings on smooth transition of microgrid from islanded to parallel operation, two indicators were defined.

1) Peak transient current ($I_{pk(transient)}$) is the peak instantaneous transient current due to synchronizing operation. This is illustrated as $I_{pk(max)}$ in Fig. 5.6(a)
2) Oscillation energy ($E_{oscilation}$) defined in (5-3) quantifies the oscillations in the utility active power due to synchronizing operation.

$$E_{Oscillation} = | P_{pk} |_{(\max)} \times t_{settle} \tag{5.3}$$

Where, P_{pk} is the peak grid power observed during the initial oscillations following the synchronization, and t_{settle} is the oscillations settling time. These quantities are illustrated in Fig 5-6(b).

These indices were calculated using simulations for each of the cases described earlier [Δf_{th} = 0.1 Hz, ΔV_{th} = 0.03 pu, 0.05p u, and $\Delta \Phi_{th}$ =5°, 10°, 20°]. The microgrid resynchronizing after two different islanding events, resulting in a -7% and a +40% power imbalances, were studied.

Fig. 5-7 presents $I_{pk(transient)}$ under different scenarios described previously. It shows that initial current transient was significantly large if $\Delta \Phi_{th}$ = 20°. Current transient was reduced with the lower setting of the phase angle difference. Therefore, it was desirable to use a 5° phase angle threshold to achieve a comparatively low initial current transient at the POI, in reconnecting the microgrid back to utility grid.

At both power imbalances tested, it showed that there was no significant difference in using 0.03 pu or 0.05 pu as the voltage threshold. However, if ΔV_{th} = 0.03 pu a larger capacitor bank is required at the POI to raise the voltage to meet the more strict voltage criterion.

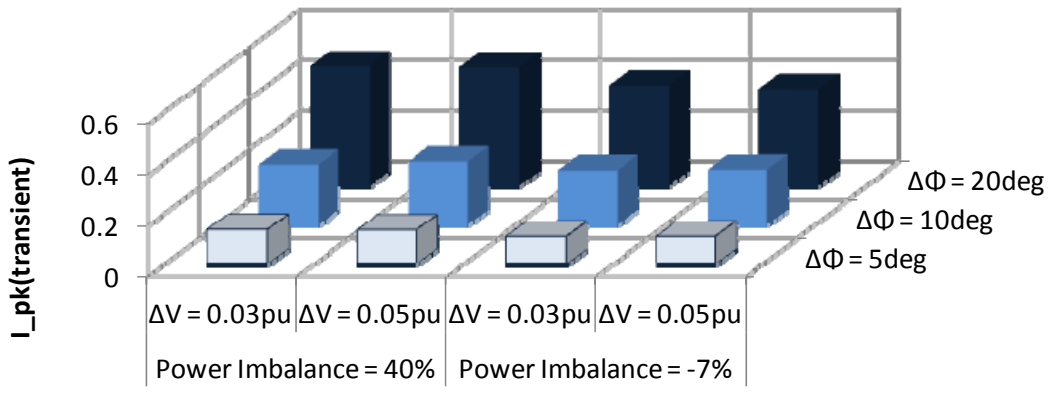

Fig. 5-7 $I_{pk(transient)}$ when microgrid is resynchronized to the utility grid after islanding resulting in +40% and -7% power imabalnce.

Table 5-5 Capacitor switching criteria for different ΔV_{th} criteria of the synchro-check relay

Case	Total reactive power injection at POI (kVar)	
	at 0.03pu	at 0.05pu
40% power imbalance	450	150
-7% power imbalance	750	600

Table 5-5 presents the total reactive power supplied at the POI by the switched capacitors for the two cases of ΔV_{th} = 0.03 pu and ΔV_{th} = 0.05 pu. When ΔV_{th} = 0.05 pu, the number of capacitor stages that were needed to be switched-in had reduced. It should be noted that even though using voltage threshold of 0.05 pu reduced the required number of switched capacitor stages, the steady state voltage limits specified in the standards [66] were not violated. For the -7% power imbalance case with ΔV_{th} = 0.05 pu, the maximum voltage deviation observed was -1.24% and the voltage unbalance was 0.58% in the islanded operation, which are well within the recommended values [67]. These observations suggested that relaxing (increasing) the ΔV_{th} setting of the synchro-check relay to 0.05 pu would not cause any power quality problems, but it could help in reducing the number of capacitor stages required at the POI.

Fig. 5-8 presents $E_{Oscillation}$ values corresponding to the same conditions as in Fig. 5-7. Fig. 5-8 shows that the use of $\Delta\Phi_{th}$ = 20^{o} resulted in significantly high $E_{Oscillation}$ values (large and longer oscillations in grid power after synchronization). Decreasing the phase angle threshold from 10^{o} to 5^{o} reduced the $E_{Oscillation}$ by a factor of three. This observation supported the previous discussions on setting the phase angle threshold of the synchro-check relay at the POI of microgrid at a value lower than the maximum permitted under the standards [67]. Simulation results in Fig. 5-8 also show that if the phase angle

threshold was set below 10°, the oscillation energy remained nearly unchanged when the voltage threshold of the synchro-check relay was increased from 0.03 pu to 0.05 pu, for both power imbalances simulated.

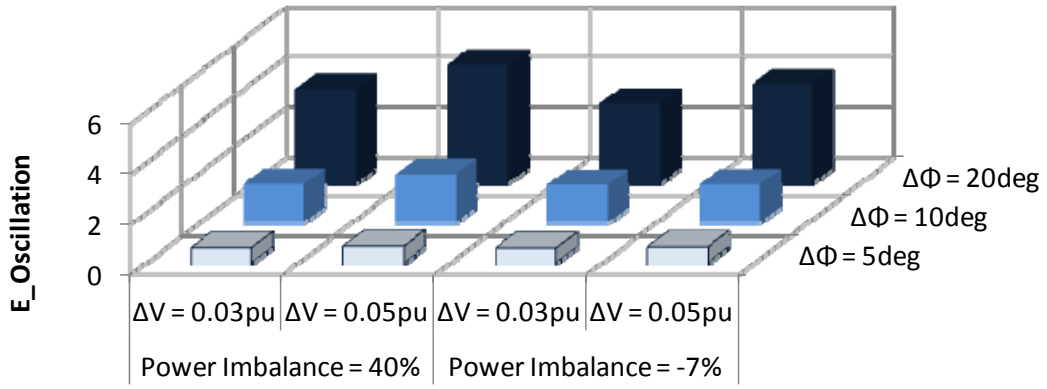

Fig. 5-8 $E_{Oscillation}$ when microgrid is resynchronized to the utility grid after islanding resulting in +40% and -7% power imbalnce.

The total generation capacity of the microgrid test system considered in this study was less than 5 MW, with a major portion (3 MW) coming from a synchronous generator. The simulation results suggested that for a MV microgrid with similar characteristics, the maximum voltage difference criteria for synchronization could be relaxed to 0.05 pu without undue effects, if the switchgear at the POI permits lowering the phase angle threshold below 10° (say to 5°). Relaxation of the voltage threshold criteria helped reducing the number of capacitor bank stages used for voltage support (and balancing). This ensured a seamless transition from islanded to parallel operation while satisfying the steady state voltage limits specified in standards during both parallel and islanded operation.

5.6 Concluding Remarks

This chapter reported the application of switched capacitor banks for voltage balancing in an islanded microgrid, and for achieving the voltage magnitude criteria for synchronization. The study considered passive synchronization with traditional synchro-check relays. The findings showed that with simple switched capacitors at the POI, it was possible to meet the voltage quality of the microgrid and synchronization requirements specified in the standards. In microgrid synchronization, the major factor that determined the smooth transition was the phase angle difference between the utility and microgrid voltages. The results also showed that, when switched capacitors were used at the POI, it was desirable to increase the voltage difference threshold of the synchro-check relay to reduce the required amount of capacitor stages at the POI. Also, the traditional synchro-check relays were quite satisfactory for microgrid synchronization.

Chapter 6

Transient Based Islanding Detection

Two previous chapters studied the transition of a microgrid from parallel to islanded operation and vice-versa. While the study on synchronization revealed that existing synchro-check relays with adjustments to the settings can be successfully used for synchronization of microgrids, the study on microgrid transition from parallel to islanded operation revealed the importance of quick detection of islanding to avoid shedding of excessive amounts of loads in the microgrid and long duration voltage depressions that could lead to tripping of the DGs through under voltage relays. As a response to this requirement, a fast transient-based islanding detection method is proposed in this chapter. The methodology involves signal processing and pattern recognition techniques. The background, relevant theory, details of implementation and the test results are presented in the next few sections through a step-by-step approach.

6.1 Background

A number of different islanding detection methods that have been proposed in the literature were reviewed in Section 2.3. The discussions in Chapters 2 and 4 identified that

among the common islanding detection methods, only telecommunication-based methods, if used with a fast communication system, would meet the required response time and the reliability demanded by a typical MV microgrid system. However, as discussed in Section 2.3, telecommunication based methods have the demerits of being costly and being complex. In general, for DG interconnection, passive islanding detection methods are preferred and widely used over the active and telecommunication based methods due to considerations such as the cost, reliability and power quality [80].

This chapter proposes a new, fast and reliable method to detect power islands using the transient signals generated during the disconnection of the grid. The methodology involves extraction of current and voltage signal energies in different frequency bands through wavelet transform and use of classification techniques.

Wavelet transform based techniques have been previously used for islanding detection, and it was discussed in Section 2.3. The proposed method differs from the previous methods because it examines the use of pattern recognition techniques in identifying the islanding condition, instead of depending on the threshold values determined by trial and error. Furthermore, it uses several wavelet coefficients corresponding to different frequency bands of the current and voltage signal transients, instead of using a complex set of indices. The final outcome is a fast and reliable islanding detection method based on decision tree classification that uses energy contents of several wavelet coefficients of current and voltage waveforms as features.

6.2 The Proposing Islanding Detection Method

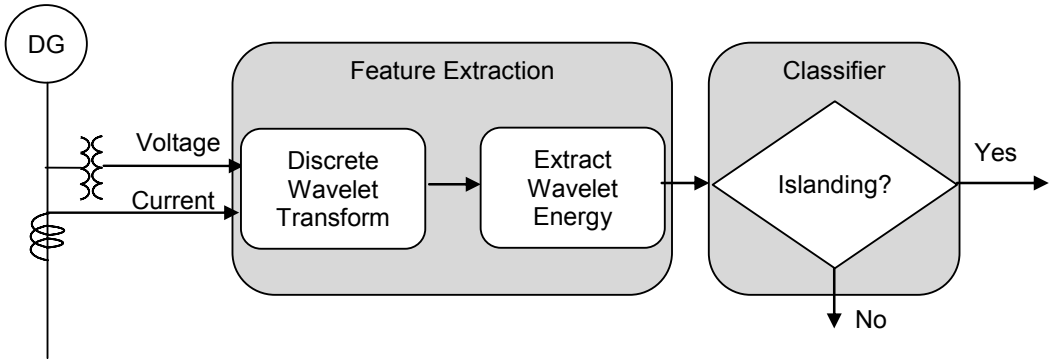

Fig. 6-1 The basic model of transient based islanding detection technique.

The basic model of the passive islanding detection method proposed is illustrated in Fig. 6-1. Transient waveforms of the currents and voltages in a power network contain unique signatures that reveal the cause of the corresponding transient event. The proposed islanding detection method was based on the hypothesis that the transients generated during the islanding event contain such a signature and a classifier could be developed to distinguish islanding events from the other disturbances. However, the event specific characteristics embedded in the transient waveforms are not directly distinguishable. Therefore, they were needed to be pre-processed to extract features that assisted fast classification response. Wavelet transformation was thus used for this purpose.

6.3 Simulation Tools and Test System

Simulation studies were carried out using PSCAD/EMTDC power system simulation software. The test system discussed in Chapter 3 was modified for the initial studies on islanding detection relay presented in this chapter. To simplify the test system, the VSC

based DC source was removed. The capacity of the wind farm was changed and both the capacity and the location of the synchronous generator were changed in accordance with the basic CIGRE MV test system and proposed DG sizes and locations in [39]. Overhead lines and the rest of the system configuration were kept unchanged from that of Fig. 3-1.

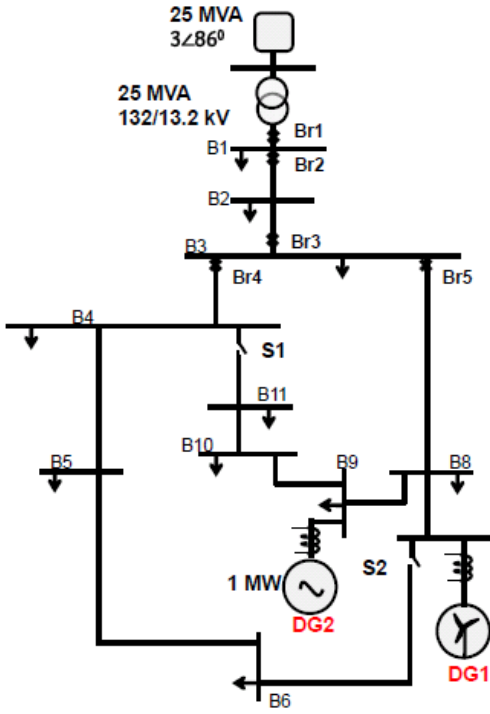

Bus	Base Load (kVA)			pf
	Ph-A	Ph-B	Ph-C	
1	250	100	300	0.9
2	300	250	200	0.95
3	83.33	500	83.33	0.9
4	200	100	100	0.9
5	250	400	50	0.95
6	50	500	100	0.95
7	200	400	100	0.95
8	100	150	200	0.9
9	100	150	100	0.95
10	50	400	50	0.9
11	200	750	100	0.95

Fig. 6-2 The modified test system for initial implementation of the islanding detection relay.

The modified test system is shown in Fig. 6-2. The modified test system had two DGs. A wind turbine driven, 1.5 MVA induction generator (DG1) was connected to Bus-7 with 0.5 MVars of capacitive compensation and a steam turbine driven1 MW synchronous generator (DG2) was connected to Bus-9. All loads in the network were simulated as constant RL loads. The system had two switches S1, S2 (which were kept normally open) making it possible to change the network configuration from radial to ring opera-

tion. Voltage and current measurements for the islanding detection relay were made at the terminals of DG1 (induction generator) and DG2 (synchronous generator).

6.4 Classification Methods

Pattern recognition involves different mathematical approaches to classify data (patterns) based either on a priori knowledge or on statistical information extracted from the patterns. There are five main components associated with a classification problem: (i) *Class* (*categorical outcome*, or *dependent variable*) - the characteristic associated with a given input, which is expected to predict; (ii) *Features* (*predictors* or *independent variables*) - the input variables, which are potentially related to the *class*. In general, there can be many possible predictor variables; (iii) *Learning (training) dataset* - a dataset, which includes values of both the *Class* and the corresponding *Features*; (iv) *Test dataset* – a dataset similar to learning data that is used to optimize/ test the accuracy of the trained classifier; (v) *Misclassification cost* - the inherent cost associated with misclassifying a future data.

In this study, it was attempted to distinguish transients generated due to system islanding from other transients generating disturbances like faults, load tripping, DG tripping, etc. Therefore, three classification techniques: (i) Decision Trees, (ii) Probabilistic Neural Networks, and (iii) Support Vector Machines were investigated to apply in islanding detection, and the following sections give a brief introduction of the methods.

6.4.1 Decision Tree Classifier and CART Algorithm

Decision Tree (DT) is a logical model constructed based on the training data, and represented as a binary tree. The DT starts with the "*Root*", which contains whole training dataset. Each "*Internal Node*" tests an attribute and each "*Arc*" corresponds to an attribute value. "*Terminal Node*" represents the predicted class [81]-[83]. Fig. 6-3 shows a sample structure of a DT of a two class problem.

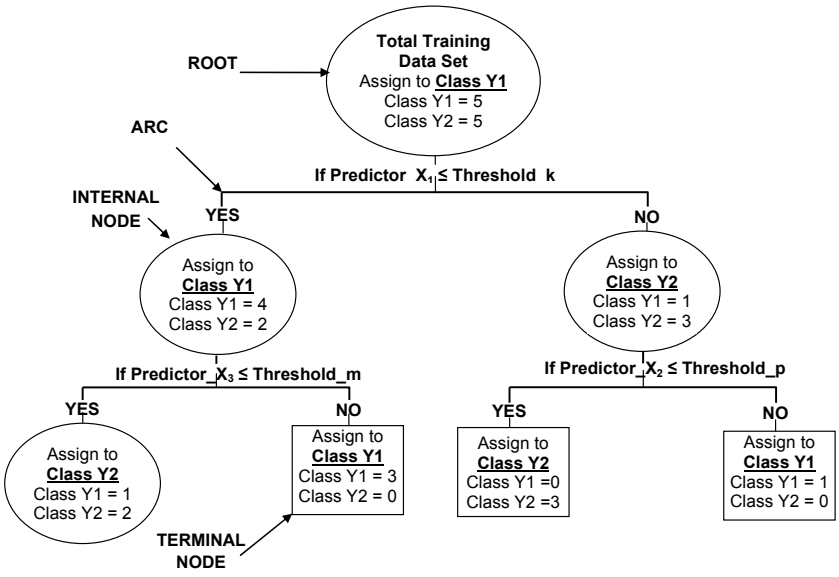

Fig. 6-3 Example DT Structure.

CART (Classification And Regression Trees) [81]-[84] is a technique that produces either classification or regression trees, depending on whether the dependent variable is categorical or numeric, respectively. CART algorithm generates decision trees based on a splitting rule. The basic idea of the splitting rule is to choose a split among all the possible splits at each node so that the resulting child nodes are the "purest". The splitting rule is processed in 3 steps:

1. Find the best split of each predictor variable
2. Find the best split of node
3. Assign the class

A brief explanation of the above steps is given in *Appendix–B* through an example case created by the author. A detailed explanation of CART algorithm can be found in [81]-[84]. The CART ® Pro V6 commercial software [82] was used to develop the decision tree classifier. The "Gini rule," which works well with the noisy data was selected as the splitting rule. The concept behind the Gini rule is to search the learning dataset for the largest class and to isolate it from the rest of the data. The mathematical representation of the Gini rule is also given in *Appendix B*. Besides the classification tree with *surrogates*, CART provides a ranking of input features based on each variable's contribution to the overall tree. It is determined by looking at every node in which a variable appears as a primary splitter or as a *surrogate splitter* and totaling the accuracies throughout the tree. Variable importance is presented by scaling the values relative to the *best performing variable*, which is the variable that minimizes the Gini impurity the most at every node it is considered as a splitter.

6.4.2 Probabilistic Neural Network Classification

Probabilistic neural network (PNN) is a neural network that is popularly used in classification applications. The PNN is primarily developed based on Bayesian classifier technique, which is commonly used in many classical pattern-recognition applications [85]. The theory on Bayesian classifier and PNN is well explained in [85].

Due to the fast training capability of the PNNs, they have been widely used in power system related applications [86]. The structure of a PNN is shown in Fig. 6-4 [85], [87]. The PNN case shown in Fig. 6-4 corresponds to a classification problem, which has three input features, four data in the learning dataset and two classes. The following explains the functions carried out at each layer shown in the figure.

- Input layer: This represents the input features of the test data. There is one neuron for each predictor variable. Each input neuron distributes the same input value to all of the pattern units.
- Pattern layer: The class-dependent probability density functions for all classification categories are calculated in this layer. There is one neuron for each case in training data and it stores both features and the target class. When presented with a vector of input values from the input layer, the pattern neuron computes the Euclidean distance of the test case from the neuron's center point and then applies the kernel function to this distance using the sigma, σ (or sometimes defined as spread, s) values, which is the smoothing factor. The Gaussian Radial Basis Function was selected as the kernel function in this study.
- Summation layer: There is one neuron for each category, and inputs to a summation neuron are the outputs of the pattern neurons that belong to the same category. Each neuron calculates the probability of an input pattern belonging to neuron's category by summing the inputs.
- Output layer: The probabilities for each target category are compared at this layer and the largest probability is used to predict target category.

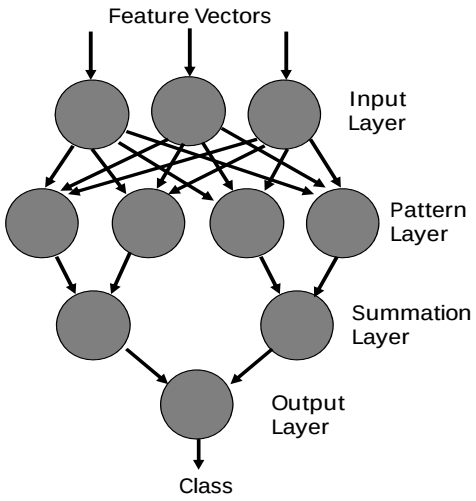

Fig. 6-4 PNN structure.

6.4.3 Support Vector Machine Classification

The Support Vector Machine (SVM) is a classification approach widely used in power system related applications. The SVM performs the classification by mapping the input vectors into a high dimensional space through some mapping function $\phi(x)$. In the higher dimensional space an optimal hyper plane is constructed to significantly increase the separation between the classes. Linear, polynomial, radial, or sigmoid activation functions can be used as the kernel function for mapping and the radial basis function was used in this study. Fig. 6-5 illustrates the concept SVM and Fig. 6-6 illustrates the concept of feature mapping in SVM.

SVM implements a special training algorithm that maximizes the separating margin between the classes, given by a set of *n* data pairs: input vector and class (x_i, d_i), where i = 1…..n. The minimization of objective function (6-1) subjected to (6-2) gives the solution for SVM [88]-[89].

$$L(W,\xi) = \frac{1}{2}W^T W + C\sum_{i=1}^{n}\xi_i, \quad \xi_i > 0 \tag{6-1}$$

$$d_i(W^T\phi(x_i) + b) \geq 1 - \xi_i \tag{6-2}$$

where, W is the weight and b is the bias and C is the penalty for the error term ξ. Theory on SVM can be found in [88]-[89].

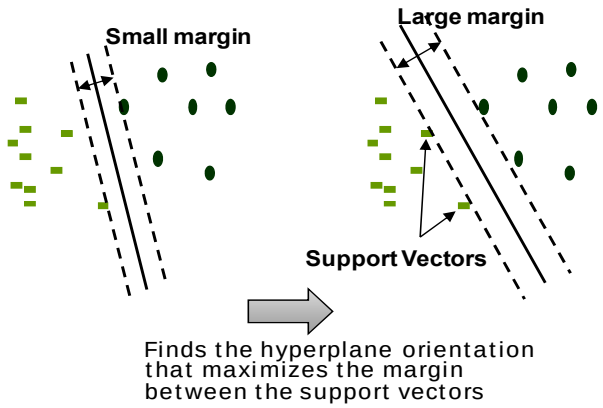

Fig. 6-5 Concept of SVM.

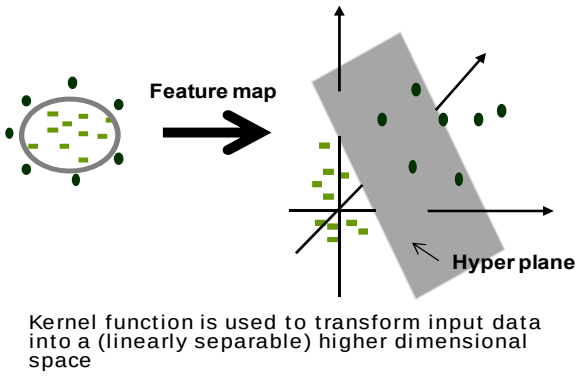

Fig. 6-6 The concept of feature mapping in SVM.

6.5 Features Used for Classification

The proposed islanding detection method was based on the hypothesis that the transients generated during the islanding event retain unique signatures that could be used to distinguish them from the transients initiated due to other disturbances. Therefore, it was important to identify the ease of classifying different transient events to meet the demanding response time for the islanding detection.

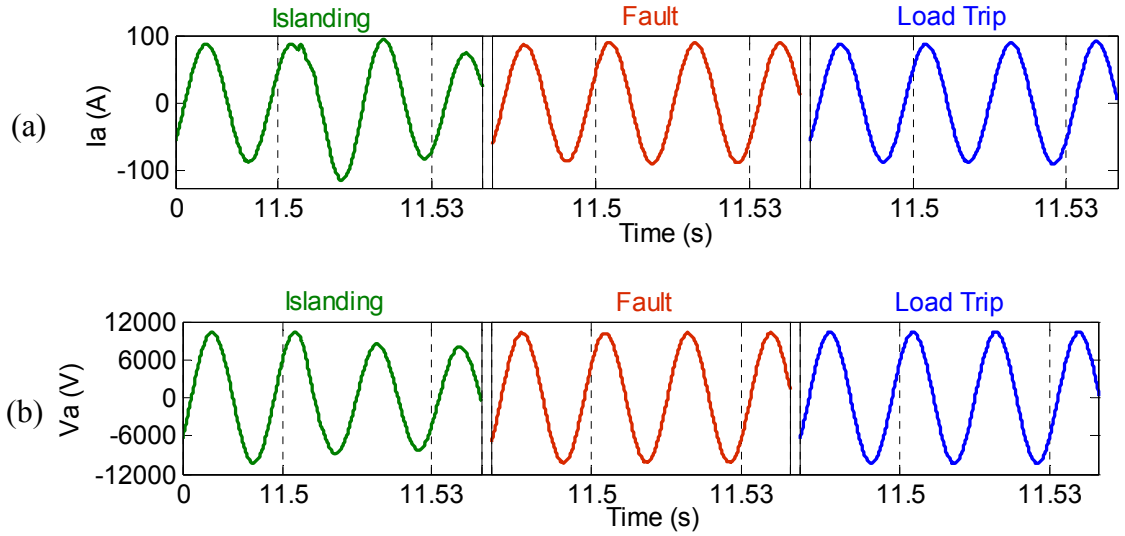

Fig. 6-7 Terminal response of phase-a, at DG1for an islanding, fault and a load trip (a) Current (b) voltage.

The current and voltage measured in phase-*a*, at DG1 (induction generator) terminals for (i) an islanding, (ii) a line-to-ground high impedance (100 Ω) fault on phase-b at Bus-2 and (iii) a load trip (585 kW + 283 kVar) events are shown in Fig. 6-7. The disturbance was applied at 11.5 s. When a significantly small time window (eg. 0.01 s) was considered, the event specific characteristics embedded in the transient waveforms were not directly distinguishable. Therefore, they needed to be pre-processed to extract a feature set that assist a fast responding classification task.

Wavelet transform was considered as an effective tool for processing transient signals, which are non-stationary in nature. Using the discrete wavelet transform (DWT), it is possible to decompose a signal into several signals in different frequency bands, which are known as wavelet coefficients. Due to the wavelet transform's nature of adapting the time width of the mother wavelet to its frequency, it is better suited to analyze transients compared to other frequency domain techniques such as windowed Fourier transform (WFT) [90]-[95]. Moreover, DWT allows extracting a range of frequencies through a single coefficient; the computational cost of obtaining the same set of information through WFT would be much higher. A good comparison of WFT and DWT can be found in [93].

DWT of a sampled signal *f(k)* is mathematically defined as:

$$DWT_{\psi} f(m,n) = \sum_{k} f(k)\psi^{*}_{m,n}(k) \tag{6-3}$$

where, $\Psi_{m,n}$ is the discretized mother wavelet given by:

$$\psi_{m,n}(k) = \frac{1}{\sqrt{a_0^m}}\psi\left(\frac{k - nb_0 a_0^m}{a_0^m}\right) \tag{6-4}$$

a_o (>1) and b_o (>0) are fixed real values, and *m* and *n* are positive integers. The DWT analyzes a signal by decomposing the signal into a coarse approximation and detail information. The coarse approximation is decomposed again to obtain the details of the next level, and so on. At each "*level"* of this successive decomposition, the parameter *m* in (6-4) is incremented to increase the frequency resolution. A good review of wavelets can be found in [92]-[94].

6.6 Feature Extraction

As discussed in the section 6-5, the DWT was used to extract the features for the classifiers. The DWT was performed online in the PSCAD simulation program using the DWT component developed in [96].

The DWT was performed on the sampled waveforms with the Daubechie's 4 (Db4) mother wavelet. The successful application of Db4 for characterizing power system transients is reported in many studies [94]-[96]. Comparison of the islanding detection performance with several mother wavelets types during the preliminary investigations confirmed the suitability of Db4 mother wavelet. During the initial investigations three sampling frequencies, 20 kHz, 10 kHz and 5 kHz, were considered.

Table 6-1 Frequency bands filtered out along with the size of mother wavelet at each level of DWT [96]

Level, **L**	**20 kHz**		**10 kHz**		**5 kHz**	
	Size of wavelet (s)	Frequency band (Hz)	Size of wavelet (s)	Frequency band (Hz)	Size of wavelet (s)	Frequency band (Hz)
1	0.0007	5000 < f < 10000	0.0014	2500 < f < 5000	0.0028	1250 < f < 2500
2	0.0021	2500 < f < 5000	0.0042	1250 < f < 2500	0.0084	625 < f < 1250
3	0.0049	1250 < f < 2500	0.0098	625 < f < 1250	0.0196	312.5 < f < 625
4	0.0101	625 < f < 1250	0.0202	312.5 < f < 625	0.0404	156.25< f < 312.5
5	0.0205	312.5 < f < 625	0.0410	156.25< f < 312.5	0.0820	78.125<f<156.25
6	0.0413	156.25< f < 312.5	0.0826	78.125<f<156.25	0.1652	39.0625<f<78.125

The frequency bands filtered out by DWT at each level was in accordance with the Mallat algorithm and Nyquist's rule. Table 6-1 presents the frequency bands filtered out along with the size of mother wavelet at each level of DWT output for the three sampling frequencies considered. According to [97], a_0 and b_0 of (6-4) was set to 2 and 1 respectively, in applying Mallat algorithm. This results in a geometric scaling of 1, ½, ¼,... and

translation by 0, n, $2n$,.... which decompose the input signal into sub bands with a bandwidth that increases exponentially with frequency. This scaling gives the DWT a logarithmic frequency coverage in contrast to the uniform frequency coverage of Fourier transformation.

The detail DWT coefficients using 10 kHZ sampling frequency for (i) the islanding, (ii) the line-to-ground high impedance (100 Ω) fault on phase-b at Bus-2 and (iii) the load trip (585 kW + 283 kVar) events were found. The detail DWT coefficients of the current and voltage measured in phase-*a*, at DG1 terminals are shown in Fig. 6-8 and Fig. 6-9 respectively. The disturbance was applied at 11.5 s and DWT coefficients are shown on an expanded scale that covers a time window of 0.03 s extending from 11.5 s to 11.53 s.

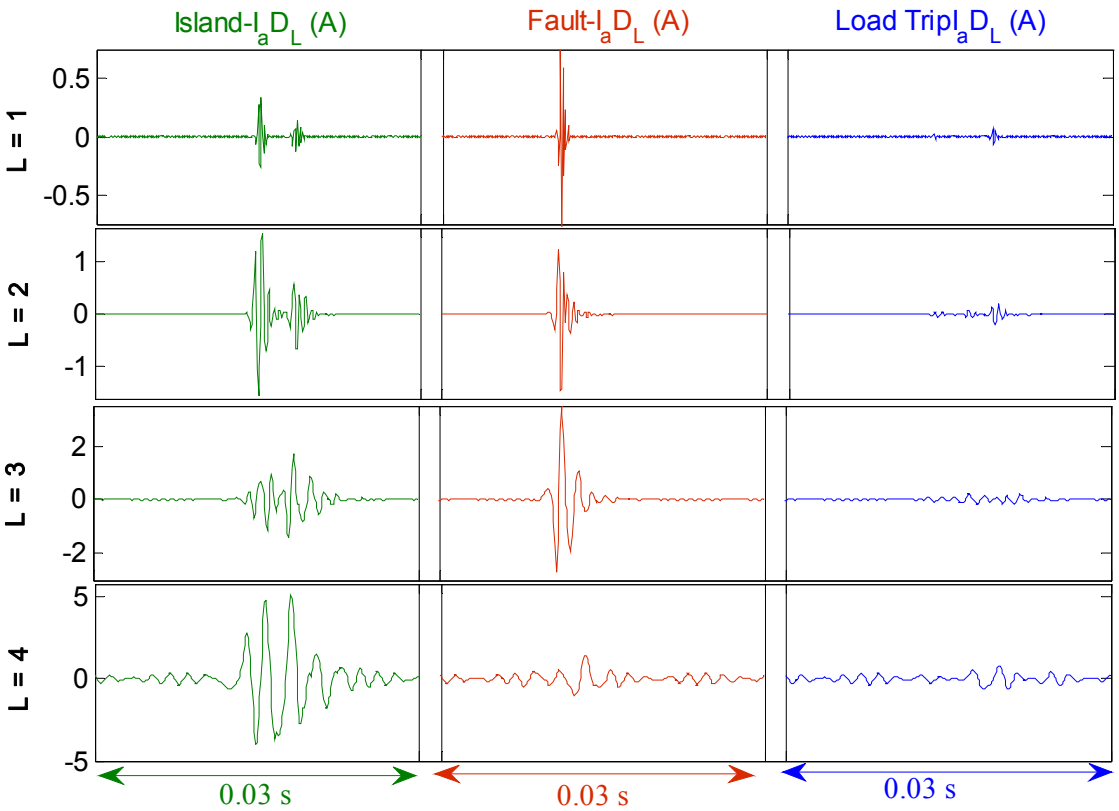

Fig. 6-8 DWT detail wavelet components of current signals.

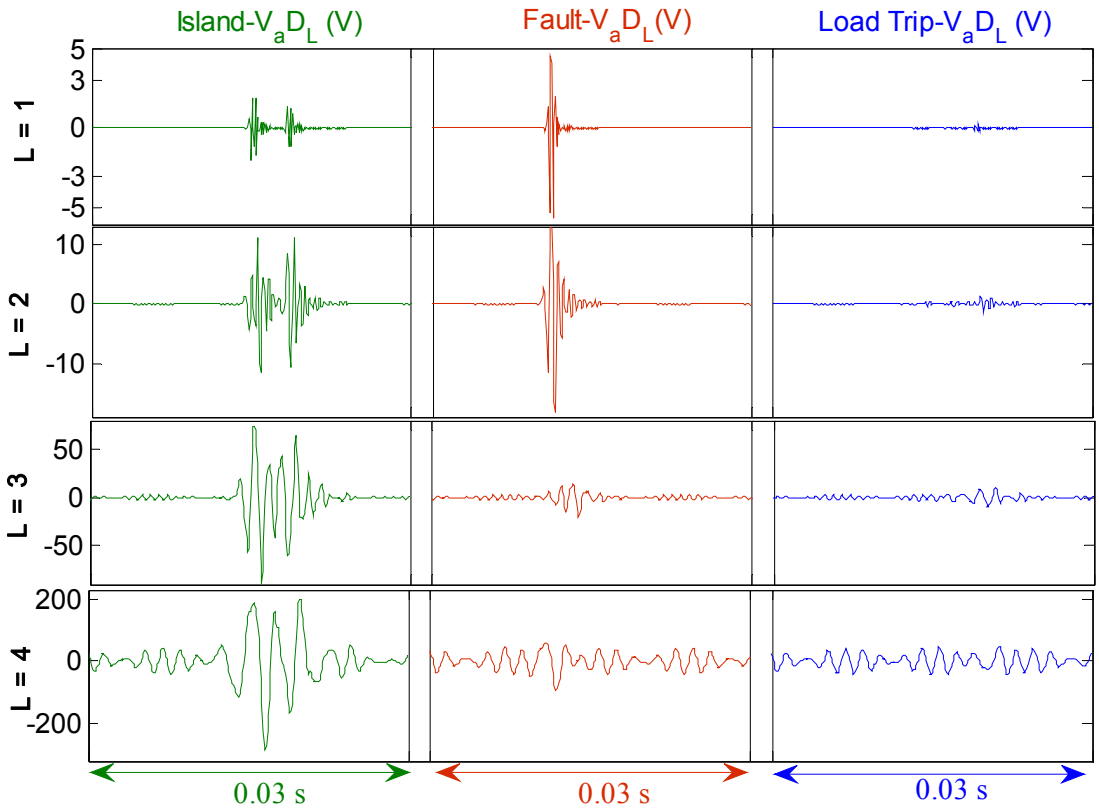

Fig. 6-9 DWT detail wavelet components of voltage signals.

Although original signals did not present distinguishable differences (Fig. 6-7), DWT coefficients depicted distinct identities among different events. In addition to the obvious variations in the range of amplitudes, there were other noticeable differences between the islanding and non-islanding events. Furthermore, it was clear that different non-islanding events themselves hold identities. Thus, an approach such as a simple threshold could be used to distinguish islanding and non-islanding events. Consequently, a more sophisticated method, involving pattern recognition was required.

Direct use of wavelet coefficients, which are essentially waveforms, as inputs to a classifier (in this case to a DT) is impractical. Thus, energies associated with the wavelet coefficients in a time window that encompasses the transient were used as features for the

classifier. Wavelet energy was obtained by integrating the square of the wavelet coefficient over a time window of 0.01 s. The analysis used a moving window, thus preserving the temporal information. This time window length was selected after preliminary investigations as a compromise between the accuracy and response time.

At each decomposition level, the energies of the three phases were added to form a combined 'three-phase energy' value in the particular frequency band. This feature extraction method using the DWT with 10 kHz sampling frequency is illustrated in Fig. 6-10. Only the decomposition of Phase-a current up to four levels is shown in detail to reduce the complexity of the figure. The calculated 'three-phase energy' values of the currents and voltages create a 12 dimensional feature space (6 levels of currents + 6 levels of voltages) for each generator, if output of six levels from DWT is used.

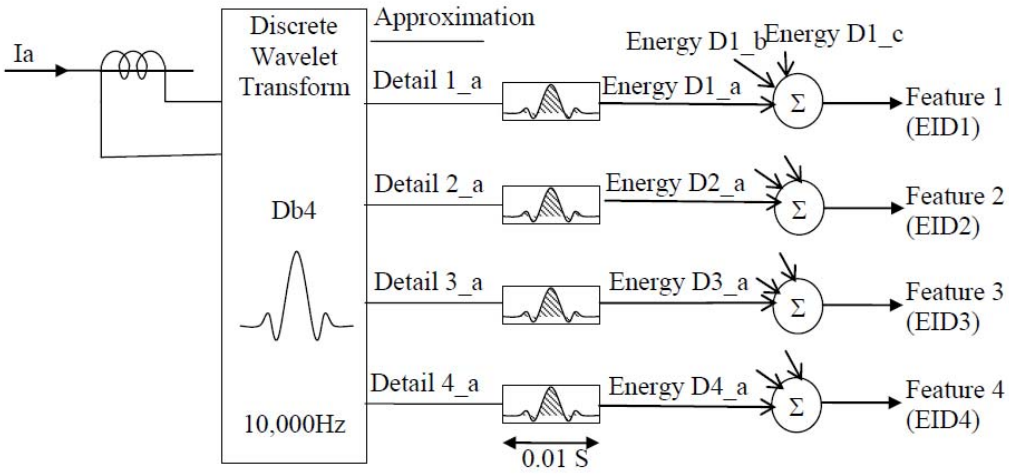

Fig. 6-10 Feature extraction of phase-a current waveform at 10 kHz sampling frequency.

6.7 Simulation Results and Analysis

6.7.1 Selection of the Classifier

As the first step, it was attempted to find the best classifier for the proposing transient based islanding detection. Only the features extracted from phase currents measured at the DG terminal were used in this step. Thus, the feature space was six dimensional. The sampling frequency of the DWT was set at 20 kHz in this step.

Two classes namely: non-islanding (C1) and islanding (C2) were considered. The simulated non-islanding cases included normal operation, temporary faults (3 phase-to-ground, 3 phase, line-to-line, line-to-ground) on the distribution network, switching of loads and switching of DGs. Opening of the breaker B1, operation of the feeder breakers B2 and B3 after a fault on Bus 2, and operation of breakers B3, B4 and B5 after fault on Bus 3 were included in the simulated islanding cases. The data were collected at different loading conditions (changing load impedances) and different system configurations (opening and closing switch S1).

A total of 154 islanding and 121 non-islanding cases were simulated. Out of this simulation database, 116 islanding cases and 89 non-islanding cases were used to train the classifiers. The remaining cases were used as testing data (i.e. nearly 75% of the total data set was used as training data and the remaining 25% was used as testing data).

Three classifiers based on the techniques explained in Section 6.4 were trained using the simulated data. To overcome misleading error rates that would result from the holdout method (having only one set of training and testing data), K-fold cross-validation is done.

In K-fold cross-validation, the original dataset is partitioned into K subsets. Of the K subsets, a single subset is retained as the validation data for testing the model, and the remaining (K − 1) subsets are used as training data. The cross-validation process is then repeated K times with each of the K subsets used exactly once as the validation data. The advantage of this method is that all observations are used for both training and validation, and each observation is used for validation exactly once [98]. A 4-fold cross-validation was carried out in this research [99], and only the results of the data fold that gave the best accuracies among the 4-folds are shown.

a. Decision Tree Based Classifier

Decision tree based classification was carried out using the CART 6 software. Although, CART itself provides K-fold cross validation, a 4-fold cross validation was carried out by inspection in order to maintain uniform procedure with the other two techniques. Two different approaches were tested: (i) Development of two separate classifiers for induction generator (DG1) and synchronous generator (DG2) by training the classifiers separately with the data measured at the respective generators and (ii) development of a single classifier using the waveforms measured at the both generators DG1 and DG2.

Table 6-2 summarizes the results of the decision tree classifier trained for each case. The "*overall classification accuracy*" means the accurate classification of both islanding and non-islanding as a percentage of the total data set. Table 6-2 shows that in training, overall classification accuracy was above 96%, whether the classifier was trained separately for each generator or whether a common classifier was trained for both generators. The classifier trained for induction generator (DG1) gave 93.6% accuracy in identifying

islanding events with an overall accuracy of 95.7% when the classifier was tested. Islanding identification accuracy of 93.5% with an overall accuracy of 92.7% was achieved when the classifier trained for the synchronous generator (DG2) was tested. In testing the common classifier trained for both DGs, 88.41% overall accuracy was achieved for induction generator and it was 97.1% for the synchronous generator.

Considering the different types of testing results in Table 6-2, in average, the overall classification accuracy achievable from the decision tree classification method was around 94%.

Table 6-2 Decision tree classification results (C1 – Non-Islanding, C2 – Islanding)

Training Topology	**Classification Accuracy , %**						
	Training	**DG1 Testing**			**DG2 Testing**		
	Overall	**Overall**	**C1**	**C2**	**Overall**	**C1**	**C2**
Trained for DG1 only	96.60	95.7	97.40	93.60	N/A*		
Trained for DG2 only	96.60	N/A*			92.7	92.10	93.50
Trained for both DG1and DG2	96.84	88.41	89.47	87.10	97.10	97.37	96.77

*N/A- Not Applicable

b. Probabilistic Neural Network (PNN)

Four-fold cross validation study was carried out with a PNN based classifier developed in MATLAB 8. The optimum achievable accuracy in each topology was searched by changing the value of "spread" and only the best cases for each training topology is presented in Table 6-3.

Table 6-3 PNN classification results (C1 – Non-Islanding, C2 – Islanding)

Training Topology	Classification Accuracy , %					
	DG1 Testing			DG2 Testing		
	Overall	C1	C2	Overall	C1	C2
Trained for DG1 only	94.0	92.1	96.7	N/A*		
Trained for DG2 only	N/A*			89.9	81.6	100
Trained for both DG1 and DG2	91.3	94.7	87.1	88.8	89.5	87.9

*N/A- Not Applicable

With the PNN classifier, better islanding identification accuracy (more than 96%) was achieved compared to the DT classifier when separate classifiers were trained for each generator. However, overall classification accuracy of the PNN classifier was observed to be lower compared to the DT classifier since PNN was poor in classifying the non-islanding cases correctly. For the common classifier trained with PNN, overall classification accuracy achieved in testing the induction generator was 91.3% and with synchronous generator it was 88.8%. In average, overall classification accuracy of PNN classifier was around 90%.

c. Support Vector Machines

Islanding detection classifiers based on Support Vector Machine (SVM) were developed in MATLAB 8 using the Library for Support Vector Machines (LIBSVM) developed by Chih-Chung Chang and Chih-Jen Lin [100]. Table 6-4 presents a summary of the results by SVM classifiers developed for training generators separately and for training both generators to achieve a common classifier.

The overall classification accuracy achieved in testing, when the classifier was trained for induction generator separately was 88.4% and it was 73.9% for the synchronous generator. The common classifier trained for both DGs, gave an overall classification accuracy of 73.9% in testing induction generator and 72.5% in testing synchronous generator. SVM classifier gave the lowest average overall classification accuracy around 78% compared to the DT and PNN classifiers.

Table 6-4 SVM classification results

Training Topology	**Overall Classification Accuracy , %**	
	DG1 Testing	**DG2 Testing**
Trained for DG1 only	88.4	N/A*
Trained for DG2 only	N/A*	73.9
Trained for both DG1 and DG2	73.9	72.5

d. Concluding Remarks on Classifier Selection

By comparing the results, it could be concluded that the best classification accuracy was achieved from the *decision tree classifier* when the energies of detailed DWT coefficients up to level six of current waveforms were used as input features. With the considered feature space, training each generator separately gave better accuracy than training a common classifier.

6.7.2 Effect of Sampling Frequency

The sampling frequency of 20 kHz was first selected with the plan of developing a fast islanding detection method. DWT by its nature adapts the time window of the mother

wavelet according to the frequency band. The number of samples required to represent the mother wavelet at each detail level in the DWT is discussed in [96]. Table 6-1, presented the frequency bands filtered out along with the size of mother wavelet at each level of DWT output for the three sampling frequencies considered based on [96]. It is clear from Table 6-1, that the size of the mother wavelet increases with the level of DWT and it depends on the sampling frequency used. On the other hand, the most dominant component that determines the response time of the proposing islanding detection relay is time window considered in creating the features. If a time window of 0.01 s is considered in the feature extraction, it captures the full mother wavelet up to four levels if 20 KHz sampling frequency is used. Only $1/4^{th}$ of the sixth level mother wavelet is captured in this case. With the use of 10 kHz sampling frequency, full mother wavelet is captured up to three levels. But, only ½ of the 4^{th} level and $1/8^{th}$ of the sixth level is captured when 10 kHz sampling frequency is used. The information is deteriorated when 5 kHz sampling frequency used having only two levels with full mother wavelet being captured in a 0.01s time window. Only $1/16^{th}$ of the mother wavelet is captured in the sixth level in this case.

It was important to reduce the feature space as much as possible to reduce the computational and hardware cost while maintaining the classification accuracy and the speed of detection. The above discussion indicates that with the use of higher sampling frequency it is possible to use a small time window in feature extraction, but still capturing the full information down to higher levels of DWT decomposition.

With the use of 20 kHz sampling frequency, it was observed that the DT classification method gives the best average overall classification accuracy compared to PNN and SVM classification methods, and it was still nearly 94%. Further, it used six levels in the

DWT of terminal current as features for classification. Therefore, this section presents the effect of sampling frequency on classification accuracy, with a view on the possibility to reduce the feature space. With the observed results from the previous section, only DT classifier was considered.

Table 6-5 DT classification results at different sampling frequencies for DG1 for six dimensional feature space (C1 – Non-Islanding, C2 – Islanding)

Sampling Frequency (kHz)	Classification Accuracy , %				Variables in the Order of Importance	Depth of the DT
	Training	Testing				
	Overall	Overall	C1	C2		
20	97.09	95.65	97.37	93.55	EID1, EID2, EID3, EID5, EID4, EID6	8
10	99.03	98.55	97.37	100	EID3, EID2, EID1, EID4, EID5, EID6	5
5	98.05	97.10	97.37	96.77	EID1, EID4, EID2, EID3, EID6, EID5	4

Table 6-6 DT classification results at different sampling frequencies for DG2 for six dimensional feature space (C1 – Non-Islanding, C2 – Islanding)

Sampling Frequency (kHz)	Classification Accuracy , %				Variables in the Order of Importance	Depth of the DT
	Training	Testing				
	Overall	Overall	C1	C2		
20	96.60	92.75	92.11	93.55	EID6, EID4, EID1, EID5, EID2, EID3	13
10	100	98.55	97.37	100	EID1, EID2, EID3, EID4, EID6, EID5	8
5	97.56	98.55	100	96.77	EID4, EID5, EID6, EID1, EID2, EID3	5

Though not the same events, similar events as that at 20 kHz sampling frequency were simulated at 10 kHz and 5 kHz sampling frequencies of DWT. Thus, the number of islanding and non-islanding events used as learning and testing data sets for classification at both 10 kHz and 5 kHz were same as that at 20 kHz (for each sampling frequency, a total of 154 islanding and 121 non-islanding cases were simulated. Out of this simulation database at each sampling frequency, 116 islanding cases and 89 non-islanding cases

were used to train the classifiers. The remaining cases at each sampling frequency were used as testing data). The DT classifiers were trained for each generator using the six dimensional feature space derived from terminal phase current signals.

Tables 6-5 and 6-6 show the DT classification results at different sampling frequencies for the classifiers trained separately for islanding detection at DG1 and DG2 respectively. Tables present the classification accuracy, variable importance in the classification task where, EID*L* denote the energy values of the level *L* wavelet coefficient of the DG terminal current signal, and the depth of the DT classifier, which gives the total number of node levels from root to the last terminal node of the classifier.

For both DG1 and DG2 using 10 kHz sampling frequency produced the best overall classification accuracy being 100% accurate in classifying tested islanded cases. Although comparatively similar overall classification accuracies were observed at 5 kHz sampling frequency, it was more accurate in classifying non-islanding than islanding cases. The depth of the Decision Tree indicates how complicated the classification problem was, and for this classification problem, the DTs were simple and easy to implement at all sampling frequencies of DWT.

The variable importance facilitates to select the features for the classifiers. With the use of 10 kHz sampling frequency, for both classifiers at DG1 and DG2, energy contents of first four levels of DWT of current waveforms were the most important in correct classification. But, at the other two sampling frequencies, levels 5 and 6 of DWT were important for classification at DG2. This was further examined by creating classifiers using only the energy contents of the first four levels of DWT of current waveforms at each generator separately. Results for the classifiers trained for DG1 and DG2 are shown in

Tables 6-7 and 6-8 respectively. The results revealed that at 10 kHz sampling frequency, the islanding detection accuracy was still higher compared to other two sampling frequencies when only 4-dimensional feature space was used. In testing the classifiers at DG2, at 20 kHz and 5 kHz sampling frequencies, the performance of islanding detection had further deteriorated.

Table 6-7 DT classification results at different sampling frequencies for DG1 for four dimensional feature space (C1 – Non-Islanding, C2 – Islanding)

Sampling Frequency (kHz)	Classification Accuracy, %				Variable Importance in Order	Depth of the DT
	Training	Testing				
	Overall	Overall	C1	C2		
20	96.60	94.20	94.74	93.55	EID1, EID2, EID3, EID4	11
10	98.54	97.10	97.37	96.77	EID3, EID1, EID2, EID4	5
5	98.05	97.10	97.37	96.77	EID1, EID4, EID2, EID3	4

Table 6-8 DT classification results at different sampling frequencies for DG2 for four dimensional feature space (C1 – Non-Islanding, C2 – Islanding)

Sampling Frequency (kHz)	Classification Accuracy , %				Variable Importance in Order	Depth of the DT
	Training	Testing				
	Overall	Overall	C1	C2		
20	90.29	92.75	94.74	90.32	EID2, EID1, EID3, EID4	10
10	94.66	97.1	94.74	100	EID2, EID3, EID1, EID4	3
5	95.12	97.1	100	93.55	EID1, EID4, EID2, EID3	4

Therefore, in order to develop a fast and reliable islanding detection method, 10 kHz sampling frequency appeared to be the best choice for the DWT. However, further research was required to improve the classification accuracy to create a relay with both high dependability and selectivity.

6.7.3 The Transient Based Islanding Detection Methodology

The basic concept of the transient based islanding detection scheme was shown in Fig. 6-1. From the initial investigations discussed in 6.7.1, Decision Tree (DT) classifier was selected as the best performing classifier among DT, probabilistic neural networks and support vector machines for islanding transient classification. Furthermore, with the investigations reported in the Section 6.7.2, 10 kHz sampling frequency was selected for the DWT considering the accuracy of classification, speed of detection, and hardware cost/capability required for real time implementation.

a. Initial Classifier and Feature Selection

With the intention to improve the classification accuracy, both phase currents and voltages measured at the generators were used and the same approach as explained in section 6.6, referring to Fig. 6-7 was used in feature extraction. Thus, a 12-dimensional feature space (6 levels of currents + 6 levels of voltages) was used in the first step.

Two classes of events, namely "non-islanding" and "islanding" were considered. The simulated non-islanding cases included: (i) Normal operation; (ii) Temporary faults including 3-phase-to-ground, 3-phase, line-to-line, and line-to-ground; (iii) Switching of loads; and (iv) Switching of DGs. The simulated islanding cases included: (i) Opening of the breaker B1; (ii) Opening of the feeder breakers B2 & B3, after fault on Bus-2; and (iii) Opening of breakers B3, B4 and B5 after fault on Bus-3. The data were collected at different loading conditions and under different system configurations obtained by opening and closing switch S1.

A total of 348 islanding and 539 non-islanding cases were simulated and the three-phase currents and voltages measured at the terminals of the both DGs were recorded. Nearly 85% of the data, which included 279 islanding cases and 479 non-islanding cases, were used for training. The remaining cases were used as testing data. Testing data were extracted randomly from each category of events described above to ensure testing against all types of transient events.

Initially, a DT was trained for DG1 using all 12 features. When a DT is trained, the CART software produces an output such as Table 6-9, which indicates the importance of each input feature to the classification process as a percentage of the values relative to the best performing variable. In Table 6-9, EVD*L* and EID*L* denote the energy values of the level *L* wavelet coefficient of the terminal voltages and the currents respectively. Examination of Table 6-9 showed that relevancy of some of the features was very low and they could be omitted without significantly reducing the accuracy.

Table 6-9 The importance of features in training a classifier for DG1 using a 12-dimensional feature space

Feature	Importance (%)	Feature	Importance (%)
EVD1	100.00	EID4	39.36
EVD2	98.31	EVD4	38.11
EID1	96.28	EID5	0
EID3	95.07	EVD5	0
EVD3	55.81	EVD6	0
EID2	55.35	EID6	0

After analyzing the tables of variable importance for both DG1 and DG2, it was found that using only up to four decomposition levels was sufficient to train a reliable classifier. Thus, an eight dimensional feature space was used for the further investiga-

tions. This allowed the use of DWT with 4 levels of decomposition effectively reducing the calculation time as discussed under the Section 6.7.2.

b. Development of the Classifier

Two different approaches were tested: (i) Development of two separate classifiers for DG1 (Induction Generator) and DG2 (Synchronous Generator) by training the classifiers separately with the data measured at the respective generators and (ii) Development of a single classifier using the waveforms measured at both generators DG1 and DG2.

- **Training a separate classifier for each generator**

Table 6-10 summarizes the results of the classifier trained for induction generator (DG1) to identify islanding. The overall classification accuracy (accurate classification of both islanding and non-islanding as a percentage of the total data set) achieved in testing the classifier was 99.22%. The depth of the Decision Tree (number of division levels from the Root to the farthest terminal node) was 8.

Table 6-10 Decision tree classifier trained for DG1

	Training		Testing	
	Total Cases	Correctly Classified Cases	Total Cases	Correctly Classified Cases
Non-islanding	479	477 (99.58%)	60	59 (98.33%)
Islanding	279	278 (99.64%)	69	69 (100%)
Total	758	755 (99.60%)	129	128 (99.22%)

The results obtained with the classifier trained for the synchronous generator (DG2) are summarized in Table 6-11. An overall classification accuracy of 100% was achieved in testing the classifier and the depth of the tree in this case was only 5.

Table 6-11 Decision tree classifier trained for DG2

	Training		Testing	
	Total Cases	Correctly Classified Cases	Total Cases	Correctly Classified Cases
Non-islanding	479	473 (98.75%)	60	60 (100%)
Islanding	279	277 (99.28%)	69	69 (100%)
Total	758	750 (98.94%)	129	129 (100%)

- **Training a common classifier for both generators**

The idea behind training a common classifier was that if this was successful, identical classifiers could be used at all generators. The results of this experiment are given in Table 6-12. The classifier trained for both generators gave 98.28% overall accuracy on the training dataset. With the testing data for the induction generator (DG1), it achieved an overall accuracy of 99.22%, while achieving 100% accuracy in identifying islanding events. With testing data for the synchronous generator (DG2), the classifier achieved 100% overall accuracy.

Table 6-12 Decision tree classifier trained for both DG1 and DG2

	Training		Testing			
			DG1		DG2	
	Total Cases	Correctly Classified Cases	Total Cases	Correctly Classified Cases	Total Cases	Correctly Classified Cases
Non-islanding	958	935 (97.6%)	60	59 (98.33%)	60	60 (100%)
Islanding	558	555 (99.46%)	69	69 (100%)	69	69 (100%)
Total	1,516	1,490 (98.28%)	129	128 (99.22%)	129	129 (100%)

Thus, the classifier gave an overall accuracy of 99.61% when both generators were considered. Based on the simulation experiment that included 258 observations (considering both generators), it could be stated with 95% confidence [101] that relay overall ac-

curacy is greater than 98%. The details of the hypothesis testing are given in *Appendix C*. It should be noted that the data corresponding to the normal operation (no transients) were excluded when calculating the accuracy values reported in Tables 6-10, 6-11 and 6-12. The trained classifiers were found to be always accurate under normal operation. Thus, the removal of normal operation cases resulted in more conservative (lower) estimates for the accuracy.

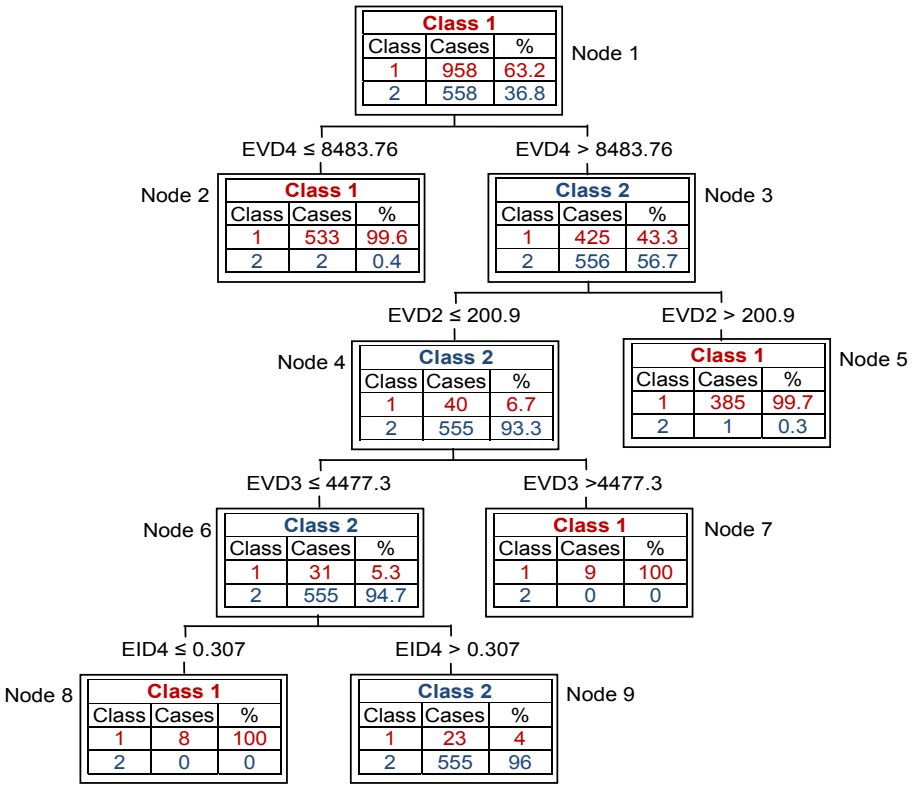

Fig. 6-11 The Decision Tree classifier for detecting power islands.

Fig. 6-11 shows the decision tree structure of the classifier trained for both generators. The depth of the tree was 5. This tree was built in accordance to the CART algorithm (explained in *Appendix B*) using the CART ® Pro V6 commercial software [83]. The root (Node 1) has the total training data set. The percentage values in each other

node indicates how well the each splitter performs in classifying the assigned class. For example, based on the first splitter, that is when EVD4 ≤ 8483.74, a total of 535 cases were classified as Class-1 (Non-islanding). Out of these, only 533 were actually belonging to Class-1; the other two belong to Class-2. With two misclassified cases it gave 99.6% classification accuracy at the particular splitter.

Features EVD1, EID1, EID2 and EID3 were not used in the final DT, but they can be used as surrogate variables, i.e. to replace a particular variable from the final classifier if needed (for example to improve the noise immunity). Since the calculation of EID4 using the Mallet tree algorithm requires calculation of EID1, EID2 and EID3 as intermediate signals, the feature extraction structure presented in Fig. 6-10 was retained.

The results presented above indicated that the common classifier was able to give the same accuracy as separate classifiers in identifying islanding, while keeping the depth of the tree smaller than the separate classifier trained for DG1. Thus, the common classifier was selected for further evaluation.

c. The Process of Islanding Detection

Figs. 6-12(a)-(e) illustrates, how the signals were processed through the proposed method in the DT relay at DG1 for an example islanding event (opening of breaker B3) that happened at t = 11.5 s.

The feature extraction and classification process, which involves extraction of DWT coefficients, calculation of energy content of wavelets, transient detection and the processing in the DT classifier, is associated with certain time delay.

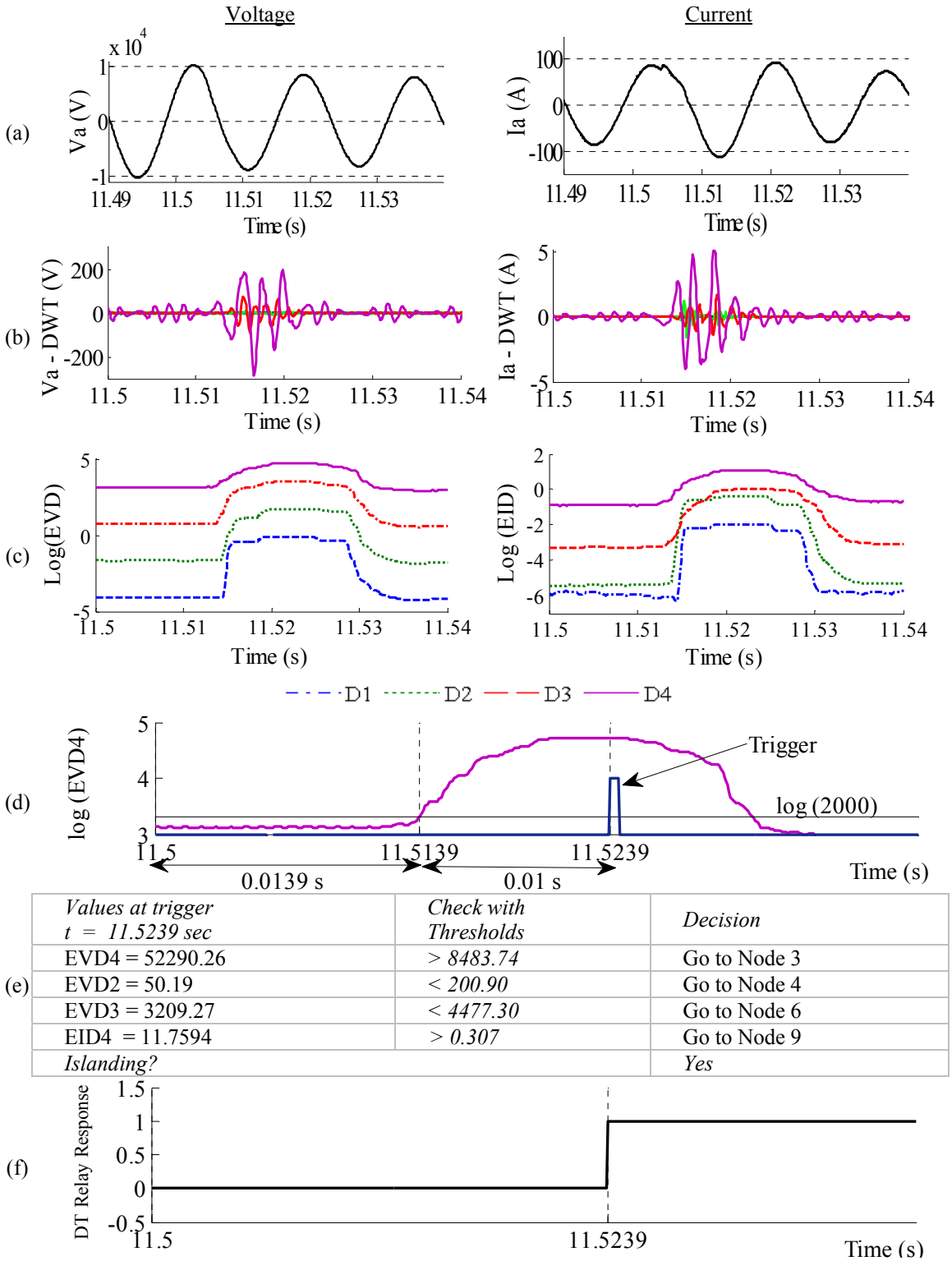

(e)

Values at trigger *t = 11.5239 sec*	*Check with Thresholds*	*Decision*
EVD4 = 52290.26	*> 8483.74*	Go to Node 3
EVD2 = 50.19	*< 200.90*	Go to Node 4
EVD3 = 3209.27	*< 4477.30*	Go to Node 6
EID4 = 11.7594	*> 0.307*	Go to Node 9
Islanding?		*Yes*

Fig. 6-12 The process in DT relay: (a) input signals, (b) DWT output, (c)Log("3-phase wavelet energy contents"), (d) transient signal detection (trigger), (e) DT classification process, (f) DT relay output.

Fig. 6-12 (a) reveals that the transient appears in the input voltage and current signals at the moment the disturbance happened (t =11.5 s). However, as can be seen from Fig. 6-12 (b), (c) and (d), the DWT and energy content calculation introduces a delay of about 0.0139 s for this particular islanding event.

The classifier was triggered by using a transient detector. Fig. 6-12 (d) illustrates how the transient was detected by using the energy content of the level four detail coefficient of DG terminal voltage (EVD4) in a sliding window of 0.0005 s. EVD4 was selected as the trigger initiator considering its quality of showing comparatively large variation in the event of a transient. If the value of EDV4 exceeded a pre-set threshold value (2000), the classification was carried out after a delay of 0.01 s. This delay was equal to the window length for calculating wavelet energy values that were fed to the classifier. The trigger threshold was set by studying the data set. According to Fig. 6-12 (d), the transient was detected at t = 11.5139 s, and a trigger was generated after a 0.01 s to activate the classifier. With already prepared inputs, the classifier operation was almost instantaneous and thus, the relay output was generated at t = 11.5239 s. The response time of the proposed relay for this particular islanding event was 0.0239 s (23.9 ms). Relay showed similar response, which was observed to be always less than 25 ms at every islanding event tested.

6.8 Concluding Remarks

A fast and reliable islanding detection method based on wavelet coefficients of transient signals was proposed. A trained Decision Tree classifier was able to successfully categorize the transient generating events as ‘islanding’ or ‘non-islanding’ using the energy as-

sociated with the wavelet coefficients. When tested with a large number of test cases, the proposed technique showed over 98% overall classification accuracy at 95% confidence level. The response time of the relay remained below two cycles for all test cases.

Chapter 7

Islanding Detection Performance

Chapter 6 described the design and implementation of an islanding detection method based on transient signals. This chapter presents the application of the proposed methodology to an extended test system with a DC source interconnected via a Voltage Source Converter (VSC). The proposed new islanding detection technique is a passive method, and in this chapter, its performance is compared with the existing passive islanding detection methods under different scenarios. Common passive anti-islanding protection methods currently in practice, their principles of operation and the typical settings were discussed in Chapter 2. The conventional passive islanding detection methods considered were: Over/Under voltage, Over/Under frequency, Voltage Vector Shift (VVS) and Rate of Change of Frequency (ROCOF). Furthermore, the effects of noise and the variations of the utility system impedance on the performance of the proposed method were studied.

7.1 Application to a Modified Test System

With the intention to evaluate the robustness of the proposed transient based islanding detection methodology under different test systems, it was applied to the microgrid test sys-

tem proposed in Chapter 3 (Fig. 3-1) with slight modifications like integrating induction motor and switched capacitors to facilitate a higher dimension of transient events. The upgraded test system is shown in Fig. 7-1. A detailed discussion on the developed basic microgrid test system is given in Chapter 3

The modified test system included one induction motor of 0.5 MW at Bus-4, which was set to start and operate in a constant power after set time duration. The rest of the loads were simulated as constant RL loads. Single pole operated switched capacitor bank was connected at the POI. To include the effect of the inrush current transients of transformer energizing, an open circuited transformer was connected at Bus-6 via a circuit breaker.

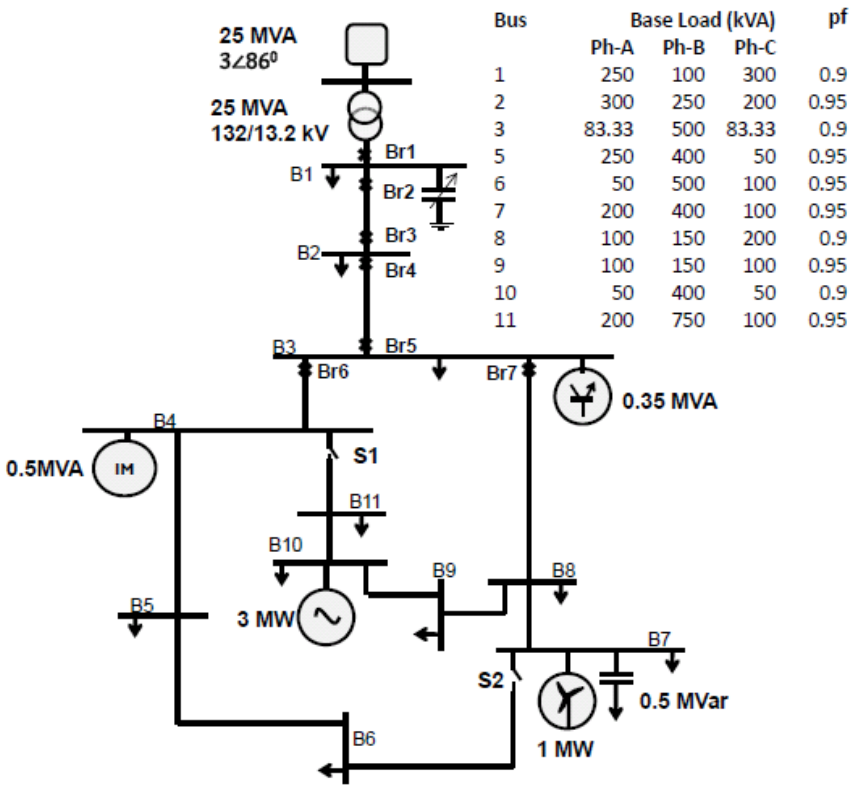

Bus	Base Load (kVA)			pf
	Ph-A	Ph-B	Ph-C	
1	250	100	300	0.9
2	300	250	200	0.95
3	83.33	500	83.33	0.9
5	250	400	50	0.95
6	50	500	100	0.95
7	200	400	100	0.95
8	100	150	200	0.9
9	100	150	100	0.95
10	50	400	50	0.9
11	200	750	100	0.95

Fig. 7-1 Block diagram of the proposed transient base islanding detection technique.

The test system used in this study (Fig. 7-1) was significantly different from the distribution test system used in Chapter 6 (Fig. 6-2). The new test system was (i) integrated with a VSC based source, (ii) the generator capacities and locations were changed, (iii) a large induction motor was included, (iv) the loads representation was changed from only RL loads to combination of RL loads and constant PQ load, and (v) a variable capacitor bank was included.

The DT classifier, which relied on training examples to build its classification rules, was required to re-train when applying to a completely new system or adding new generators to the same system. Specially, with the addition of a DC source connected through a VSC, harmonics were introduced into the system.

This is illustrated in Fig. 7-2 which shows the DWT coefficients for four levels (Level-1: 5000-2500Hz; Level-2: 2500-1250Hz; Level-3: 1250-625 Hz; Level-4: 625-312.5Hz) and 3-phase energy contents of the wavelet coefficients for a voltage transient observed during an islanding event. The differences in the above quantities for the system operation with and without the VSC based generator are clearly seen in Fig. 7-2.

Energy contents of the wavelets shown in Fig. 7-2(e) depicts how the “signature of the islanding event” in the transient signal had been changed with the addition of the VSC interconnected DC source, even though the system loading conditions were the same in both cases. The high frequency voltage ripple was introduced by the VSC control, due to the highly unbalanced nature of the test system.

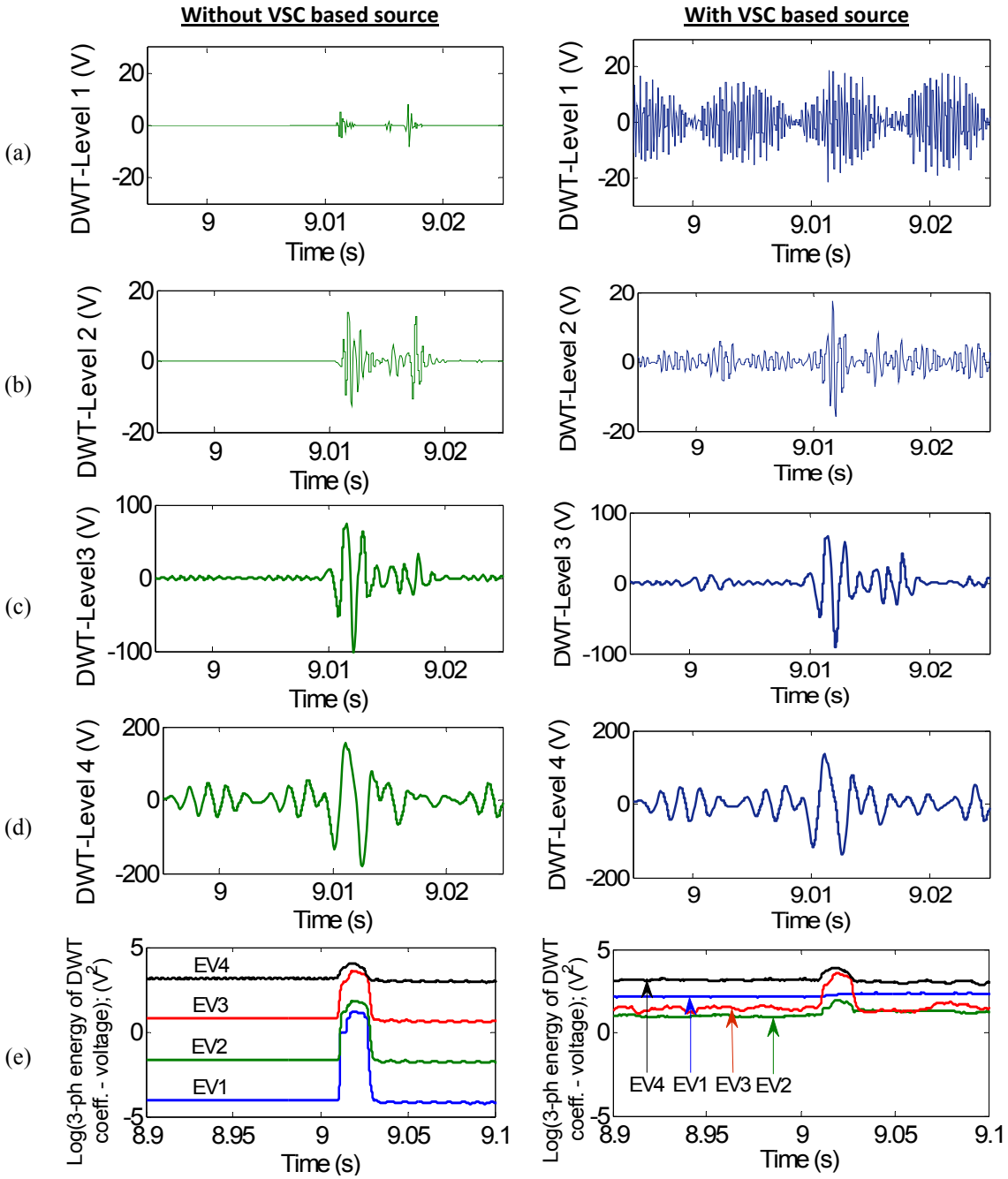

Fig. 7-2 Comparison of DWT coefficients of Phase-a terminal voltage at the synchronous generator for an islanding event happening in the system with and without the VSC based source in operation.

The DT classifier for the new system was designed using the same methodology as proposed in Chapter 6. The scope of the transient events was expanded to gain higher confidence on the reliability of the transient based islanding detection methodology. A simulation database was prepared considering a large number of "islanding events" and other transient generating events which were labeled as "non-islanding events".

The islanding cases included:

- Opening of the breaker *Br1*;
- Opening of the breakers *Br1*and *Br2*, after fault on Bus-1;
- Opening of the feeder breakers *Br3* and *Br4*, after fault on Bus-2; and
- Opening of breakers *Br5, Br6* and *Br7* after fault on Bus-3.

Non-islanding events included:

- Temporary faults initiation and clearing (ABCG, ABC, AB, AC, BC, ABG, ACG, BCG, AG, BG, CG faults with impedances ranging from 0.001Ω to 100Ω at buses1, 2, 3 and 10 occurring at different inception angles);
- Switching of loads (single and multiple);
- Balanced and unbalanced switching of capacitors (100 kVar/ph to 1000 kVar/ph);
- Switching of DGs;
- No-load transformer energizing and
- Induction motor starting. The wound rotor induction motor was started from zero speed with an applied mechanical torque (T_m) proportional to the square of the speed ($T_m = k\omega^2 + b$; where, ω = speed).

The data were collected at different loading conditions considering the load curves specified for the CIGRE Benchmark test system (the loads were changed in steps of 10% in the range of 50 - 120% of the base load, maintaining the power factor of R-L loads) [39]. Also, operation with single generator, two generators and all three generators were considered. Switches S1 and S2 were kept open. Lighting strike transients were not included as these transients are not captured by the relay, which is designed to sample the input waveforms at 10 kHz frequency. However, the secondary effects of lightning transients, such as faults due to insulation failure were captured under the fault transients considered in the dataset.

A total of 237 islanding and 922 non-islanding cases were simulated and the three-phase currents and voltages measured at the terminals of all three DGs were recorded. Based on the recommendation in Chapter 6, a single classifier was trained for all three generators using CART Pro. V6 software [83]. Since a single classifier was trained for all three generators, the voltage and current data observed at all three generators were combined to form a larger dataset containing 711 islanding data and 2766 non-islanding data.

7.1.1 Effect of the Size of Training Dataset

Having a large size of data set prompted to investigate on the effect of the size of the training data set on the classification accuracy and feature selection. In optimizing the DT classifier, 3-fold, 4-fold and 6-fold cross-validation procedures were conducted to select the best approach to avoid the errors that could happen due to relying on a particular data set. In creating the folds at each case, data were extracted randomly from each category of transient events described above to ensure testing against all types of transient events.

Tables 7-1, 7-2 and 7-3 present the classifier training and testing accuracies observed with 3-fold, 4-fold and 6-fold cross validations respectively. They present the results of the best performing fold in each case. Tables also present the variables used in training each classifier in the order of their importance. In training the classifier, all eight features (i.e. the energies in the first four levels of DWT coefficients of voltage and current) were used initially, and it was attempted to reduce the feature space maintaining the accuracy greater than or equal to that when using the eight dimensional feature space.

Results in Tables 7-1, 7-2 and 7-3 indicated that 6-fold cross validation gives the best accuracies in classifying both islanding and non-islanding events correctly. To represent this fact clearly, the aggregated accuracy considering both training and testing data (3477 events) at each cross validation case is illustrated in Fig. 7-3. It showed that any training attribute gives aggregated classification accuracy above 97%, while having 98.7% as the highest that was archived in 6-fold cross validation.

Table 7-1 Best performing Decision Tree classifier using 3-fold cross validation

	Training		Testing		Variables in Importance Order
	Total Cases	Correctly Classified Cases	Total Cases	Correctly Classified Cases	EVD3 EVD2 EID3 EVD4 EID2 EVD1 EID1 EID4
Non-islanding	1,841	1,813 (98.48%)	925	897 (96.97%)	
Islanding	475	472 (99.37%)	236	222 (94.07%)	
Total	2,316	2285 (98.66%)	1,161	1119 (96.38%)	

Table 7-2 Best performing Decision Tree classifier using 4-fold cross validation

	Training		Testing		Variables in Importance Order
	Total Cases	Correctly Classified Cases	Total Cases	Correctly Classified Cases	
Non-islanding	2,064	2036 (98.64%)	702	682 (97.15%)	EVD3 EVD2 EVD4 EID4 EVD1
Islanding	532	529 (99.44%)	179	175 (97.77%)	
Total	2,596	2565 (98.80%)	881	857 (97.28%)	

Table 7-3 Best performing Decision Tree classifier using 6-fold cross validation

	Training		Testing		Variables in Importance Order
	Total Cases	Correctly Classified Cases	Total Cases	Correctly Classified Cases	
Non-islanding	2,307	2276 (98.66%)	459	447 (97.39%)	EVD3 EVD2 EVD4 EID3 EID4 EID2
Islanding	594	593 (99.83%)	117	115 (98.29%)	
Total	2,901	2869 (98.90%)	576	562 (97.57%)	

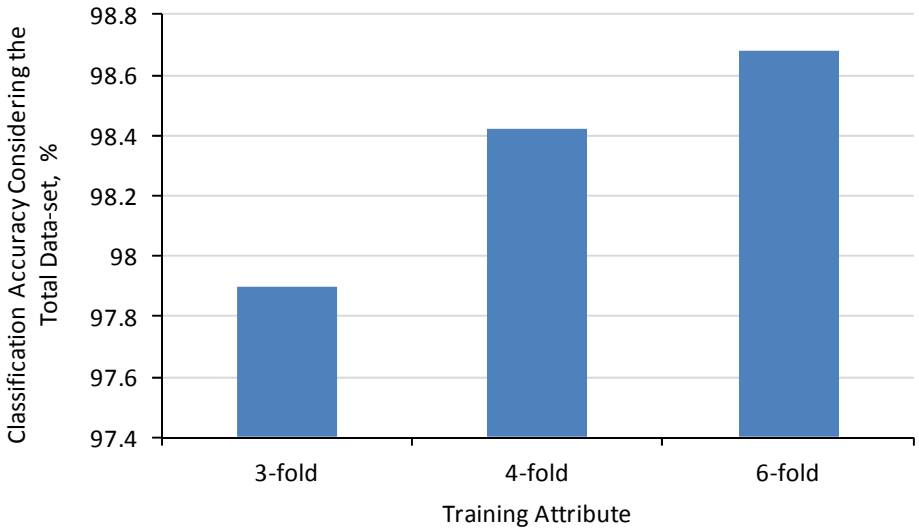

Fig. 7-3 Aggregated classification accuracy considering both training and testing data under different sizes of training dataset.

With the use of 3-fold cross validation nearly 66% of the total data were used for training. With 4-fold cross validation 75% of the total data set was used for training and with 6-fold cross validation nearly 83% of the data were used as training data. At each cross validation case the remaining portion were used as testing data.

The 4-fold cross validation gave near accurate results as the 6-fold cross validation. However, 6-fold cross validation permitted to eliminate the first level of DWT coefficients of both current and voltage signals, which was the highest frequency level. This was considered as a de-noising technique, which will be discussed later in this chapter. Therefore, the classifier trained through 6-fold cross validation was selected.

7.1.2 The Optimal Decision Tree Classifier

With the conclusions made in Section 7.2.1, the best classifier observed with 6-fold cross validation was selected as the optimal classifier for the test system shown in Fig. 7.2. The classifier gave 98.9% overall accuracy on the training dataset and 97.57% overall accuracy on testing when data from all three generators were considered jointly.

In order to study the performance of the classifier at each generator, classifier was tested with the testing data for each generator. When applied at the synchronous generator with testing data, it achieved an overall accuracy of 97.07%, while achieving 100% accuracy in identifying islanding events. With testing data for the induction generator, the classifier achieved 96.98% overall accuracy, with a 97.5% accuracy in identifying islanding events correctly. Testing at the VSC based generator gave 98.83% overall accuracy while giving a 97.06% accuracy in detecting islanding events correctly. These results are summarized in Table 7-4.

Table 7-4 Decision tree classifier trained for the new test system

	Training		Testing					
			Synchronous		Induction		VSC	
	Total Cases	Correctly Classified	Total Cases	Correctly Classified	Total Cases	Correctly Classified	Total Cases	Correctly Classified
Non-island	2,307	2276 (98.66%)	162	156 **(96.29%)**	159	154 **(96.86%)**	138	137 **(99.27%)**
Island	594	593 (99.83%)	43	43 **(100%)**	40	39 **(97.50%)**	34	33 **(97.06%)**
Total	2,901	2869 98.89%	205	199 **(97.07%)**	199	193 **(96.98%)**	172	170 **(98.83%)**

It was observed that most of the misclassifications occurred during the induction motor starting transients and unbalanced faults of 10 - 25 Ω impedance range. Transformer energizing, load switching and capacitor switching were always classified accurately as non-islanding.

The results revealed that the proposed transient based islanding detection method can be successfully applied in to any power system and it gave high level of accuracy in detecting islanding events correctly. It was also found that importance of the variables for classification task depends on the system to which the methodology is applied in. For the studied test system in Fig. 7-1, optimal DT used only six variables. It was further observed that the decision tree become complex with the expansion of the scope of the transient generating events. The trained optimal decision tree had 72 nodes.

7.2 Comparison of Classification Accuracy

In order to evaluate the robustness and reliability of the relay with confidence, a new testing data set was generated with a large set of simulation cases, including scenarios that

were not considered in generating the training data set. This new data included faults occurring at places different to those considered in preparing the training data set (at buses-4, 7 and 8). The induction motor starting transients were also changed by adding different external rotor resistance values (0.5–5Ω) and changing the value of "*k*" in the load torque equation in-between 0.75 to 1.5. The power system loading was also changed to vary the active and reactive power imbalances in the islanded portion from -60% to +60% (the percentage real/reactive power imbalance is the grid real/reactive power exchange that was lost as a percentage of the total real power consumption in the microgrid at the time of islanding). The load power factors were also changed in-between 0.9 to 1. Finally, the network topology was changed by opening and closing the switches S1 and S2 in Fig. 7-1.

The new testing data set had 250 islanding cases and 250 non-islanding cases. The events were simulated in PSCAD to compare the performance of different anti-islanding relays. The relays were designed according to the information given in Chapter 2, and included in the PSCAD simulation. Over/Under Frequency and Over/Under Voltage relay thresholds and time frames were set according to Table 2-3 and Table 2-4. VVS relay time window was set to 1/3 of a cycle and three thresholds settings of the relay were tested: 3^{o}, 10^{o}/ and 15^{o}/cycle. ROCOF relay was designed with a 2 cycle time-window, and relay thresholds of 0.1, 0.5 and 1.2 Hz/s were simulated to examine the effect of setting.

Table 7-5 Comparison of reliability of different islanding detection methods

Relay	Testing						
	Description	Synchronous		Induction		VSC	
		Correct Cases†	% Correct	Correct Cases†	% Correct	Correct Cases†	% Correct
Proposed relay	Non-islanding	238	95.2	242	96.8	243	97.2
	Islanding	246	98.4	232	92.8	229	91.6
	Overall	484	**96.8**	474	**94.8**	472	**94.4**
Over /Under Vol.	Non-islanding	250	100	250	100	250	100
	Islanding	106	42.4	107	42.8	107	42.8
	Overall	356	**71.2**	357	**71.4**	357	**71.4**
Over /Under Freq.	Non-islanding	250	100	250	100	250	100
	Islanding	186	74.4	186	74.4	186	74.4
	Overall	436	**87.2**	436	**87.2**	436	**87.2**
VVS 3^0/cycle	Non-islanding	134	53.6	132	52.8	142	56.8
	Islanding	250	100	250	100	250	100
	Overall	384	**76.8**	382	**76.4**	392	**78.4**
VVS 10^0/cycle	Non-islanding	189	75.6	189	75.6	189	75.6
	Islanding	170	68	169	67.6	170	68
	Overall	359	**71.8**	358	**71.6**	359	**71.8**
VVS 15^0/cycle	Non-islanding	189	75.6	189	75.6	189	75.6
	Islanding	96	38.4	96	38.4	96	38.4
	Overall	285	**57.0**	285	**57.0**	285	**57.0**
ROCOF 0.1 Hz/s	Non-islanding	217	86.8	214	85.6	218	87.2
	Islanding	250	100	250	100	250	100
	Overall	467	**93.4**	464	**92.8**	468	**93.6**
ROCOF 0.5 Hz/s	Non-islanding	241	96.4	238	95.2	245	98
	Islanding	224	89.6	224	89.6	224	89.6
	Overall	465	**93**	462	**92.4**	469	**93.8**
ROCOF 1.2 Hz/s	Non-islanding	249	99.6	249	99.6	250	100
	Islanding	197	78.8	197	78.8	195	78
	Overall	446	**89.2**	446	**89.2**	445	**89**

†The test data set included 250 non-islanding cases and 250 islanding cases.

Table 7-5 summarizes the achieved results. The proposed relay at the synchronous generator gave 98.4% dependability and 95.2% security level. The corresponding values for the induction generator were 92.8% and 96.8% respectively and same for the VSC based source were 91.6% and 97.2% respectively. The overall classification accuracy of the proposed relay was 95.33% in considering all three generators together.

Most of the misclassifications in islanding detection with the proposed method were observed with the VSC based generator, for the non-trained events happening at near zero power imbalances. Thus, it is important to train the classifier in all possible power imbalances. However, synchronous generator showed robust performance giving high level of dependability and security for untrained levels of power imbalances as well. This testing also confirmed that most of the misclassified non-islanding events were the induction motor starting transients.

Table 7-5 reveals that the proposed method with 95.33% overall classification accuracy, showed the highest reliability when tested under the entire span of considered power imbalances. The next best accuracy was obtained with the ROCOF relay at 0.5 Hz/s relay setting, but its islanding detection accuracy was lower than that of the proposed relay for all the generators. The ROCOF relay also presented a higher detection times under near zero power imbalances, which is discussed in next two sections. VVS relays and ROCOF relay with low settings (3^0/cycle and 0.1Hz/s respectively) showed 100% dependability but, they gave high level of nuisance tripping presenting a low level of security. VVS relay at its high settings (10^0/cycle and 15^0/cycle) showed neither good dependability nor good security. Over/under voltage relay and the over/under frequency

relay showed a 100% security, but dependability was very low, especially under near-zero power imbalances.

The above observations are based on a test data set, which could be considered as a random sample of an infinite population. Thus, it was necessary to establish the confidence intervals for the observed population proportions. This experiment could be considered as binomial because, the trials were independent, each trial resulted in only two possible outcomes ("correctly classified" and "misclassified"), and the probability of a success on each trial (p) remained constant. Confidence interval on a binomial proportion can be found by normal approximation. This is valid only if p is not too close to 0 or 1 and if the number of samples (n) is relatively large. The rule of thumb to apply this approximation is that np and $n(1-p)$ must be greater than or equal to 5 [101]. With n=1500, (considering the observations at all three generators, $n = 3 \times 500$), the dataset satisfy the above requirements for normal approximation.

The confidence interval on a proportion is defined as follows [101]:

"If $\hat{p}$ is the proportion of observations in a random sample of size n that belong to a class of interest, then an approximate 100(1-α) percent confidence interval on the proportion p, of the population that belongs to this class is:

$$\hat{p} - z_{\alpha/2}\sqrt{\frac{\hat{p}(1-\hat{p})}{n}} \le p \le \hat{p} + z_{\alpha/2}\sqrt{\frac{\hat{p}(1-\hat{p})}{n}} \tag{7.1}$$

Where $z_{\alpha/2}$ is the upper $\alpha/2$ percentage point of the standard normal distribution" [101].

Thus, to calculate the 99% confidence interval, α =1-0.99 = 0.01, and from normal distribution, $z_{\alpha/2}$ = 2.58. The estimated probability of accurate classification by the proposed relay, using the 1500 observations is:

$$\hat{p} = \frac{238 + 242 + 243 + 166 + 163 + 159}{1260} = 0.9533$$

Therefore, based on (7.1), the 99% confidence interval for the probability of correct classification, p is: $0.939 \leq p \leq 0.967$ for the proposed relay. Likewise, 99% confidence intervals for all other relays were calculated.

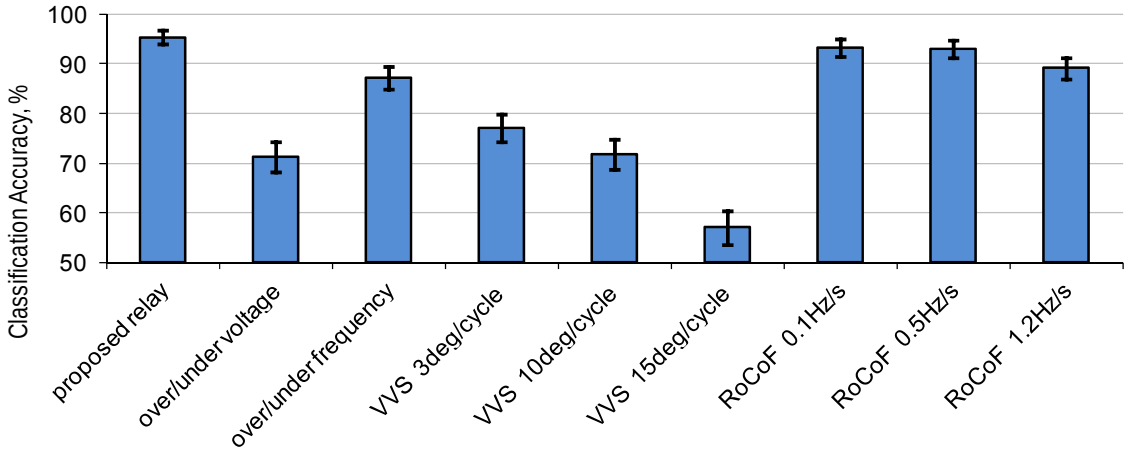

Fig. 7-4 Classification accuracy with 99% confidence interval.

Fig. 7-4 presents the classification accuracy of islanding detection relays with 99% confidence intervals marked by the error bars. It can be concluded with 99% confidence, that the classification accuracy of proposed relay is higher than all other relays, even when testing includes some system configurations and power imbalances unseen during the training of the classifier.

7.3 Comparison of Response Time

Speed of detection is one of the advantages expected in the proposed transient based islanding detection scheme. In order to investigate whether there is significant advantage

compared to the other methods, the response times of all the relays for the 250 islanding cases simulated were recorded. Fig. 7-5 presents the responses of the synchronous generator terminal quantities for a system islanding event occurred at t = 9s. This islanding event creates an active power imbalance of 40% and reactive power imbalance of 60%.

The graphs show the time variations of the terminal voltage, frequency, rate of change of frequency, cycle length of voltage waveform as estimated by the VVS relay, and logarithmic value of "three phase energy contents" of the voltage and current wavelet coefficients. Table 7-6 presents the minimum, maximum and average detection times of the relays for the 250 islanding cases tested. If the response times were above 2 s, those cases were considered non-detected and omitted for each relay in presenting its average detection times.

The maximum detection time for the proposed relay was 48 ms (3 cycles) and it was observed for the VSC based dc source. The average detection time of the proposed relay was less than 30 ms (less than two cycles). Although VVS relays gave faster or comparable response times, it was associated with high level of nuisance trip signals. ROCOF relays' response times depended on the relay setting. The average detection time observed for the lowest ROCOF relay setting (0.1 Hz/s) was nearly 0.16 s. ROCOF relay of 0.5 Hz/s, which gave high accuracy level presented an average detection time of nearly 0.32 s. The Over/Under Frequency relay showed a slow response taking an average detection time of nearly 0.96 s at all the generators. The Over/Under voltage relay showed poor performance in terms of both islanding detection accuracy and response time. The average islanding detection time of the Over/Under voltage relay was around 0.65 s.

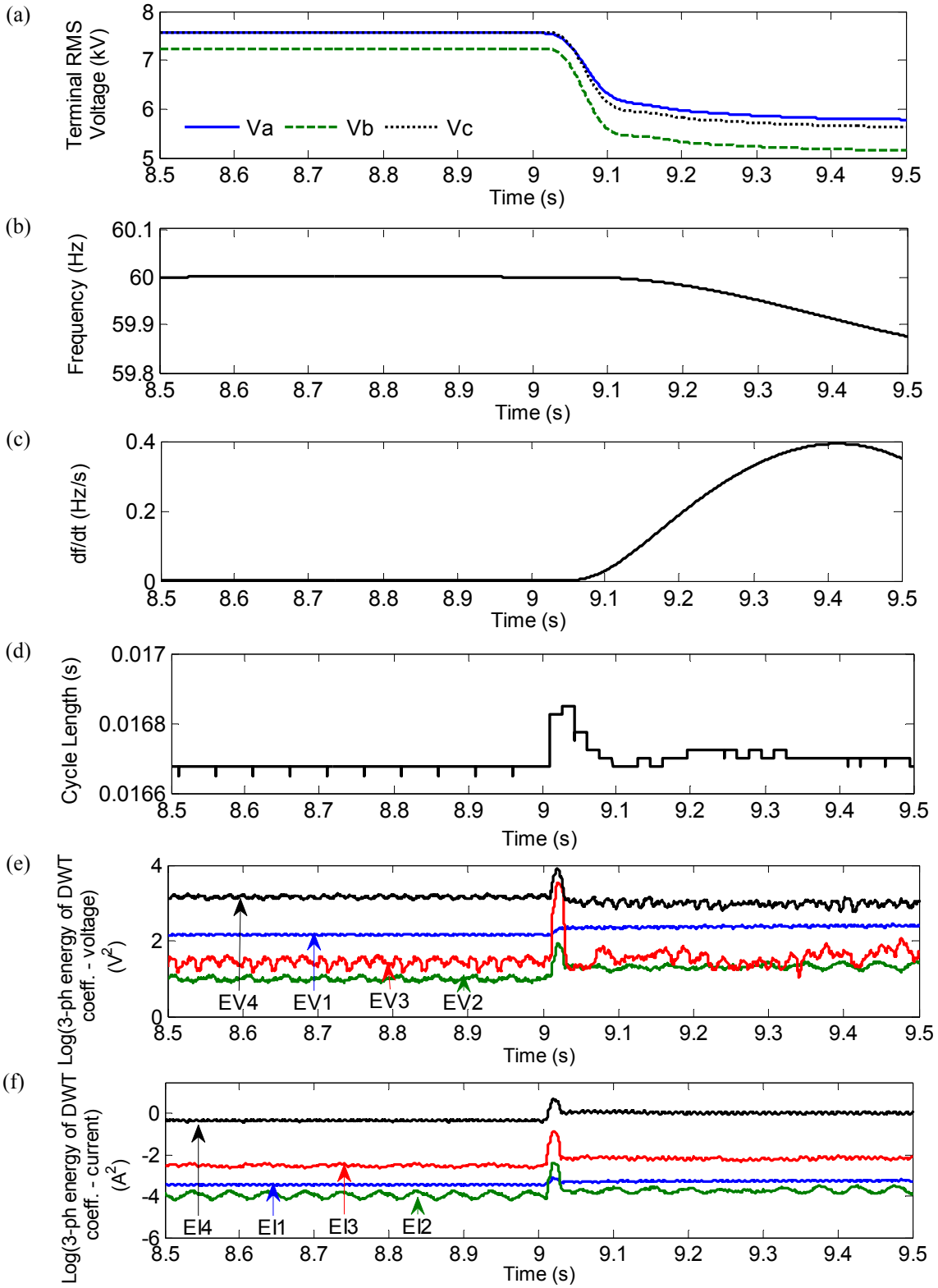

Fig. 7-5 Terminal responses at the synchronous generator: (a) RMS voltage, (b) frequency, (c) rate of change of frequency, (d) cycle length of voltage waveform, (e) log of energy content of voltage wavelet coefficients, (f) log of energy content of current wavelet coefficients.

Table 7-6 Comparison of response time of different islanding detection methods

Relay	Detection Time (s)								
	Synchronous			Induction			VSC		
	Min	Avg	Max	Min	Avg	Max	Min	Avg	Max
Proposed relay	0.021	0.026	0.034	0.021	0.0264	0.046	0.016	0.0253	0.048
Over/Under Vol.	0.240	0.649	1.290	0.241	0.650	1.299	0.239	0.628	1.296
Over/Under Freq.	0.608	0.964	1.974	0.607	0.964	1.974	0.606	0.963	1.974
VVS 3^0/cycle	0.005	0.011	0.027	0.005	0.010	0.027	0.005	0.011	0.027
VVS 10^0/cycle	0.007	0.015	0.023	0.007	0.013	0.023	0.007	0.013	0.023
VVS 15^0/cycle	0.011	0.028	0.433	0.011	0.023	0.433	0.011	0.023	0.433
ROCOF 0.1Hz/s	0.096	0.164	0.734	0.096	0.163	0.736	0.096	0.162	0.743
ROCOF 0.5Hz/s	0.152	0.323	1.517	0.151	0.322	1.517	0.150	0.321	1.517
ROCOF 1.2Hz/s	0.211	0.456	1.750	0.210	0.456	1.750	0.209	0.455	1.750

Although not statistical or graphical, a discussion on active islanding detection methods with a comparison against passive methods is presented in [17]. It indicates that the active methods have high dependability and security levels but the detection times are concluded to be longer than passive methods [17], [22]. Also, some active methods cannot be applied with all types of generators [17]. The methods like reactive power fluctuation cannot be applied with induction generators and the load fluctuation methods cannot be applied with VSC based sources. Inter-harmonic injection methods are said to be applicable with any type of generator but, continuous injection of harmonics affects the power quality. Telecommunication based methods are highly dependable and fast responding depending on the type of communication used [22]. In general, response times of these methods vary between 30 ms and 1.7 s [22]. The drawback of this method is it being complex and costly compared to passive islanding detection methods [80].

7.4 Effect of Power Imbalance and Non-Detection Zones

The "*Power imbalance*" in this thesis was defined in (4.1), as the grid power being lost as a percentage of the total power consumption in the islanded part just before islanding. The response times of the relays for islanding events were monitored under varying active and reactive power imbalance conditions (-60% to +60%). This investigation was carried out as two different cases to illustrate the results with a higher confidence. The islanding events corresponding to each power imbalance levels in the two cases were corresponding to two distinctly different situations in the microgrid. Therefore, two cases represented different power-flow situations in the islanded microgrid at each power imbalance level.

In order to vary the real power imbalance, the synchronous generator operating point was changed in the range of 0.6 pu to 1 pu, and different loading conditions were considered. The required reactive power imbalances were created by switching the capacitors and changing the load power factors. The results are presented in 3-D plots drawn for the observations at the synchronous generator, representing the active power imbalance in x-axis, reactive power imbalance in y-axis and relay response times in z-axis. The events that did not detect the islanding within 2 s were considered as non-detected. Figs. 7-6 to 7-14 illustrate the response times of islanding detection by different relays, and results for case-1 are marked by *(a)* and case-2 are marked by *(b)*. The relays at the wind turbine and VSC based dc source showed similar responses.

The Non-Detection-Zone (NDZ) of each relay can be found by chopping the surfaces using a horizontal plane at the detection time of interest. These figures are drawn for a 2 s time frame for islanding detection, and therefore, the plateau on the 3-D plot represents the NDZ of each relay, on the P-Q plane.

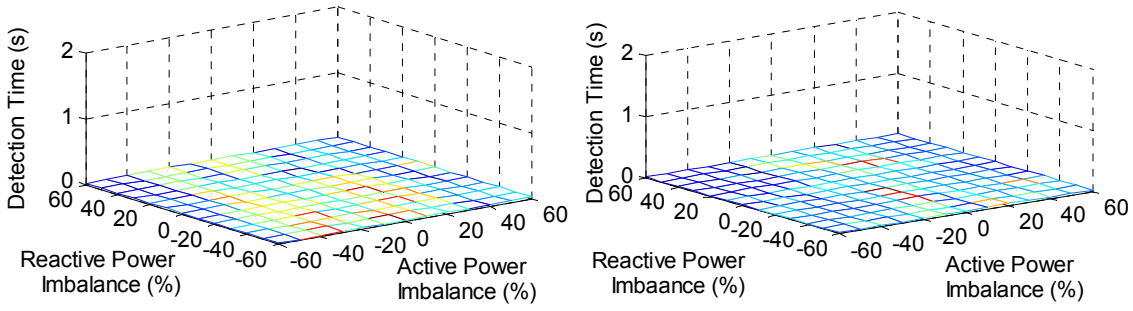

(a) (b)

Fig. 7-6 Variation of islanding detection times of the proposed relay (DT) with varying active and reactive power imbalances (a) Case-1, (b) Case-2.

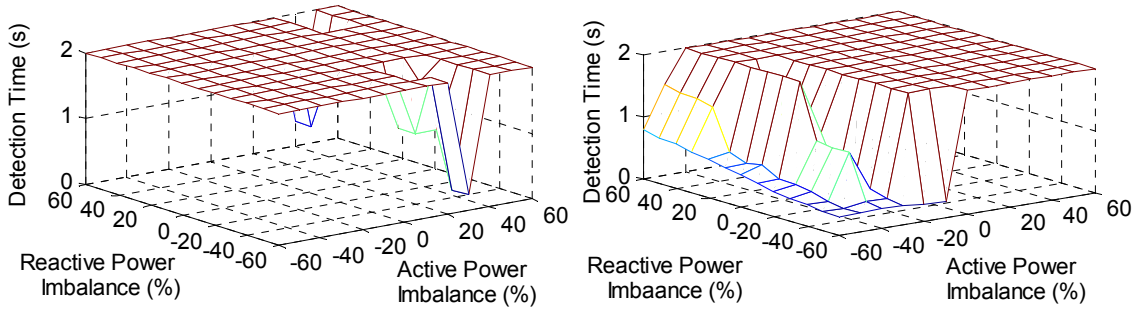

(a) (b)

Fig. 7-7 Variation of islanding detection times of Over/Under Voltage relay with varying active and reactive power imbalances (a) Case-1, (b) Case-2.

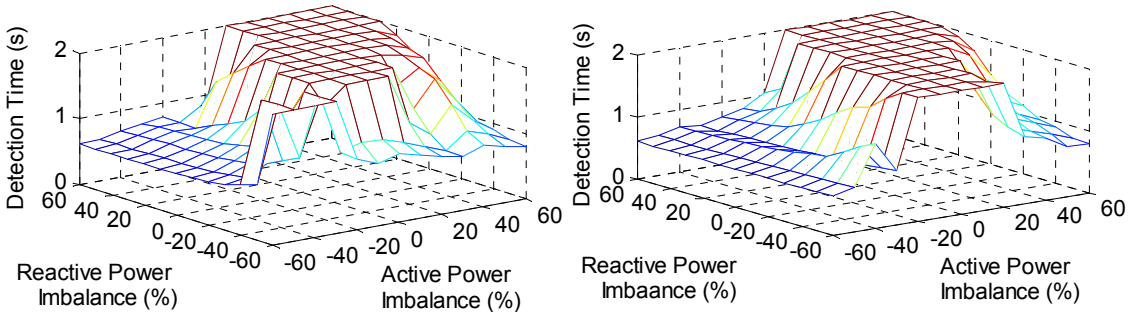

(a) (b)

Fig. 7-8 Variation of islanding detection times of Over/Under Frequency relay with varying active and reactive power imbalances (a) Case-1, (b) Case-2.

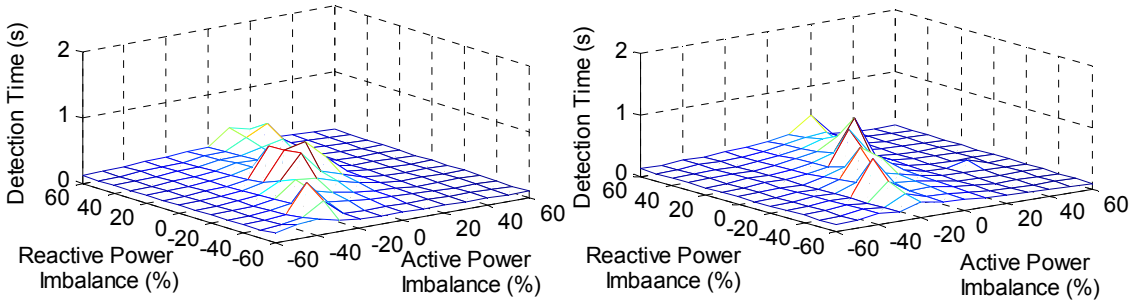

(a) (b)

Fig. 7-9 Variation of islanding detection times of ROCOF relay at 0.1 Hz/s setting under varying active and reactive power imbalances (a) Case-1, (b) Case-2.

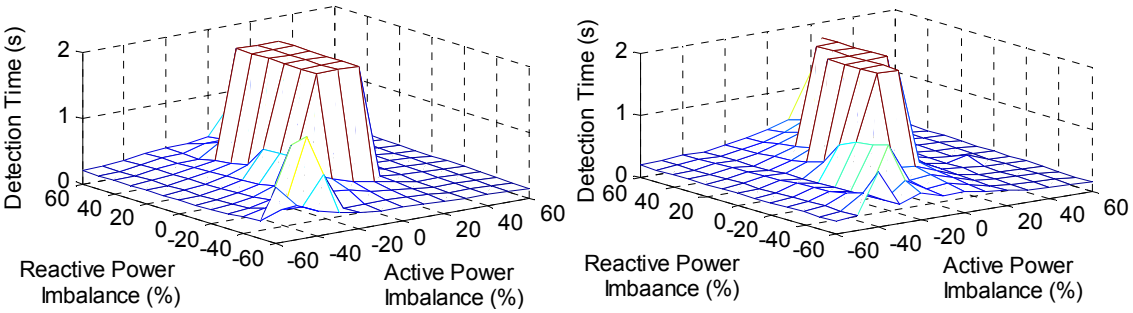

(a) (b)

Fig. 7-10 Variation of islanding detection times of ROCOF relay at 0.5 Hz/s setting under varying active and reactive power imbalances (a) Case-1, (b) Case-2.

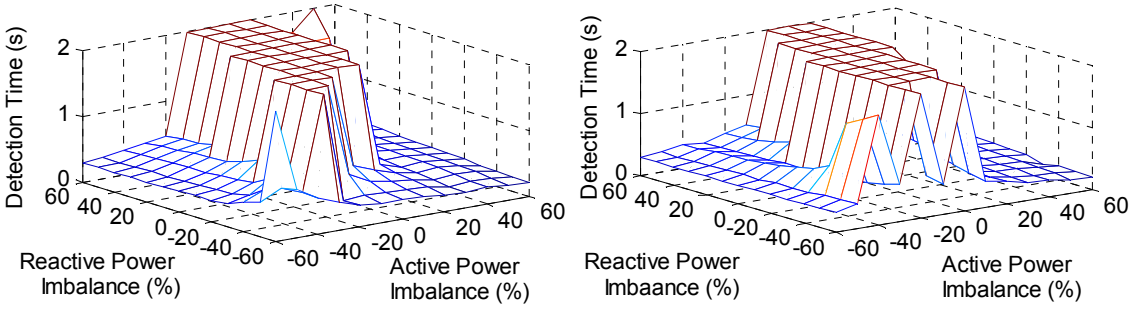

(a) (b)

Fig. 7-11 Variation of islanding detection times of ROCOF relay at 1.2 Hz/s setting under varying active and reactive power imbalances (a) Case-1, (b) Case-2.

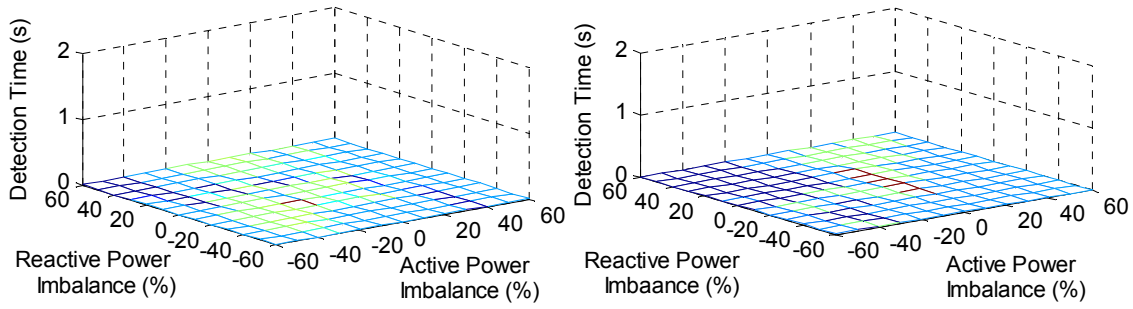

(a) (b)

Fig. 7-12 Variation of islanding detection times of VVS relay at 3°/cycle setting under varying active and reactive power imbalances (a) Case-1, (b) Case-2.

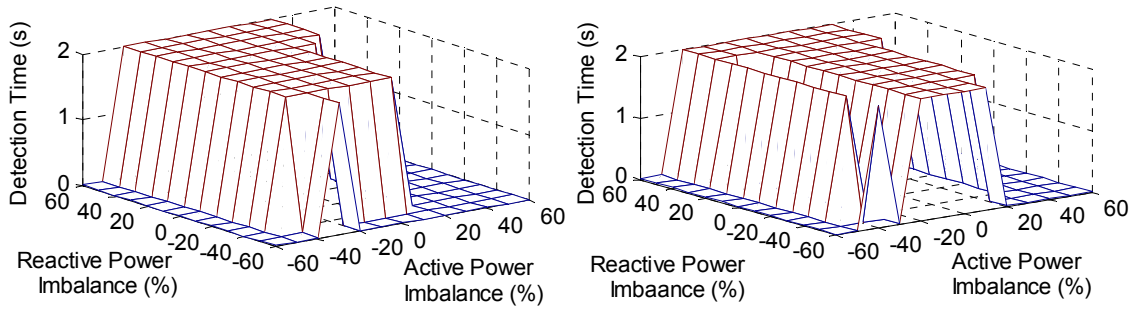

(a) (b)

Fig. 7-13 Variation of islanding detection times of VVS relay at 10°/cycle setting under varying active and reactive power imbalances (a) Case-1, (b) Case-2.

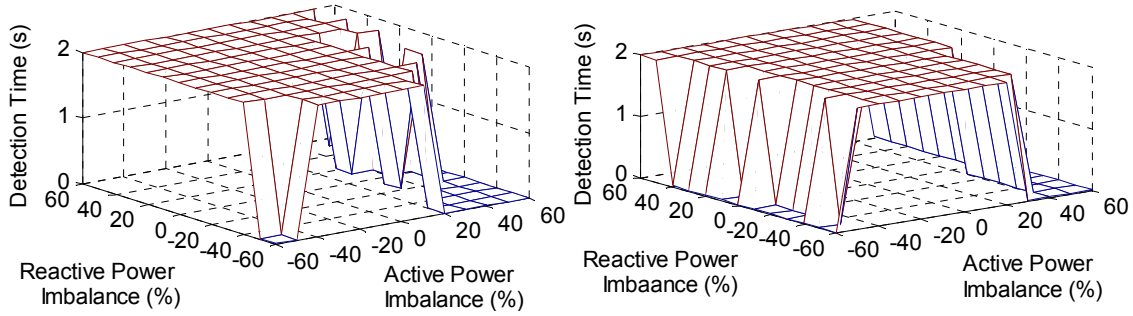

(a) (b)

Fig. 7-14 Variation of islanding detection times of VVS relay at 15°/cycle setting under varying active and reactive power imbalances (a) Case-1, (b) Case-2.

Fig. 7-6 shows that the proposed relay had a zero NDZ, and the response time of the relay was very much independent from the power imbalance. Similar response could be observed with the VVS relay at 3°/cycle setting, which is shown in Fig. 7-12. However, it

showed a very high degree of nuisance triggering in testing its accuracy. Also, the figures present that higher the setting of the relay, very much larger were the NDZ for both ROCOF and VVS relays. With reference to Fig. 7-9, ROCOF relay at the lowest setting (0.1 Hz/s) had a zero non-detection zone but the response time depended on the power imbalance, which agreed with the theory. But, ROCOF relay at 0.1 Hz/s presented a high level of triggering at non-islanding events. Conversely, Fig. 7-8 shows that Over/Under frequency relay had a considerably large NDZ, although it was very accurate in identifying non-islanding events.

Over/Under voltage relay showed very poor performance with a higher detection times and a considerably large NDZ, as can be seen in Fig. 7-7. For the same active and reactive power imbalance, there was a difference in the power-flows within the islanded microgrid for the two cases (Case-1 and Case-2), which corresponds to Fig. 7-7 (a) and (b). Therefore, the voltage dip was not alike for each power imbalance for the two cases. This had resulted in dissimilar response-time graphs as shown in Fig. 7-7 (a) and (b). Furthermore, Over/Under voltage settings were set according to Table 2-3, which is recommended by IEEE standard 1547-2003 [10]. As shown in Table 2-3, the relay has 4 threshold levels: if the voltage goes lower than 50% or higher than 120% of the rated, the relay is triggered in 16 ms; If the voltage level is in-between 110% and 120% for a period longer than 1 s, the relay is triggered; And the relay is triggered only after 2 s, if the voltage level is in-between 50% and 88% of rated value. Therefore, the large NDZ and some fast detecting events observed in the graphs (a) and (b) happened due to the relay settings, and system behavior with the corresponding power imbalance.

7.5 Effect of Signal Noise

The quality of wavelet energy calculations can be degraded by the presence of noise in practical environments, and it is one of the major challengers in implementing transient based relays.

The effect of signal noise on DWT coefficients is illustrated in Fig. 7-15 and Fig 7-16, which shows the original waveform and the DWT coefficients for four levels (Level-1: 5000-2500Hz; Level-2: 2500-1250Hz; Level-3: 1250-625 Hz; Level-4: 625-312.5Hz) for voltage and current transients observed during an islanding event. For the figures illustrated, the current signals were contaminated with random noise giving 10 dB Signal to Noise Ratio (SNR) and a random noise giving 50 dB SNR was introduced to voltage signals. Fig. 7-15 shows that only level-1 DWT coefficient of the voltage signal was significantly changed with noise of 50 dB SNR presented in the voltage signal. However, Fig. 7-16 shows that, having a very high level of signal noise (10 dB), all the coefficients of DWT of current signals were significantly changed compared to those without signal noise.

The effect of measurement noise on the wavelet based algorithms can be reduced through de-noising techniques [102]-[103], but this may compromise the speed of detection. Reference [104] introduces s-transform as an alternative transform with high noise immunity for classification of disturbances. But, for real time application such as the one proposed in this thesis, faster calculation speed of DWT compared to s-transform [105] could be critically important.

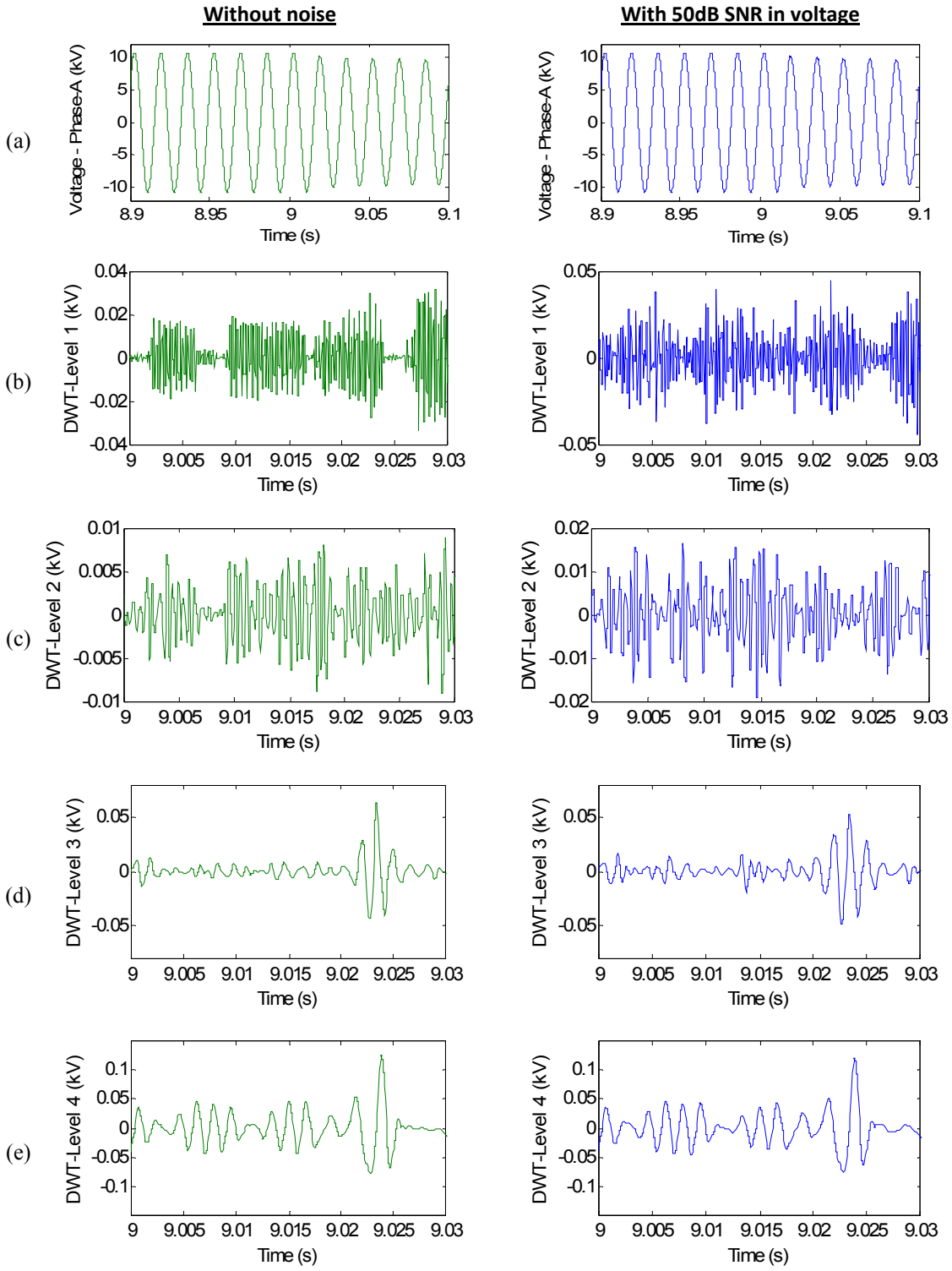

Fig. 7-15 Comparison of the original signal and DWT coefficients of Phase-a terminal voltage at the synchronous generator for an islanding event happening in the system with and without signal noise.

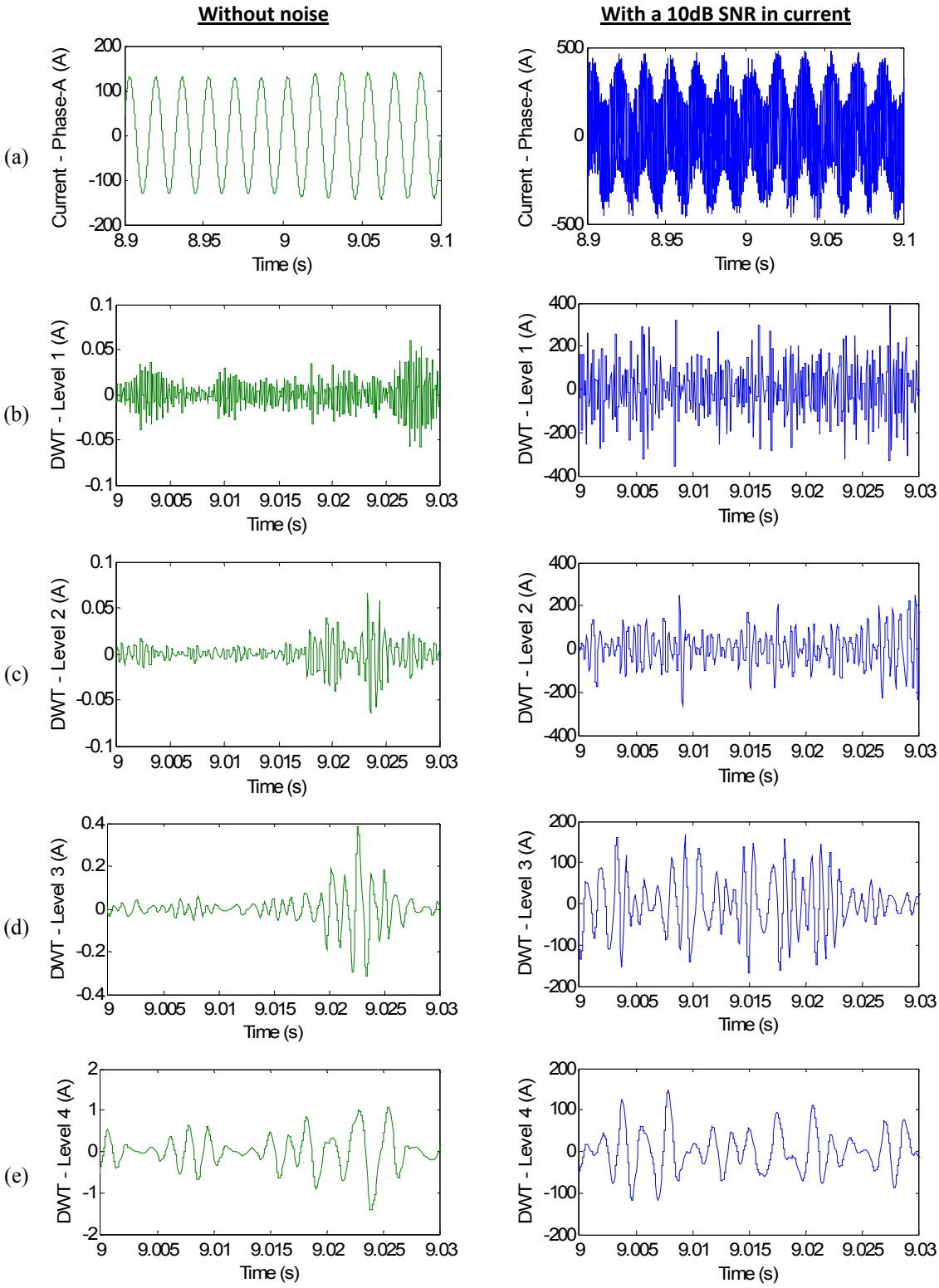

Fig. 7-16 Comparison of the original signal and DWT coefficients of Phase-a terminal current at the synchronous generator for an islanding event happening in the system with and without signal noise.

The DT classifier designed for the islanding detection relay was not trained with noisy data. In order to investigate the effect of noise on islanding detection accuracy, the designed classifier was tested with a set of noisy data. The data set included 25 islanding cases and 25 non-islanding cases with an added random noise to the current and voltage signal.

Tests revealed that even with highly distorted current signal having 10 dB SNR, the classifier performed perfectly in determining both islanding and non-islanding situations, if a noise free voltage signal was used. The tests also showed that classification of non-islanding events was less affected by noise. All the non-islanding cases tested were accurately classified even under 10 dB noise level in both current and voltage signals. Fig. 7-17 show the variation of classification accuracy with changing SNR in terminal voltage signal while having 10 dB SNR in the current signal, for the synchronous generator, induction generator and VSC based source. Fig. 7-17 shows that, the classification accuracy of islanding events started to degrade when the SNR of voltage signals was below 50 dB, if the current signal was already noisy (10 dB SNR).

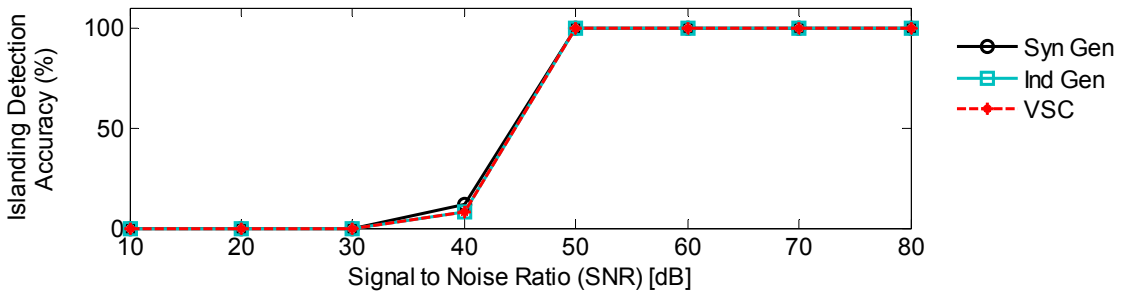

Fig. 7-17 Classifier accuracy with changing SNR in voltage signal with 10dB SNR present in the current signal.

The robustness against the noise can be explained by analysing the DT design. The elimination of features derived from level-1 wavelet coefficients helped, as those are the coefficients highly susceptible to signal noise, which was observed in Figs. 7-15 and 7-16. In effect, the signal was somewhat denoised when these high frequency coefficient were removed. The classifier was more robust against the noise in current, because the features derived from DWT coefficients of current signal were the less important compared to the features derived from voltage signals, according the variable importance results provided by CART software during the training. This interprets the theory behind defining the variable importance in the DT. Although the DT had 72 nodes, the first few internal nodes, which were the features derived from voltage signals completed the most of the classification task. Furthermore, robustness of the classifier could have been improved if trained with noisy data.

7.6 Effect of Grid Side Impedance

The grid side impedance can possibly be changed with the connection and disconnection of parallel transformers at the substation and/or due to many other reasons. The proposed relay was based on recognizing the patterns of transients generating at the event of an island. Therefore, it was important to study whether there is an effect of changing the grid side impedance on the features used for classification and consequently on accuracy of the proposed islanding detection relay.

Fig. 7-18 illustrates the original waveform and the DWT coefficients for four levels (Level-1: 5000-2500Hz; Level-2: 2500-1250Hz; Level-3: 1250-625 Hz; Level-4: 625-

312.5Hz) for voltage transients of phase-A observed at the synchronous generator terminal during an islanding event.

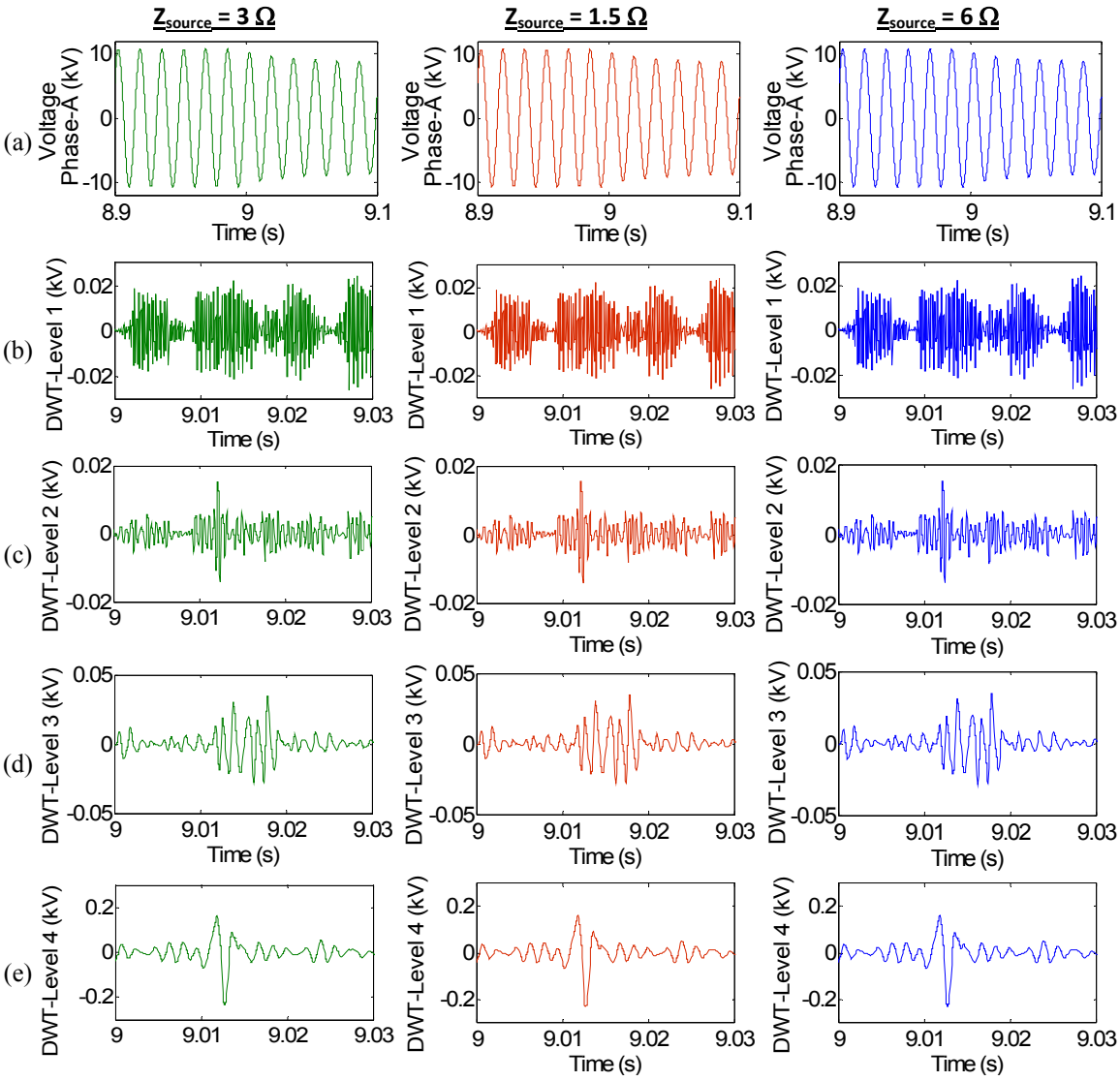

Fig. 7-18 Comparison of the original signal and DWT coefficients of Phase-a terminal voltage at the synchronous generator for an islanding event at different grid side source impedances.

The waveforms are shown for the same islanding event happening at 100%, 50% and 200% of the grid side source impedance [39] as that used in creating the islanding detection relay. In comparing the DWT coefficients at the three source impedances, they had

identical characteristics. The same similarity was observed with current transients at the islanding. Therefore, the proposed islanding detection relay could be predicted to be robust under different grid side impedances.

To validate the prediction, the relay accuracy was tested with 25 islanding events and 25 non-islanding events under 100%, 50% and 200% of the grid side source impedance. The observed results validated the expected outcome giving 100% accuracy in classifying all the islanding and non-islanding events correctly at all three generators, under the three grid side source impedances that were tested. Therefore, the proposed relay was robust against the changing grid side impedances.

7.7 Hardware Implementation

The possibility of hardware implementation of this proposed algorithm was investigated in the work presented in [106]. In [106], the same approach was used for detecting power islands, with feature extraction part replaced with analog electronics to achieve a low cost. However, with the powerful digital signal processing hardware available today, fully digital implementation of the proposed algorithm is not difficult.

It is recommended that initially, the islanding detection relay is trained with simulated transient events data and tested with real time simulations. The relay should then be field tested by monitoring its performance for a sufficient period of time (say one year) recording the transients and relay responses. The observations and recordings can be used to further improve and judge the performance of the proposed transient based islanding detection method.

7.8 Concluding Remarks

This chapter evaluated the performance of the islanding detection method proposed in this thesis. The proposed islanding detection method uses decision tree classifier and it detects the islanding events based on the transient signals generated during the grid disconnection.

The study was extended by applying the methodology into a system with a dc source connected via a VSC. The simulation based tests asserted that the proposed relay has 95.33 ± 1.405% overall classification accuracy, with 99% confidence. Most of the misclassifications were observed with induction motor starting transients. The test cases involved unlearned system configurations and the observed accuracies showed relay's robust performance under such conditions.

The response time of the relay was less than three cycles for the synchronous generator, the VSC based dc source and the induction generator under all the cases tested. These response times were invariant with the power imbalance in the power island and the methodology gave a zero NDZ with any type of generator, if trained considering the possible power imbalances.

For the MV distribution system studied, the proposed transient based classification method showed better performance when compared with the other passive anti-islanding relays in use: the proposed relay had a higher dependability, higher security, faster response time, less sensitivity to load imbalance and a zero NDZ. It was also found to be robust against the noise in current and voltage signals, if designed eliminating the lower

level DWT coefficients from the classification feature set. The proposed relay showed robust performance under variable grid side source impedances as well.

This chapter also compared the performance of the conventional islanding detection techniques under a comprehensive set of test conditions.

Chapter 8

Conclusions and Contributions

This chapter presents the conclusions of the research, summarizes the main contributions and proposes directions for future research in the area of transient based islanding detection and microgrids.

8.1 Conclusions

The thesis investigated the problems associated with interconnecting microgrids to the utility grid. The main focus of the research, in the first two stages was to identify the microgrid performance during and immediately after the transition from parallel to islanded operation and vice versa. The findings lead to explore for a fast responding reliable islanding detection method as the third major part of the research. Thesis proposed a transient based islanding detection technique that uses pattern recognition to predict islanding in a distribution system. The fast response of the proposed islanding detection technique allows changing the microgrid control mode from parallel to islanded operation in less than two cycles on average and thereby achieving the frequency and voltage sta-

bility of the islanded microgrid with minimum load shedding. The major conclusions drawn from the thesis are given below.

The literature review established the current state-of-the art of microgrids, particularly the control, synchronization and islanding detection techniques. There are many variations in microgrid architecture and design. However, they are implemented with common objectives such as reliability and optimal integration of DGs. Review of many experimental microgrid projects around the world revealed that most projects use conventional strategies for preserving the frequency and voltage stability during the autonomous operation. Identifying the dependable control strategies and utilizing them accordingly to further improve the system reliability is a key requirement. The literature review also highlighted the need for a generic microgrid simulation model that reflects the properties of the present microgrids to facilitate further research on transient stability performance, protection, control and design standards for microgrids.

A substation microgrid simulation model was developed based on the proposed CIGRE MV test system. The microgrid model included a synchronous generator, an induction generator and an inverter interfaced generator. This enabled studying the responses of all major types of generators used in distributed generation to various events. The use of more conventional frequency and voltage control methods in the microgrid design made it generic, and closer to some of the existing experimental microgrid test systems. Through simulation of various scenarios, it was established that the developed microgrid test system conforms to main requirements in the IEEE standard 1547.4-2011 on *Guide for Design, Operation, and Integration of Distributed Resource Island Systems with Electric Power Systems*.

The frequency and voltage stability of a microgrid at the transition from parallel to islanded operation and vice versa was investigated. Investigations revealed that the control mode transition delay has a significant impact on the amount of load that needed to be shed to preserve the islanded microgrid stability. If the control mode was changed within 50 ms from islanding, the MV substation microgrid considered in this study attained the same frequency and voltage responses that were observed when the control mode was changed without any delay, irrespective of the value of embedded inertia of the system. At higher embedded inertia, the microgrid became more robust, and tolerated a longer transition delay. The above conclusions pointed to the benefits of having a fast and reliable islanding detection device to activate control mode transition. These conclusions were drawn for a substation level microgrid with a synchronous generator and no energy storage. Therefore, the validity of the results must be checked before application to microgrids with fast responding energy storage of significant capacity.

The transition of a microgrid from islanded to parallel operation maintaining the system power quality was investigated. The application of automatically controlled switched capacitor banks for voltage balancing in an islanded microgrid, and for achieving the voltage magnitude criteria for synchronization was explored. According to the investigations, it is possible to meet the voltage quality of the microgrid and synchronization requirements specified in the standards with simple switched capacitors connected at the POI. Only the passive synchronization, which is most likely to be used in most situations, was considered in the study. According to the results, the traditional synchro-check relays can satisfactorily synchronize a MV substation microgrid with the utility grid. The main factor that impacts the smoothness of transition is the phase angle difference be-

tween the utility and microgrid voltages. The results of the studies in this chapter suggest that when the switched capacitors are used at the POI, it may be desirable to relax the voltage difference threshold of the synchro-check relay to reduce the initial current transients during the reconnection of the microgrid to the utility grid.

The above investigations on transition from islanded to parallel operation of the microgrid indicate that existing technologies and procedures with appropriate modifications can be effectively used to achieve the required operating standards of a MV microgrid. However, the requirement for fast, reliable and economical islanding detection method was attested from the investigations on transition of microgrid from parallel to islanded operation. Inability of existing passive islanding detection methods to meet the fast detection times demanded by MV microgrids was highlighted. As a possible solution, a novel fast islanding detection technique was proposed. In a step by step approach, the hypothesis behind the new islanding detecting technique, “the transients generated during an islanding event embed unique signatures that can be exploited to identify the event using a suitable pattern recognition technique”, was proved. A methodology for feature extraction, feature selection and classifier selection was developed in designing the proposed transient based islanding detection technique. The best islanding detection performance was obtained with a Decision Tree classifier that used the energy associated with the wavelet coefficients of the transient current and voltage signals as input features. When tested with a large number of simulated events for a system having a synchronous generator and an induction generator, the proposed technique showed over 98% accuracy at 95% confidence level. The response time of the proposed relay remained below two cycles for all test cases.

The performance and robustness of the proposed transient based islanding detection technique was evaluated in comparison to established passive islanding detection techniques. New tests were performed for a system that included a dc source connected via a VSC. The simulation based tests asserted that the proposed relay had 95.3 ± 1.4% overall classification accuracy, with 99% confidence. Most of the misclassifications were observed with induction motor starting transients. The test cases included unlearned system configurations and the observed accuracies indicated the robustness of the proposed islanding detection method in responding to unseen conditions. The response time of the relay was less than three cycles under all the cases tested. These response times were invariant with the power imbalance in the power island and the proposed methodology gives a zero non detection zone with any type of generator, if trained considering all possible power imbalances.

In terms of dependability, security, response time, sensitivity to load imbalance and the size of NDZ, the proposed transient based classification method showed better performance when compared with the other passive anti-islanding relays in use. It was also found to be robust against the noise in current and voltage signals, if designed eliminating the lower level DWT coefficients from the classification feature set. The proposed relay showed robust performance under varying grid side source impedances as well.

Since the islanding detection was carried out by using a classifier trained using examples, the classifier needed to be re-trained whenever there was a major change to the microgrid, such as addition of new generators. The decision tree classifier can become complex with the inclusion of large set of different transient patterns.

The thesis as a whole researched interconnecting microgrids to the utility grid. It proposed and verified the solutions to the identified specific requirements in transition of a microgrid from islanded to parallel operation and vice versa. The findings in this thesis provide resources for further research in the area of microgrids and islanding detection. Furthermore, the test network model developed in this thesis can be used for testing new microgrid control and protection solutions.

8.2 Contributions

The main contributions of the thesis are listed below:

1. Design and implementation of a substation level microgrid test system on an electromagnetic transient simulation program, and verification of the microgrid design with respect to IEEE standard 1547.4-2011. This detailed microgrid test system simulation model can be used for further studies on control, power quality, and protection of microgrids.
2. Demonstration of the impact of control mode transition delay on the frequency and voltage stability, and power quality of an islanded microgrid, and introduction of the notion of "critical control mode transition delay" to characterize this impact.
3. Demonstration of the effectiveness of switched capacitors installed at the POI for balancing and regulating the voltage in an islanded microgrid.
4. Confirmation of the adequacy of the existing synchro-check relay for synchronization of a MV microgrid, and identification of phase angle difference between the voltages

measured across the main breaker at POI as the most significant factor, which impacts the power quality.

5. Demonstration of the possibility of reducing the transient inrush current during synchronization of a microgrid supported with switched capacitors at the POI, by relaxing the voltage threshold of the synchro-check relay from the specified standards.
6. Proof of the possibility of using pattern recognition techniques to classify transients generated during islanding from other transients and development of an islanding detection techniques based on this principle.
7. Comparison of the performance of main passive islanding detection methods in a microgrid environment.
8. These contributions led to the following publications in journals and conferences.

Journal Papers

- **N. W. A. Lidula** and A. D. Rajapakse, "Microgrids research: A review of experimental microgrids and test systems," *Renewable and Sustainable Energy Reviews Journal*, vol. 15, pp. 186–202, 2011.
- **N. W. A. Lidula** and A. D. Rajapakse, "A Pattern Recognition Approach for Detecting Power Islands Using Transient Signals—Part I: Design and Implementation," *IEEE Transactions on Power Delivery*, vol. 25 (4), pp. 3070 - 3077, October 2010.
- **N. W. A. Lidula** and A. D. Rajapakse, "A Pattern Recognition Approach for Detecting Power Islands Using Transient Signals—Part II: Performance Evaluation," *IEEE Transactions on Power Delivery*, Accepted and early access available at IEEE Xplore.

- **N. W. A. Lidula**, A. D. Rajapakse, D. Muthumuni and C. Senkow "A Study on Microgrid Control Mode Transition from Grid Connected to Islanded Operation," *IEEE Transactions on Sustainable Energy*, Submitted May 2011, Revised February 2012.
- **N. W. A. Lidula** and A.D. Rajapakse, "Voltage Balancing and Synchronization of a Microgrid with Highly Unbalanced Loads," *IEEE Transactions on Power Delivery*, Submitted February 2012.

Conference Papers

- **N. W. A. Lidula**, N. Perera, A. D. Rajapaksse, "Investigation of a Fast Islanding Detection Methodology Using Transient Signals," in *Power & Energy Society General Meeting, 2009. PES '09. IEEE*, pp. 1-6.
- **N. W. A. Lidula** and A. D. Rajapakse, "Fast and Reliable Detection of Power Islands Using Transient Signals," in *IEEE International Conference on Industrial and Information Systems (ICIIS)*, 2009, pp. 493 – 498.
- Jean-Paul Pham, N. Denboer, **N. W. A. Lidula**, N. Perera, and A. D. Rajapakse, "Hardware implementation of an islanding detection approach based on current and voltage transients," in *IEEE Electrical Power and Energy Conference, IEEE EPEC 2011,* pp.152-157.

8.3 Suggestions for Future Research

The fact that transients generated at the islanding embed sufficient information to separate from other transient generating events was proved in this thesis. The weaknesses of the proposed islanding detection method were also identified. The classifier needed to

be re-trained when additional generators were connected to the system. Also, the decision tree classifier can become complex with the inclusion of a large set of different transient patterns, and the importance of input features could depend on the system it is applied to. Although, retraining the classifier is a task of running simulations, and reprogramming a microcontroller in the implementation, a possible generalized algorithm would be preferred. It was noticed that the patterns of some features such as level 3 and 4 DWT coefficients were not affected much by the number of generators. Further research in this area could lead to a more generalized islanding detection algorithm based on transient signals.

Thesis outcome was entirely based on the simulation studies. Islanding detection algorithm can be implemented in hardware, and tested using real time simulations to further verify the practicality. Some research in this area was already done [106], but with slight modification to the proposed method. Applying and testing these essential findings on a real microgrid test system is a necessary step towards the practical application.

The developed microgrid test system can be further enhanced by designing improved control for VSC, for example to deal with unbalanced voltages. It would reduce the harmonic level in the system, and voltage unbalance. Furthermore, an energy storage system and a doubly-fed induction generator can be added to the microgrid model to cover wider range of DERs.

Appendix A

(i) Network parameters of three-phase sections of the microgrid test system[39]

node from	node to	R_{ph} [Ω/km]	X_{ph} [Ω/km]	B_{ph} [1/μΩ·km]	R_0 [Ω/km]	X_0 [Ω/km]	B_0 [1/μΩ·km]	l [km]	installation
1	2	0.173	0.4317	3.8305	0.3506	1.7987	0.0025	1.200	overhead
2	3	0.173	0.4317	3.8305	0.3506	1.7987	0.0025	1.000	overhead
3	4	0.173	0.4317	3.8305	0.3506	1.7987	0.0025	0.610	overhead
4	5	0.173	0.4317	3.8305	0.3506	1.7987	0.0025	0.560	overhead
5	6	0.173	0.4317	3.8305	0.3506	1.7987	0.0025	1.540	overhead
6	7	0.173	0.4317	3.8305	0.3506	1.7987	0.0025	0.240	overhead
7	8	0.173	0.4317	3.8305	0.3506	1.7987	0.0025	1.670	overhead
8	9	0.173	0.4317	3.8305	0.3506	1.7987	0.0025	0.320	overhead
9	10	0.173	0.4317	3.8305	0.3506	1.7987	0.0025	0.770	overhead
10	11	0.173	0.4317	3.8305	0.3506	1.7987	0.0025	0.330	overhead
11	4	0.173	0.4317	3.8305	0.3506	1.7987	0.0025	0.490	overhead
3	8	0.173	0.4317	3.8305	0.3506	1.7987	0.0025	1.300	overhead

(ii) Tower geometry and conductor mechanical specifications [39]

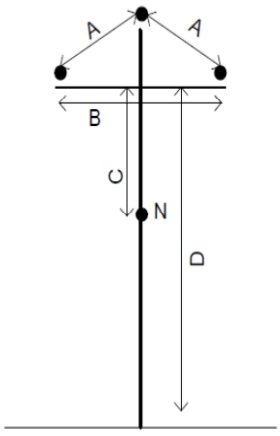

Tower Parameter			
A	*B*	*C*	*D*
1.64 m	3.05 m	2.13 m	13.7 m

conductor type	size AWG	number of strands	d [mm]	r_a [Ω/m]	*GMR* [cm]
AAC	336.4	19	16.9	0.173	0.658

(iii) PSCAD model of the cogeneration plant with generator and turbine parameters

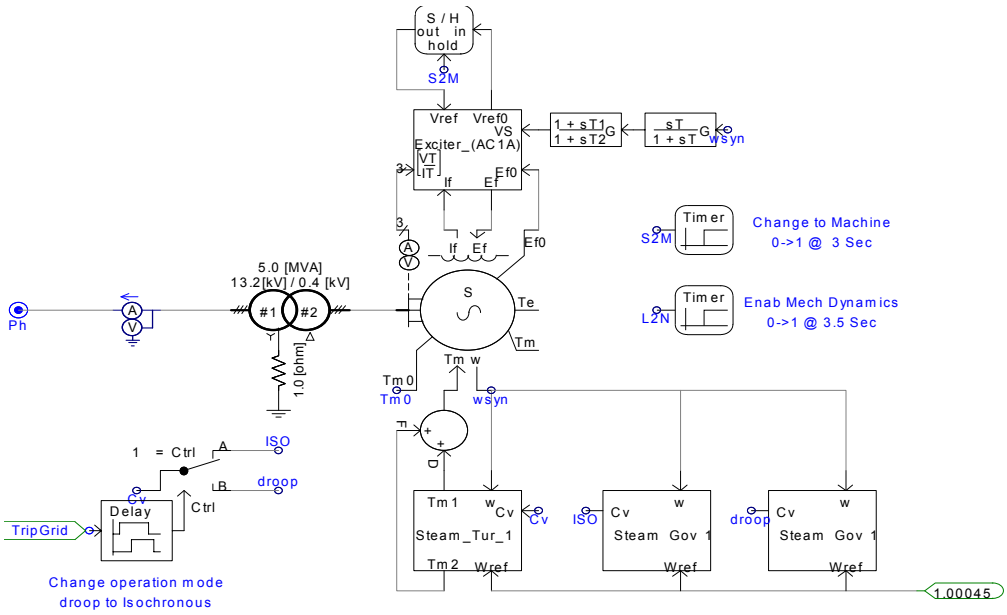

Device	Parameter	Assigned value[55]-[57]
Synchronous Generator (Reference to PSCAD block diagram)	Inertia constant, H	3s
	Armature time const, Ta	0.332s
	Xd, Xd', Xd'', Xq, Xq', Xq''	0.920pu, 0.3pu, 0.22pu, 0.51pu, 0.228pu, 0.29pu
	Tdo', Tdo'', Tdo', Tdo''	5.2s, 0.029s, 0.89s, 0.034s
Steam Turbine (Single reheat cross-compound turbine; Refer-ence to PSCAD block diagram)	High Pressure Turbine K1, K3, K5, K7	0.2pu, 0pu, 0.3pu, 0pu
	Low Pressure Turbine K2, K4, K6, K8	0pu, 0.2pu, 0pu, 0.3pu
	Steam chest time constant, T4	0.1s
	Re-heater time constant, T5	5.0s
	Cross-over time constant, T6	0.5s
	Cross-over time constant, T7	0.5s

(iv) Block diagram of AC1A exciter with the PSS [55]

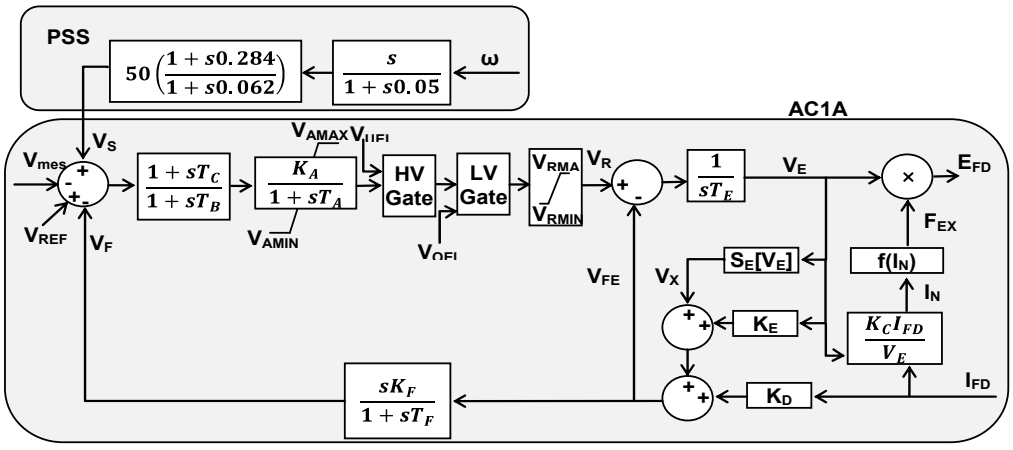

(v) Some of the main parameters of the AC1A exciter [55]

Parameter	**Assigned value**
Regulator gain, K_A; time constant, T_A	400pu; 0.02s
Regulator limits: V_{AMAX}, V_{AMIN}, V_{RMAX}, V_{RMIN}	5pu, -5pu, 7.3pu, -6.6pu
Exciter constant, K_E; time constant, T_E	1pu; 0.8s
Rate feed-back Gain, K_F; time constant, T_F	0.03pu; 1s
Demagnetizing factor, K_D	0.38pu
Field circuit commutating reactance, K_C	0.2pu

(vi) Block diagram of an electro-hydraulic controlled governor [55]

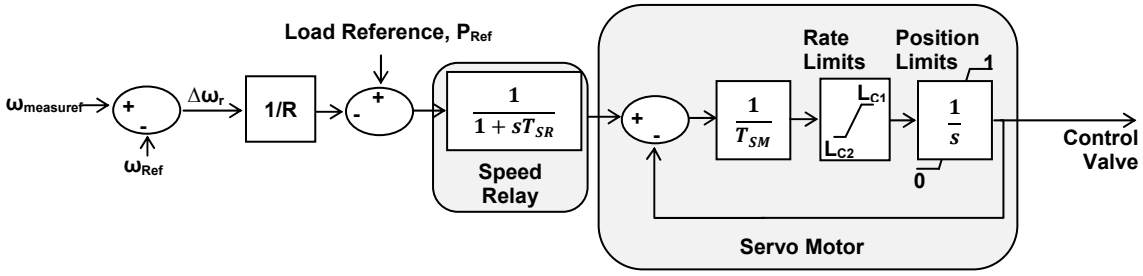

(vii) Steam turbine governor parameters in grid connected and islanded mode [55]

Parameter	Grid connected operation (Droop)	Islanded Operation (Isochronous)
Droop, R	0.05pu	0.003pu
Speed relay time const., T_{SM}	0.1s	0.1s
Opening Rate; L_{C1}, L_{C2}	1, -3	1, -3
Servo Position; P_max, P_min	1, 0	1, 0

(viii) PSCAD model of the wind farm

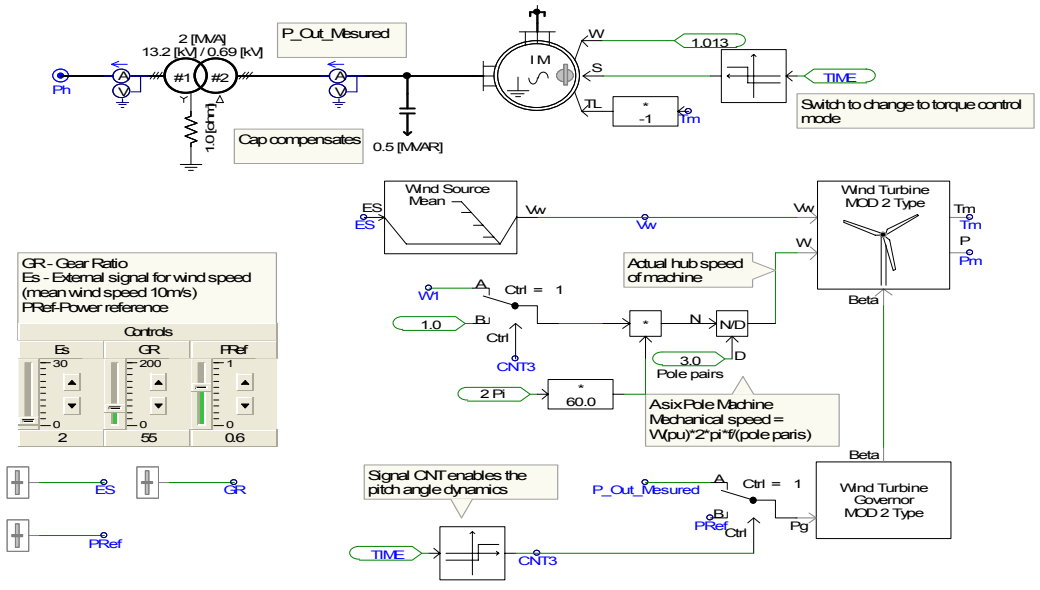

(ix) Block diagram of the wind turbine governor in pitch control [58]

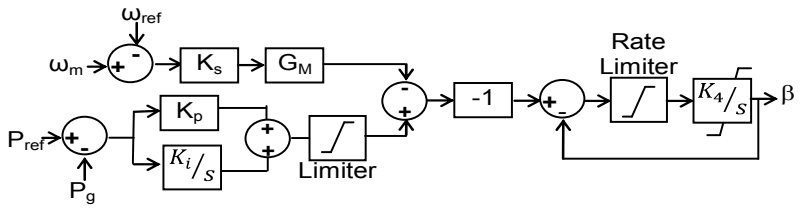

Parameter	Value
Proportional gain, K_p	5 deg/pu
Integral gain, K_i	2 deg/pu
Integrator limits (lower, upper)	-100, 100
Blade actuator integral gain, K_4	0.1 s
Pitch angle limits (lower, upper)	0, 55 deg
Speed damping gain, K_s	0.05 deg/pu
Gain multiplier, G_M	30 deg/pu

(x) PSCAD model of the VSC based dc source

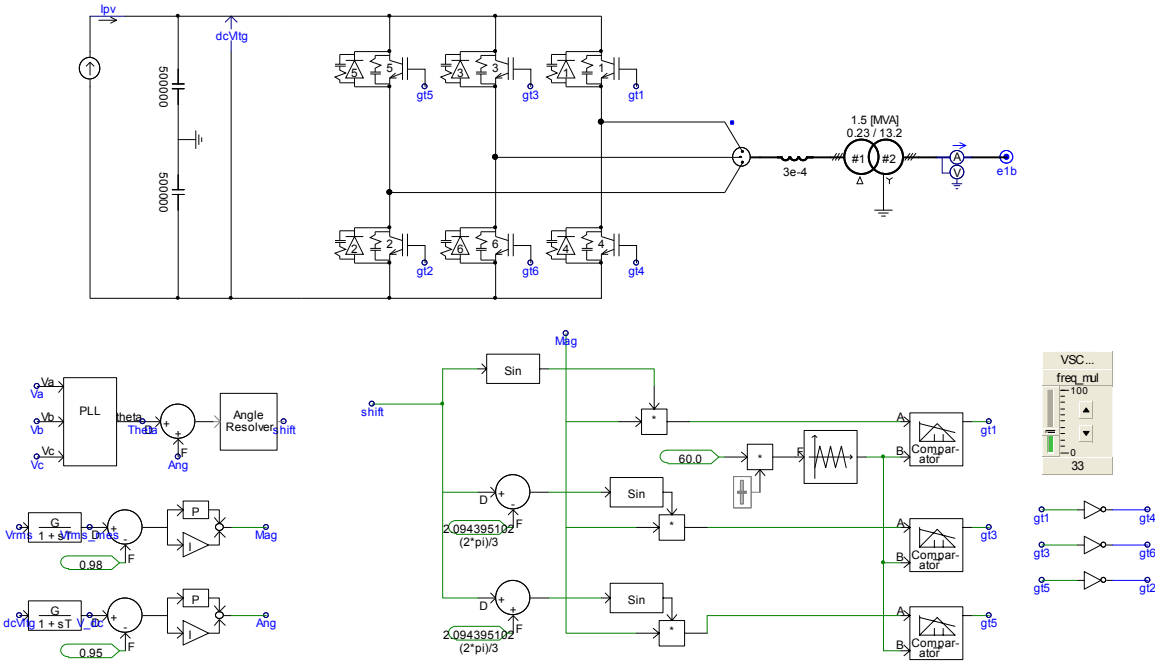

Appendix B

(i) Theory on Training a Dicision Tree

The steps involved in training a Decision Tree using the CART algorithm are presented in the following sections.

a. Finding the best split of each predictor:

In the CART algorithm, each split depends on the value of only one predictor variable (input feature). It carries out a brute force search through all possible splits to find the particular split. Let,

Y_j = class, where $j = 1, 2, ...J$

X_k = predictor variable, where $k = 1, 2, ...P$

$X_k = [D^k_1, ... D^k_m ..., D^k_M]^T$, where $D^k_m = m^{th}$ *value of* k^{th} *variable*

$L = [X_1; ..., X_k; ...; X_P; Y_j]$, where L = learning data set

- ***The tree building starts at the "Root" with the variable X1:***

If the predictor variable X_1 is an ordinal variable with "M" different values (D_m), there are M-1 different splits on X_1. The splits are found by sorting the values (D_m) from the smallest to the largest. For the purpose of illustration, let's take an example case corresponding to Fig. 6-2. The learning dataset, $L = [X_1; X_2; X_3; Y_j]$, where j=1, 2 is given in

Table B-1. The size of the dataset is 10. Table B-1 also shows the sample dataset when sorted by predictor X_1.

Table B-1 Example dataset to explain the selection of split points

	X_1	X_2	X_3	Y_i			X_1	X_2	X_3	Y_i
D_1	2.1	22	200	Y1		D_1	2.1	22	200	Y1
D_2	8.5	83	890	Y2		D_4	3.5	30	310	Y2
D_3	7.9	50	720	Y1		D_7	5.5	70	900	Y1
D_4	3.5	30	310	Y2	Sorted by X_1	D_8	7.8	60	680	Y2
D_5	8	80	800	Y2		D_3	7.9	50	720	Y1
D_6	8.5	85	850	Y1	$\longrightarrow$	D_{10}	7.9	78	700	Y1
D_7	5.5	70	900	Y1		D_5	8	80	800	Y2
D_8	7.8	60	680	Y2		D_9	8.2	81	750	Y2
D_9	8.2	81	750	Y2		D_2	8.5	83	890	Y2
D_{10}	7.9	78	700	Y1		D_6	8.5	85	850	Y1

$(X_1 \leq 2.1), (X_1 \leq 3.5), \ldots, (X_1 \leq 8.2)$ are possible *"split points"* of X_1. At each possible "*split point*" of the variable, the sample is split into two child nodes. Cases with a "yes" response to the question posed are sent to the left node and those with "no" responses are sent to the right node.

- ***Application of the splitting rule:***

There are different splitting rules: "Gini rule", "Twoing rule", "Ordered rule"...etc. Gini rule works well for noisy data and it is used in this study to find the best split [81]. The basic idea behind Gini rule is to search the learning dataset for the largest class and to isolate it from the rest of the data. The mathematical representation is as following: Let,

t = node number

$p(Y_j \mid t)$ = class probability distribution of the dependent variable at node t

$i(t)$ = impurity measure at node t

s = a particular split

p_L = the proportion of cases at node t that go into the left child node, t_L

p_R = the proportion of cases at node t that go into the right child node, t_R

$i(t_L)$ = impurity of the left child node

$i(t_R)$ = impurity of the right child node

$\Delta i(s,t)$ = goodness of split s at node t

For a particular split s at node t, the Gini impurity measure $i(t)$ is defined as:

$$i(t) = 1 - \sum_{1}^{J} p^2(Y_j \mid t) \tag{B1}$$

If priors are proportional to data, then, these probabilities are the observed relative frequencies of each class Y_j at the node t. Therefore,

$$p(Y_1 \mid t) + p(Y_2 \mid t) + \ldots + p(Y_J \mid t) = 1 \tag{B2}$$

Once the impurity measure is calculated, then the goodness of split s, $\Delta i(s, t)$ is calculated.

$$\Delta i(s, t) = i(t) - p_L\,[i(t_L)] - p_R\,[i(t_R)] \tag{B3}$$

The best split point is the one that maximize the $\Delta i(s,t)$ when the node is split according to it.

As an example, the $\Delta i(s,t)$ calculation for split point, $s: X_1 \leq 7.9$, at the Root node is presented in Fig. B-1, and $\Delta i(s,t)$ of all possible split points of X_1 is given in Table B-2. From the table, $s: X_1 \leq 7.9$ has the largest $\Delta i(s,t)$ and thus, the *best split* of X_1.

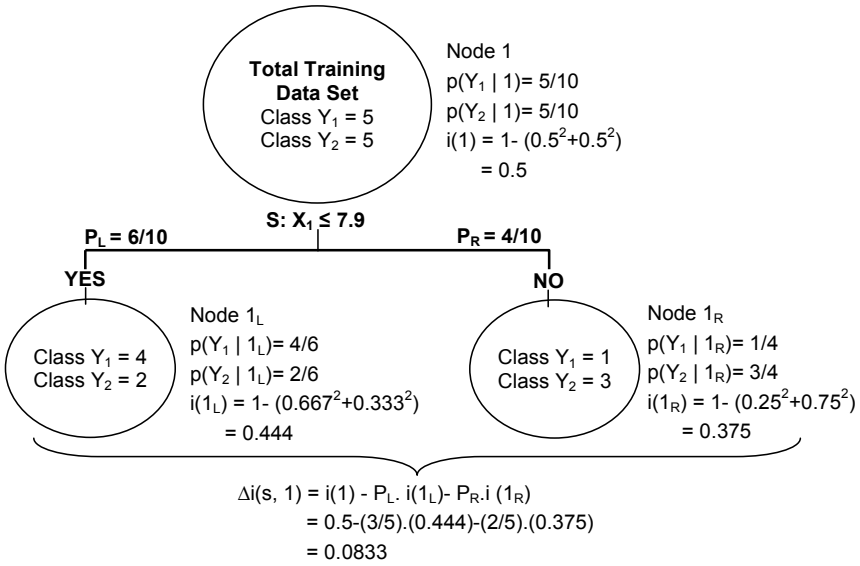

Fig. B-1. Example on *goodness of split* calculation.

Table B-2 *Goodness of split* values at each possible split of X_1

X_1	≤ 2.1	≤ 3.5	≤ 5.5	≤ 7.8	≤ 7.9	≤ 8.0	≤ 8.2
$\Delta i(s, 1)$	0.056	0	0.0238	0.02	0.0833	0.0238	0.025

b. Find the best split of the node:

To find the best split of the node, the above two steps are repeated for each of the remaining variables at the *Root*, and the best splits on each variable is ranked according to the $\Delta i(s,t)$. The algorithm then selects the variable and its split point that minimized the impurity of the *Root*.

As an illustration, Table B-3 presents the best splits of each predictor with their $\Delta i(s,t)$ values. It shows that it is possible to select either s:$X_1 \leq 7.9$ or s:$X_2 \leq 78$ as the best split of the *Root*. If s:$X_1 \leq 7.9$ is selected, s:$X_2 \leq 78$ would be a *surrogate splitter* (a splitting rule that closely mimic the primary split).

Table B-3 The maximum *goodness of split* values of each predictor, X_k

s	$X_1 \leq 7.9$	$X_2 \leq 78$	$X_3 \leq 200$
Δi(s, 1)	0.0833	0.0833	0.0556

c. Class assignment:

There are two rules for assigning classes to nodes:

1. Assign terminal node *t* to a class for which $p(Y_j|t)$ is the highest. The rule assumes equal misclassification costs for each class (refer to Fig. 6-3).
2. *Assign terminal node t to a class for which the expected misclassification cost is at a* minimum. The application of this rule takes into account the severity of the costs of misclassifying cases or observations in a certain class, and incorporates cost variability into a Gini splitting rule, which needs to be modified accordingly.

CART algorithm does not use a stopping rule. It continues growing the classification tree repeatedly applying the above three steps at each child node until further splitting is impossible. When the maximal tree is found CART examines smaller trees by pruning away the possible branches. The best tree is determined by testing for error rates or costs [81]-[82].

Appendix C

(i) Hypothesis testing on classification accuracy [101]

	Testing both DG1 and DG2	
	Total Cases	Correctly Classified Cases
Non-islanding	120	119 (99.16%)
Islanding	138	138 (100%)
Total	258	257 (99.61%)

In considering the total testing data set, having independent trials, which results in only two possible outcomes as "correctly classified" and "misclassified" with constant probability of a success on each trial (p), this experiment can be considered as binomial. Using normal approximation to the binomial, following hypothesis was tested with the parameter of interest being the fraction of misclassification, p.

Null Hypothesis, H_0: $p = 0.02$

H_1: $p < 0.02$

To test the hypothesis with 95% confidence level, define $\alpha = 0.05$.

The test statistic is defined as following in [101].

"Let x be the number of observations in a random sample of size, n that belongs to the class associated with p. Then if the null Hypothesis, H_0: $p = p_0$ is true, we have

x~N(np_0,np_0(1-p)), approximately. To test H_0: $p = p_0$, calculate the test statistic given in (C-1):

$$z_0 = \frac{x - np_0}{\sqrt{np_0(1-p_0)}} \qquad \text{(C-1)}$$

and reject H_0: $p = p_0$, if $z_0 > z_\alpha$ or $z_0 < -z_\alpha$"

Therefore having $x = 1$, $n = 258$, and $p_0 = 0.02$, the test static from (C-1) is:

$$z_0 = \frac{1 - 258 \times 0.02}{\sqrt{258 \times 0.02 \times 0.98}} = -1.85$$

Conclusions: Since ($z_0 = -1.85$) < ($-z_{0.05} = -1.645$), H_0 is rejected and the fraction of mis-classification can concluded to be less than 0.02. Thus, it is proved with 95% confidence that the proposed method has overall classification accuracy greater than 98%.

Bibliography

[1] R.S. Kirby, S. Withington, A.B. Darling and F.G. Kilgour, "Engineering in History," New York: McGraw-Hill Book Company, 1956.

[2] N. Jenkins, R. Allan, P. Crossley, D. Kirschen and G. Strbac, "Embedded generation", UK: IEE, 2000.

[3] G. Pepermansa, J. Driesenb, D. Haeseldonckxc, R. Belmansc, W. D'haeseleer. Distributed generation: definitions, benefits and issues. *Energy Policy* 2005; 33(18): 787-798.

[4] H. B. Püttgen, P. R. Macgregor and F. C. Lambert. "Distributed generation: semantic hype or the dawn of a new era?", *IEEE power & energy magazine*, pp. 22-29, January/February 2003.

[5] A. M. Borbely and J. F. Kreider, "Distributed generation-the power paRigm for the new millennium", Florida: CRC Press LLC, 2001.

[6] G. Hodgkinson. "System implications of embedded generation and its protection and control-PES perspective", IEE Colloquium on System Implications of Embedded Generation & its Protection & Control (Digest No.1998/277), 1998.

[7] T. Y. Ismall, "The implications of embedded generation on the NGC transmission system", IEE Colloquium on System Implications of Embedded Generation & its Protection & Control, (Digest No.1998/277), 1998.

[8] G. Carpinelli, G. Celli, F. Pilo and A. Russo, "Distributed generation siting and sizing under uncertainty", in *Power Tech Proc., 2001 IEEE Porto*, vol. 4, pp. 7.

[9] M. E. H. Golshan and S. A. Arefifar, "Distributed generation, reactive sources & network-configuration planning for power & energy-loss reduction", in *Generation,Transmission & Distribution IEE Proc*. March 2006, vol. 153(2), pp. 127-136.

[10] *Interconnecting Distributed Resources with Electric Power Systems*, IEEE Standard 1547-2003, 2003.

[11] W. Freitas, W. Xu, C.M. Affonso and Z. Haung, "Comparative analysis between ROCOF and vector surge relays for distributed generation applications," *IEEE Transactions on Power Delivery*, vol. 20(2), pp. 1315–1324, April 2005.

[12] R. A. Walling and N. W. Miller, "Distributed generation islanding–implications on power system dynamic performance", in *Power Eng. Society Summer Meeting, 2002 IEEE*, vol. 1, pp. 92-96.

[13] P. Mahat, Z. Chen and B. Bak-Jensen, "Review of islanding detection methods for distributed generation," in *Third Int. Conference on Electric Utility Deregulation and Restructuring and Power Technologies, DRPT 2008*, pp. 2743-2748.

[14] W. Xu, K. Mauch, and S. Martel, "An assessment of DG islanding detection methods and issues for Canada," CANMET Energy Technology Centre – Varennes, Natural Resources Ca, ", Rep. CETC-Varennes 2004-074 (TR), July 2004.

[15] W. Freitas, Z. Huang, and W. Xu, "A practical method for assessing the effectiveness of vector surge relays for distributed generation applications," *IEEE Transactions on Power Delivery*, vol. 20(1), pp. 57-63, January 2005.

[16] J. E. Kim, J. S. Hwang. "Islanding detection method of distributed generation units connected to power distribution system," in *Proc. PowerCon 2000*, Perth, WA, vol. 2, pp. 643-647.

[17] T. Funabashi, K. Koyanagi, and R. Yokoyama, "A review of islanding detection methods for distributed resources," in *Power Tech Conference Proc., 2003 IEEE Bologna*, vol. 2, pp. 6-11.

[18] M. A. Redfern, O. Usta and G. Fielding, "Protection against loss of utility grid supply for a dispersed storage and generation unit," *IEEE Transactions on Power Delivery*, vol. 8(3), pp. 948-954, July 1993.

[19] P. O'Kane and B. Fox, "Loss of mains detection for embedded generation by system impedance monitoring," in *6th International Conference on Developments in Power Systems Protection, IEE 1997*, pp. 95-98.

[20] M. E. Ropp, M. Begovic and A. Rohatgi, "Analysis and performance assessment of the active frequency drift method of islanding prevention," *IEEE Transactions on Energy Conversion*, vol. 14(3), pp. 810–816, September 1999.

[21] Guo-Kiang Hung, Chih-Chang Chang, and Chern-Lin Chen, "Automatic phase-shift method for islanding detection of grid-connected photovoltaic inverters," *IEEE Transactions on Energy Conversion*, vol. 18(1), pp: 169-173, March 2003.

[22] A. Etxegarai, P. Eguía and I. Zamora, "Analysis of remote islanding detection methods for distributed resources," *International Conference on Renewable Energies and Power Quality, ICREPQ'11,* April 2011, pp. 1-6.

[23] Yung-Hsiang Liy, Tain-Syh Luor, Shyh-Jier Huang and Jeu-Min Lin, "Method and system for detecting stand-alone operation of a distributed generating system," US Patent 7342758, March 2008.

[24] Cheng-Tao Hsieh, Jeu-Min Lin and Shyh-Jier Huang, "Enhancement of islanding-detection of distributed generation systems via wavelet transform-based approaches," *International Journal of Electrical Power & Energy Systems*, vol. 30(10), pp. 575-580, December 2008.

[25] A. Pigazo, V. M. Moreno, M. Liserre and A. Dell'Aquila, "Wavelet-based islanding detection algorithm for single-phase PV distributed generation systems," in *IEEE International Symposium on Industrial Electronics (ISIE2007)*, Vigo, Spain, pp. 2409-2413.

[26] K. El-Arroudi, G. Joós, I. Kamwa and D.T. McGillis, "Intelligent-based approach to islanding detection in distributed generation," *IEEE Transactions on Power Delivery*, vol.22, pp. 828-835, April 2007.

[27] S. K. Salman and D. J. King, "Comparison Between The Performance of Ann-Based Loss of Mains Relays Using Multi-Layer and Non-Layered Perceptron Approaches," *International Journal of Innovations in Energy Systems and Power*, Vol. 1, No. 1, pp: 24-28, November 2006.

[28] S. Chowdhury, S.P. Chowdhury, P. Crossley. Microgrids and active distribution networks, IET Renewable Energy Series 6, IET, London, 2009.

[29] H. Zareipour, K. Bhattacharya, C.A. Canizares. Distributed generation: current status and challenges. In:*Proc. of 36th Ann. North American Power Symposium*; 2004.

[30] G. Venkataramanan, C. Marnay. A large role for microgrids: are microgrids a viable paradigm for electricity supply expansion?. *IEEE Power Energy Magazine* 2008; May/June: 78-82.

[31] R. Lasseter, A. Akhil, C. Marnay, J. Stephens, J. Dagle, R. Guttromson, A. S. Meliopoulous, R. Yinger, J. Eto. The CERTS microgrid concept, White paper on Integration of Distributed Energy Resources. CERTS, Ca, Consultant Report no. P500-03-089F, October 2003.

[32] N.W.A. Lidula and A.D. Rajapakse, "Microgrids research: A review of experimental microgrids and test systems," *Renewable and Sustainable Energy Reviews Journal*, vol. 15, pp. 186–202, 2011.

[33] *Guide for Design, Operation, and Integration of Distributed Resource Island Systems with Electric Power Systems,* IEEE standard 1547.4-2011.

[34] B. Kroposki, C. Pink, J. Lynch, V. John, S.M. Daniel, E. Benedict and I. Vihinen, "Development of a high-speed static switch for distributed energy and microgrid applications," *Power Conversion Conference- Nagoya, PCC '07, 2007*, pp: 1418 – 1423.

[35] R.H. Lasseter and P. Piagi, "Control and Design of Microgrid Components," Final Project report: PSERC Publication 06-03, January 2006. Available at http://www.pserc.org/cgi-pserc/getbig/publication/reports/2006report/lasseter_microgridcontrol_final_project_report.pdf

[36] Davood Yazdani, Alireza Bakhshai, Geza Joos, and M. Mojiri, "A nonlinear adaptive synchronization technique for grid-connected distributed energy sources," *IEEE Transactions On Power Electronics*, vol. 23, No. 4, pp. 2181-2186, 2008.

[37] R. Majumder, A. Ghosh, G. Ledwich, and F. Zare, "Power management and power flow control with back-to-back converters in a utility connected microgrid," *IEEE Transactions on Power Systems*, vol. 25, no. 2, pp.821-834, 2010.

[38] H. Laaksonen, and K. Kauhaniemi, "Synchronized re-connection of island operated a LV microgrid back to utility grid," in *Innovative Smart Grid Technologies Conference Europe (ISGT Europe), 2010 IEEE PES*, 2010, pp-1-8.

[39] CIGRE C6.04.02 Task Force, Benchmark Modeling and Simulation for Analysis, Design, and Validation of Distributed Energy Systems, September 2006.

[40] ABB, "Synchrocheck relay," product guide SPAU 140 C, 1MRS750421-MBG, Version: C/25.04.2006, 2006. Available at: http://www05.abb.com/global/scot/scot229.nsf/veritydisplay/8bbf5b573eb0ae36c1257176002994de/$file/spau140c_tob_750421enc.pdf

[41] A. Doukas. Distributed generation in Canada - maximizing the benefits of renewable resource; Promoting a Transition to Renewable Energy. Canadian Renewable Energy Alliance. August 2006.

[42] T. Sels, C.Dragu, T. Van Craenenbroeck, R. Belmans. Electrical energy storage systems: existing systems versus newest systems–an overview. *In Power generation and sustainable development International conference; 2001*. pp. 215-220.

[43] E. A. Technology. Review of electrical energy storage technologies and systems and of their potential for the UK. DTI 2004. URN 04/1876.

[44] B. Kroposki, R.Lasseter, T. Ise, S. Morozumi, S. Papatlianassiou N. Hatziargyriou. "A look at microgrid technologies and testing projects from around the world, Making microgrids work". *IEEE Power Energy Magazine 2008*; May/June: 40-53.

[45] F. Katiraei, R. Iravani, N. Hatziargyriou, "A. Dimeas. Microgrids management: controls and operation aspects of microgrids". *IEEE Power Energy Magazine 2008*; May/June: 54-65.

[46] DTI. Micro-generation strategy and low carbon buildings programme–consultation. Available on 23 June 2005. http://www.dti.gov.uk/files/file13989.pdf

[47] J. Driesen, F. Katiraei. "Design for distributed energy resources". *IEEE Power Energy Magazine 2008*; May/June: 30-40.

[48] R.H. Lasseter, P. Piagi. Control and design of microgrid components. Final Project report: PSERC Publication 06-03. Available online on January 2006. http://www.pserc.org/cgi-pserc/getbig/publicatio/reports/ 2006report/lasseter_microgridcontrol_final_project_report.pdf

[49] C.K. Sao and P.W. Lehn, "Control and Power Management of converter fed microgrids," *IEEE Trans. on Power Sys*, Vol.23, No.3, pp:1088-1098, Aug. 2008.

[50] C.F. Ten and P.A. Crossley, "Control of multiple distributed generators for intentional islanding," *SmartGrids for Distribution, 2008, IET-CIRED*, pp:1-4.

[51] H.H. Zeineldin, E.F. El-Saadany and M.M.A. Salama, "Distributed generation micro-grid operation: control and protection," *Advanced Metering, Protection, Control, Communication, and Distributed Resources, 2006, PS apos*; *06*, pp:105 – 111.

[52] T. Tanabe et al, "An active network control method using distributed energy resources in microgrids," *13th Power Electronics and Motion Control Conference, EPE-PEMC 2008*, pp: 2478 – 2480.

[53] A.L. Dimeasand and N.D. Hatziargyriou, "Operation of a multiagent system for microgrid control," *IEEE Transactions on Power Systems*, vol. 20, No. 3, pp: 1447-1455, August 2005.

[54] Z. Jiang and R.A. Dougal, "Hierarchical microgrid parigm for integration of distributed energy resources," *Power and Energy Society General Meeting - Conversion and Delivery of Electrical Energy in the 21st Century, 2008 IEEE*, pp: 1-8.

[55] A.M. Gole (Principal Editor), J. Martinez Velasco and A.J.F. Keri, "Modelling and Analysis of System Transients Using Digital Programs", IEEE Special Publication, IEEE Catalog No. 99TP 133-0, Piscataway, N.J., January 1999.

[56] P. Kundur, "Power sys. stability and control," USA: McGraw-Hill, 1994.

[57] Powerforce APP Ltd. Technical, standards and control issues of embedded generation. DTI Pub. URN 00/1449.

[58] *PSCAD online help system*, Manitoba HVDC Research Center Inc., MB, Canada, 2003-2006.

[59] P.M. Anderson, A. Bose, "Stability simulation of wind turbine systems," *Transactions on Power Apparatus and Systems*. vol. PAS 102 (12), pp. 3791-3795, December 1983.

[60] J. Arrillaga, Y.H. Liu and N.R. Watson, "Flexible power transmission, the HVDC options," UK: John Wiley & Sons Ltd, 2007.

[61] Y. Suh, V. Tijeras, and T. A. Lipo, "A nonlinear control of the instantaneous power in dq synchronous frame for PWM AC/DC converter under generalized unbalanced operating conditions," *37th IAS Annual Meeting. Conference Record of the Industry Applications Conference*, 2002, vol.2, pp. 1189- 1196.

[62] A. M. Gole, S. Filizadeh, R. W. Menzies and P. L. Wilson, "Optimization-enabled electromagnetic transient simulation," *IEEE Trans. Power Delivery*, vol. 20, pp. 512-518, Jan. 2005.

[63] GE Power Management, "Load shedding, load restoration and generator protection using solid-state and electromechanical under frequency relays," Ontario, Canada, Rep. GET-6449.

[64] A. A. M. Zin, H. M. Hafcz and W. K. Wong, "Static and dynamic under-frequency load shedding: a comparison," in Proc. *International Conference on Power System Technology - POWERCON 2004*, Singapore, 2004, Vol. 1, pp. 941-945.

[65] Transend Networks Pty Ltd, "Frequency Standard Development," Final Report to Alinta Power, TrimD07/:66728, December 2007 [online]. Available at: http://www.aemc.gov.au/Media/docs/Alinta%20Submission%20-%20revised%2021%20May%202008-d0ad3b48-a016-470c-aa9d-cb4e90206c55-0.pdf.

[66] B. Delfino, S. Massucco, A. Morini, P. Scalera, and F. Silvestro, "Implementation and comparison of different under frequency load-shedding schemes," *Power Engineering Society Summer Meeting, 2001. IEEE*, Vol. 1, pp. 307-312.

[67] *Technical requirements for connecting distributed recourses to the Manitoba Hydro system*, DRG 2003, Revision 2, Manitoba Hydro Electric Board, June 2010.

[68] *Power quality specification for interconnection to Manitoba Hydro's electrical system*, PQS2000, Revision 2, Manitoba Hydro Electric Board, April 2011.

[69] F. Katiraei, M. R. Iravani, and P. W. Lehn, "Micro-grid autonomous operation during and subsequent to islanding process," *IEEE Transactions on Power Delivery*, vol. 20, No. 1, pp: 248 - 257, January 2005.

[70] Basler Electric International (Original Author: George Rockefeller). (2001 June). Generator Protection Application Guide (Revised) [online]. Available at: http://www.basler.com/downloads/genprot guidC.pdf

[71] Basler Electric, "BE1-81O/U," Instruction manual for digital frequency relay, Publication: 9137300990. Available at: https://www.eiseverywhere.com/file_uploads/b9944a1d22cd6a824e2c0d62f10b5a1e_6_BE1_81_O_U_9137300990L.pdf

[72] B. Fox, D. Flynn, L. Bryans, N. Jenkins, D. Milborrow, M. O'Malley, R. Watson, O. Anaya-Lara, "Wind power integration connection and system operational aspects," IET Power Energy, Series 50, UK: IET, 2007.

[73] T.H.M. EL-Fouly and C. Abbey, "Commercial relays field tests for passive anti-islanding protection schemes of synchronous generator based DGs," *in CIGRÉ Canada Conference on Power Systems*, Toronto, October 2009, Paper # 164.

[74] Vaasa Electronic Group, "Step by step instruction to activating the synchrocheck function in VAMP relays," application note, AN200/EN004, May 2008. Available at: http://www.vamp.fi/Technical%20papers/Application%20notes/English/AN200.EN004%20Step%20by%20step%20instruction%20to%20activating%20the%20synchrocheck%20function%20in%20the%20VAMP%20relays.pdf

[75] *Network Planning Guideline for MV Shunt Capacitors*, Guideline, Eskom Distribut Tech, revised on June 2010. Available at: http://bits.eskom.co.za/dtechsec/distribu/tech/GUIDE/DGL_34-598.pdf

[76] Specification of FRANKE's MV Capacitor Banks and Capacitors, Franke Gmkp Energy Ltd. Available at: http://www.frankeenergy.com/84.pdf

[77] Synchronism Check Relays, MLJ, Instructions manual, GEK-106213C, GE Power Management. Available at: http://www.gedigitalenergy.com/products/manuals/mlj/mljman-c.pdf

[78] Tzung-Lin Lee; Shang-Hung Hu; Yu-Hung Chan, "Design of D-STATCOM for voltage regulation in microgrids," in *Energy Conversion Congress and Exposition (ECCE), 2010 IEEE*, pp. 3456 – 3463.

[79] P. Bogónez-Franco, J. Balcells, O. Junyent , J. Jordà, "SVC model for voltage Control of a microgrid," in *IEEE International Symposium on Industrial Electronics (ISIE),* 2011, pp. 1645 – 1649.

[80] A. Foss and K. Leppik, "Design and implementation of an anti-islanding protection strategy for distributed generation involving multiple passive protections," *in IEEE conference Electrical Power & Energy Conference (EPEC)*, 2009, pp. 1-4.

[81] Y. Sheng, S. M, Rovnyak, "Decision tree-based methodology for high impedance fault detection," *IEEE Transactions on Power Delivery*, vol. 19(2), pp. 533-536, April 2004.

[82] B. Leo, J. Friedman, R. Olshen and C. Stone, "Classification and regression trees," Pacific Grove: Wadsworth, 1984.

[83] D. Steinberg and P. Colla, "CART: tree-structured non-parametric data analysis," San Diego, CA: Salford Systems, 1995.

[84] L. Bel, D. Allard, J.M. Laurent, R. Cheddadi and A. Bar-Hend, "CART algorithm for spatial data: Application to environmental and ecological data," *Computational Statistics & Data Analysis,* vol. 53(8), pp. 3082-3093, June 2009.

[85] D. F. Specht, "Probabilistic neural networks," *Neural Networks*, vol. 3, pp. 109-118, 1990.

[86] J. Upendar, C. P. Gupta and G. K. Singh, "Discrete wavelet transform and probabilistic neural network based algorithm for classification of fault on transmission systems," in *Annual IEEE India Conference, 2008. INDICON 2008*, pp. 206-211, January 2009.

[87] Goh A.T, "Probabilistic neural network for evaluating seismic liquefaction potential," *Canadian Geotechnical Journal*, Vol. 39, No. 1, pp. 219-232(14), February 2002.

[88] C. W. i Hsu, C. C. Chang, and C.J Lin, "A practical guide to support vector classification," Dept. of Computer Science, National Taiwan University, May 2008. Available: http://www.csie.ntu.edu.tw/~cjlin/papers/guide/guide.pdf

[89] P. Janik and T. Lobos, "Automated classification of power-quality disturbances using SVM and RBF networks," *IEEE Trans. on Power Delivery*, Vol. 21, No. 3, July 2006.

[90] S. Chen, "Feature selection for identification and classification of power quality disturbances," in *Power Engineering Society General Meeting, 2005. IEEE*, vol. 3, pp. 2301 – 2306.

[91] D.C. Robertson, O.I. Camps, J.S. Mayer, and W.B. Gish, "Wavelets and electromagnetic power system transients", *IEEE Transactions on Power Delivery*, vol. 11(2), April 1996.

[92] I. Daubechies, "Ten lectures on wavelets", Philadelphia: SIAM, 1992.

[93] A. Graps, "An introduction to wavelets," *Computing in Science and Engineering*, vol. 2(2), pp. 50-61, June 1995.

[94] C. H. Kim and R. Agganrval, "Wavelet transforms in power systems – Part 1: General introduction to the wavelet transforms," *IEEE Power Engineering Journal*, vol. 14(2), pp. 81-87, April 2000.

[95] H. A. Darwish, M. H. Farouk, Abdel-Maksoud I. Taalab and N. M. Mansour, "Investigation of real–time implementation of DSP-based DWT for power system protection," *Transmission and Distribution Conference and Exhibition, 2005/2006 IEEE PES*, pp. 1258-1263.

[96] N. Perera, "Rapid Isolation of Faults in Power Networks with Distributed Generators," M.Sc. Thesis, The University of Manitoba, Winnipeg, Manitoba, Canada, May 2007.

[97] T. Frederick and N. Erdol, "Arbitrary tilings of phase space," *IEEE International Conference on Acoustics, Speech, and Signal Processing, 1994. ICASSP-94.*, vol. 3, pp. III/25 - III/28.

[98] Olga Veksler, "Pattern Recognition," Lecture Notes, Department of Computer Science, The University of Western Ontario, Winter 2006. Available: http://www.csd.uwo.ca/courses/CS434b/

[99] N. W. A. Lidula, N. Perera and A. D. Rajapakse, "Investigation of a Fast Islanding Detection Methodology Using Transient Signals," in *Power & Energy Society General Meeting, 2009. PES '09. IEEE*, pp. 1-6.

[100] Chih-Chung Chang and Chih-Jen Lin, "LIBSVM - A Library for Support Vector Machines," 2001, Software available at http://www.csie.ntu.edu.tw/~cjlin/libsvm.

[101] D. C. Montgomery, G. C. Runger and N. F. Hubel, "Engineering statistics," USA: John Wiley & Sons Inc., 1998.

[102] U. D. Dwivedi and S. N. Singh, "A wavelet-based de-noising technique for improved monitoring and characterization of power quality disturbances," *Electric Power Components and Systems*, vol. 37(7), pp. 753–769, July 2009.

[103] Hong-Tzer Yang, and Chiung-Chou Liao, "A de-noising scheme for enhancing wavelet-based power quality monitoring system," *IEEE Transactions on Power Delivery*, vol. 16(3), pp. 353-360, July 2001.

[104] I. W. C. Lee, and P. K. Dash, "S-transform-based intelligent system for classification of power quality disturbance signals," *IEEE Transactions on Industrial Electronics*, vol. 50(4), pp. 800-805, August 2003.

[105] C. R. Pinnegar, H. Khosravani and P. Federico, "Time-time distributions for discrete wavelet transforms," in *Operator Theory: Advances and Applications*, vol. 1, Switzerland: Birkh¨auser Verlag Basel, 2009, pp. 269-276.

[106] Jean-Paul Pham, N. Denboer, N. W. A. Lidula, N. Perera, and A. D. Rajapakse, "Hardware implementation of an islanding detection approach based on current and voltage transients," in *IEEE Electrical Power and Energy Conference, IEEE EPEC 2011,* pp.152-157.